Plaster Modelling of Fault Development in Extensional Regimes

Margrethe Sæterdal Bøyum

Thesis for the degree

Master of Science

Department of Earth Science

University of Bergen

June 2015

Abstract

The full complexity of deformation in natural extensional regimes is complicated, as direct observation in nature is limited in regards to outcrops and structural evolution over time. The aim of this thesis is to analyse the growth and evolution of fault systems in rift settings using physical experiments. Seismic imaging is widely used for exploring the subsurface, however its resolution may simplify small-scale deformation. When sub-seismic structures are not accounted for, the limited understanding of the structural complexity of the subsurface can lead to complications during exploration and production of hydrocarbons.

Analogue plaster modelling can provide a valuable insight of both large- and small-scale structures in space and time, as the models show the deformation history from fault initiation to a fully developed extensional basin. Plaster of Paris is well suited for producing and preserving large- and small-scale structures for further analysis. Unilateral extensional experiments show that deformation is dependent on the plaster rheology, basement geometry and extension rate. The models are compared to natural extensional systems.

The large fault planes interact in three dimensions, and the fault growth style is dependent on the primary structures. Fault planes form by cutting through an array of sub-planar first generation faults. Their exact growth pattern may vary between the two profile planes of the same model, and their timing may also be different. The first brittle deformation occurs within 10% extension and a through-cutting fault plane forms within 23% extension, followed by secondary deformation. The largest amount of deformation in found to be in the hanging wall as it rotates and shears internally to generate faults with a variety of dip angles. The deformation zone growth and structural complexity are promoted by a changing footwall fault gradient. One of the reoccurring features is antithetic faulting and the formation of horst and graben structures above a low-angle fault. Relatively ductile sections with a small cumulative number of faults accommodate 70-90% of the total horizontal extension, while for relatively brittle sections the larger faults accommodate 43-63%. This distribution supports that the extension of a seismic section with a large number of sub-seismic faults may be underestimated, due to a wider distribution of displacement.

Keywords: Extension, analogue modelling, plaster, stretching factor, fault plane geometry.

Acknowledgements

I would like to express my appreciation for the opportunity to work with this project and for everyone who has participated. First of all I would like to thank my supervisors Haakon Fossen (UiB, Department of Earth Science), Atle Rotevatn (UiB, Department of Earth Science), Eivind Bastesen (UiB, CIPR), Tore Odinsen (Statoil ASA) and Signe Ottesen (Statoil ASA) for excellent guidance during the laboratory work. I would also like to extend an extra appreciation for the guidance and feedback on the written work provided by Eivind Bastesen and Tore Odinsen. Thank you Statoil and the University of Bergen for funding the project.

I am grateful for everyone who has taken the time during these two years to assist during the experiments and provide guidance. This thesis is a part of a larger research group at the department of Earth Science and I would like to thank my fellow plaster students for a great collaboration: Maria Helena Seim, Marie D. Eri, Christine T. Andersen, Renate E. Tveit and Ingvild Blækkan.

I would like to thank all the student volunteers assisting the experiments and also Hamed Khani for guidance and Jozef Kusior for excellent carpentry.

Finally, I would like to thank Magnus for his patience during these five years of studies and his great support while writing this thesis.

Margrethe Bøyum

CONTENTS

CHAPTER 1 Introduction

1.1 Introduction

This thesis is a part of a master programme within geodynamics and structural geology at the Department of earth science, University of Bergen, and involves analogue experimental studies of extensional deformation in plaster of Paris. The experiments are performed in collaboration with two other sister projects focussing on contraction and strike-slip, respectively. These projects are a part of a renewed activity on analogue plaster experiments and are funded by Statoil and the University of Bergen.

1.2 Aim and motivation

The purpose of analogue modelling is to explore the formation and development of normal faults and concomitant structures. By observing structures in nature, one is limited to the extent of the outcrop available as well as the capacity of applied methods. This usually also means observing the end product of deformation, while the deformation history itself is an interpretation based on the end product, which may involve restoration and balancing (Gibbs, 1983). On the other hand, analogue modelling allows for analysis in four dimensions of structures forming during fault initiation, propagation and interaction in a rift setting. The experimental set-up style provides a view of the surface deformation as well as two vertical profile planes oriented perpendicular to the fault strike trend in the model. Three high-resolution cameras capture the structural evolution and fault interference in the horizontal and two vertical planes during the experiment (for specifications see section 4.1.6), from which the strain-rate, deformation evolution and timing can be estimated.

1.3 The scientific value of plaster modelling

In the petroleum industry, knowledge of the geometry of normal faults and their concomitant structures is important to understand the migration and sealing of fluids in reservoirs (Caine et al., 1996; Childs et al., 1997; Fisher et al., 2001). Many of the petroleum traps on the Norwegian continental shelf are related to extensional structures (Fossen et al., 1998). An important tool used for investigating the subsurface at a large scale is seismic imaging. The

quality and resolution of seismic data largely control how the subsurface is perceived and interpreted. Poor seismic imaging of an area may be a big challenge when making detailed geological models. The resolution of seismic data is dependent on the wavelength of the seismic signal as well as signal noise. The vertical resolution for modern high-quality 3D seismic data sets is 20-30 m. Fault with throw less than 20-30 m are thus difficult to see or not apparent in the resolution of seismic data, and thus called sub-seismic faults (Rotevatn et al., 2011). Small-scale structures may not be visible in seismic imaging as there is no significant disturbance of the layering or offset of the rocks. This may lead to an underestimation of the extent of a fault. Experimental modelling using plaster provides very good seismic analogues as small-scale structures such as lenses and minor faults are generated and preserved in the models (Fossen et al., 1996).

A simplified portrayal of the substrata means that the complexity of extensional deformation is not seen, which can be challenging during exploration and production of hydrocarbons. Plaster experiments can increase the general understanding of the development of rift settings at various scales. The experiments develops from an unstrained to heavily deformed state in a short period of time, and show both large and small-scale structures. The end model can be further studied and preserved as the plaster solidifies shortly after the experiment.

Compared to sand box experiments, the fine-grained plaster of Paris is well suited to produce small-scale structures. A representative grain size of plaster of Paris grain is 10 μm (Lewry et al., 1994) and a typical model length is 30 cm long. Dry quartz sand used widely for experiments have sizes between 190-275 μm (McClay, 1996). If the length of the model were scaled up from 30 cm to 1 km, the grain size of plaster and sand would be 3.3 cm and 63 cm, respectively.

Visualisation of deformation patterns and stepwise figures are also a useful tool for the basic and intuitive understanding of how the crust deforms an audience outside the geological community. The models provide an intuitive visual aid when a geologist is observing structures in nature and tries to visualise the deformation history.

1.4 Main objectives

The aim of this study is to investigate fault formation, fault growth and structural evolution in an extensional setting using analogue plaster modelling. The photographic data collected is of

higher quality and the rate of which the photographs are taken is higher than before for plaster experiments (Odinsen, 1992; Fossen et al., 1996; Gabrielsen et al., 2001; Lindanger et al., 2004). Specifications for the cameras used are provided in section 4.1.6 Data collection. The experimental set-up allows a view of the structural evolution through time in two profile planes perpendicular to strike and of the model surface. The plaster cover allows for large-scale structures to form as well as minor structures and secondary processes associated with master fault planes and their evolution. This thesis provides detailed interpreted sections of structural evolution of the experiments. The collected data can be used to increase the knowledge of general deformation patterns in the crust.

CHAPTER 2 Extensional fault architecture

2.1 Introduction

This chapter provides a short overview of theories behind the growth and architecture of natural faults. Additional terms and processes used for describing the plaster models presented in this thesis are defined in Appendix A: Definitions.

Normal faults form as a result of the extension of the crust. Extension forms either due to gravity or to crustal break-up. When plates are diverging, breaking up and moving away from each other due to plate tectonic forces, the crust is thinned and starts to form normal faulting in a rift zone. In large orogens, extension takes place due to large gravitational forces, and the understanding of the collapse related extensional fault grew in the 1980s. Previously these low-angle faults were interpreted to be contractional faults. Extensional faults are thus considered as an important structure formed post-orogenic due to loss of potential energy stored during mountain build-up. When the compressional forces on the mountain decreases, their weight pushes down on the crust and forces it to move away (Stüwe, 2007). Extensional faults also form near surface associated with larger landslides (Braathen et al., 2004).

Understanding the structural complexity of extensional faults is also valuable when making geological models of the subsurface, as many hydrocarbon plays are found in extensional settings (Ehrlich et al., 2004). This thesis focuses on the structural evolution of an extensional basin (Gibbs, 1984). As seismic image show fault segments with displacement larger than 20-30 m (Rotevatn et al., 2011), the fault tip-lines and the process zones are usually not visible on seismic images as there is no significant disturbance of the layering or offset of the rocks. This may lead to an underestimation of the extent of a fault. Experimental modelling using plaster provides very good seismic analogues as small-scale structures as lenses and minor faults are generated and preserved along with the large scale structures which is rare within experimental modelling (Fossen et al., 1996).

2.2 Fault zone architecture

A fault zone is commonly describes with a fault core surrounded by a damage zone (Fig. 1A and B) (Caine et al., 1996; Braathen et al., 2009). A fault core is where most of the displacement is accumulated and may consist of altered rocks and fault rocks such as gouge, cataclasite and mylonite. The surrounding damage zone may consist of minor faults and fractures as well as veins and folds. A wide damage zone indicates several sequences of faulting and deformation. The properties of the damage zone may accommodate or inhibit migration between the protolith and the fault core. The permeability of a fault zone is controlled by the grain-scale of the fault rocks within the fault core, and the hydraulic properties of fractures in the damage zone (Caine et al., 1996).

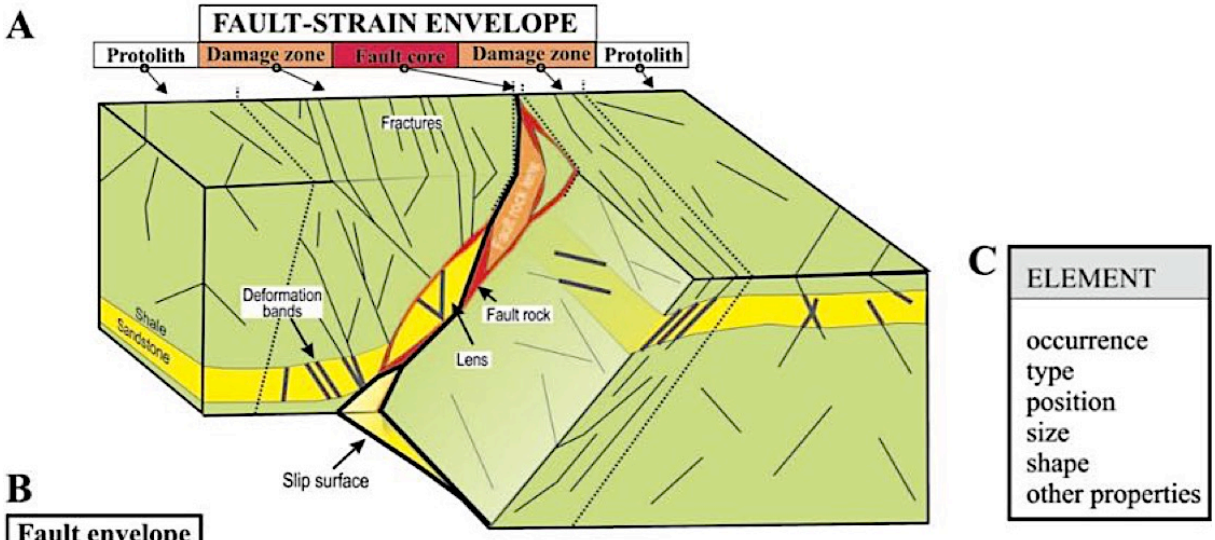

B

Fault envelope

STRAINED ROCK VOLUME	ZONING		APPEARANCE	TYPICAL ORIENTATION
	Fault core	**Damage zone**		
ELEMENTS	deformation band	deformation band	millimeter tabular zone	Riedel sets
	slip surface	slip surface	cohesion-free discontinuity	parallel with fault
	fracture	fracture	cohesion-free discontinuity	Riedel sets
	cleavage	cleavage	disolution and mineral orientation surface	parallel with fault or fold surface
	stylolith	stylolith	disolution surface	parallel with fault or fold surface
	fault-rock layer		deformed host-rock layer along fault	parallel with fault
	shale smear		smeared shale layer along fault	parallel with fault
	sand smear		smeared sand layer along fault	parallel with fault
	mixed unit	mixed unit	layer of mixed sand-shale	parallel with fault
	membrane		layer of fault rock or smear along fault	parallel with fault
	lens	lens	tectonic body of host or fault rock	long axis parallel with fault

C

ELEMENT
occurrence
type
position
size
shape
other properties

Fig. 1: (A) An illustration of common structures found related to extensional faulting. (B) The diagram shows the occurrence of structural elements in the different zones and their characteristics. (C) List of the required elements of fault modelling. Modified from Braathen et al. (2009).

2.3 Fault growth

Consensus is that larger faults form by the linkage of small and isolated faults, which interact to form increasingly complex patterns. If the small faults are in fact isolated and unrelated to the surrounding brittle expressions or if they form as an array of minor faults, which is related mechanically and in space is debated. Walsh et al. (2003) suggests two models of fault growth termed isolated fault model and coherent fault model of which the isolated fault model is widely used. The isolated fault model treats the initial faults as unaffected by the surroundings until a coincidental configuration leads to fault interaction. These fault growth models are often based on two-dimensional studies and modelling and their spatial distribution are inferred in three dimensions (Walsh et al. (2003) and references therein). The coherent fault model expresses that faults form within a kinematically coherent system as a result of the three-dimensional propagation and their spatial distribution.

Fault plane interaction

Larger faults are often formed as smaller faults grow and link together. Fault planes have a relatively wide range of geometries, of which planar, listric and ramp-flat-ramp faults are common, and these geometries are related to the process of fault growth and linkage. There are two main types of fault linkage (Gupta et al., 2000). Soft linkage is the interaction of the stress fields of two fault planes. Soft linkage has a low impact on the fault geometry. It may be difficult to constrain the entire extent to the fault planes where they are not in view and they may physically interact. Fault planes that are physically connected are hard-linked and their interaction changes the fault plane geometry. The damage zone is wider in the areas where fault planes are hard-linked (Ehrlich et al., 2004; Rotevatn et al., 2012).

Formation of extensional duplexes

Irregularities such as fault bends, extensional duplexes (Gibbs, 1983) along a fault trace are formed by several different processes including: tip-line coalescence (Fig. 2A), segment linkage (Fig. 2B), tip-line bifurcation (Fig. 2C) and by asperity bifurcation (Fig. 2D) (Gabrielsen et al., 2001). Irregularities formed during fault evolution are progressively smoothed out due to continuing of displacement causing formation of fault lenses (Gabrielsen et al., 2001) and fault rocks (Childs et al., 2009). Larger irregularities are typically evened out by asperity bifurcation (Fig. 2D), which yields a secondary fault plane enveloping a fault lens. The formation of duplexes is related to multiple phases of asperity bifurcation, segment

splaying (Fig. 2E) or the coalescence of secondary structures to a master fault plane (Fig. 2F). Further displacement leads to internal shear in the horses, separating the horses into smaller units and a complex structure pattern. These processes widen the fault zone.

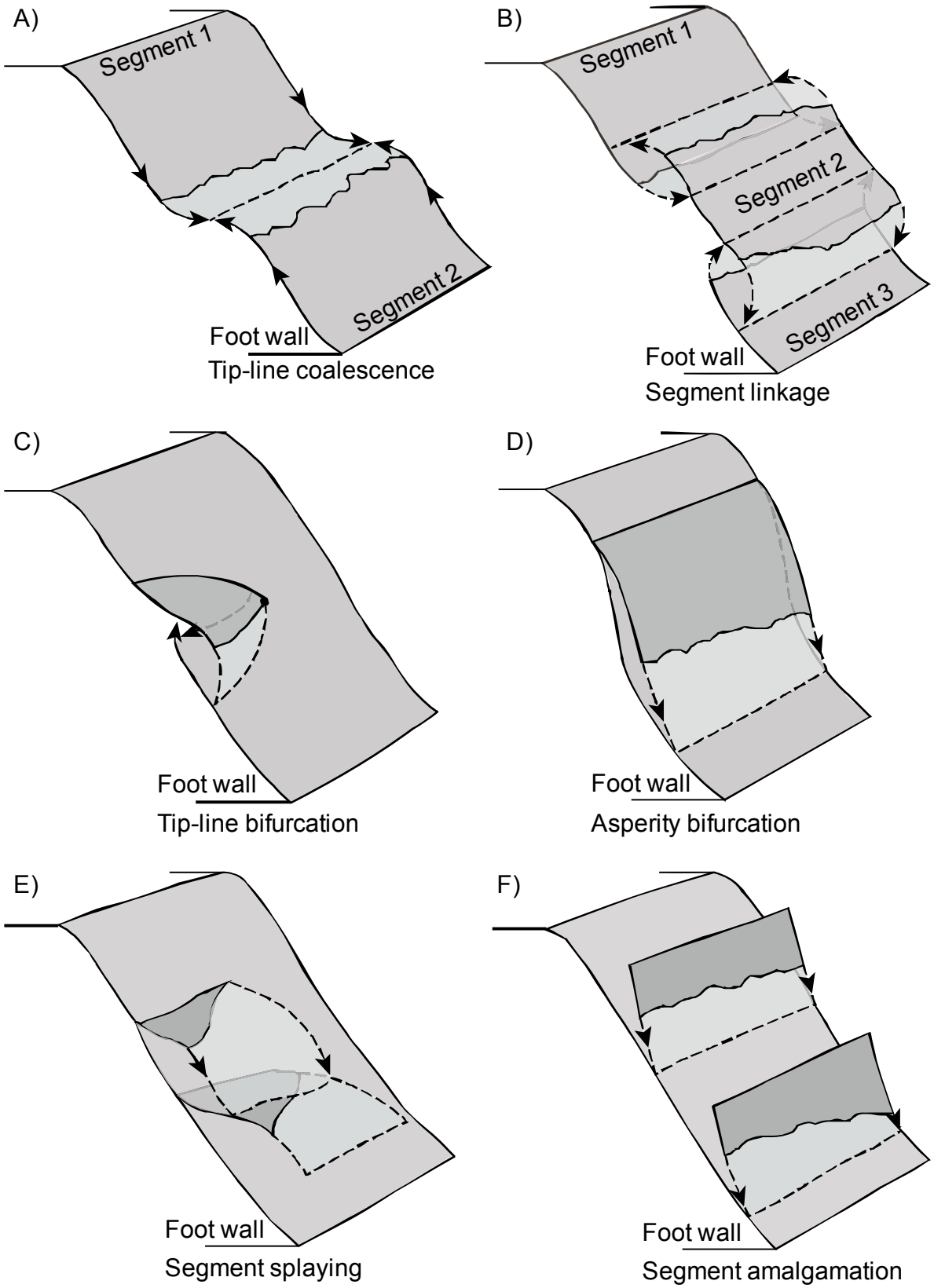

Fig. 2: Figures A-F illustrate primary and secondary processes to form extensional duplexes, (A) Tip-line coalescence, (B) Segment linkage, (C) Tip-line bifurcation, (D) Asperity bifurcation, (E) Segment splaying, (F) Segment amalgamation. See text above for description and Appendix A: Definitions for further reference. Modified from (Gabrielsen et al., 2001).

Structures found in extensional basins

Gibbs (1984) described the structural evolution found within high extensional basin margins and discusses their similarities to structures found in the contractional regime. Low-angle faults, ramp-flat-ramp faults and planar faults are common fault geometries interpreted in seismic sections. Complex strain-patterns in the hanging wall induce secondary structures such as folding and syn- and antithetic faulting. Single riders or an array of riders in a listric fan may form as the hanging wall moves down a ramp-flat-ramp fault to the shallower portion. An extensional duplex zone of extensional horses may form by changing trajectories of the footwall fault.

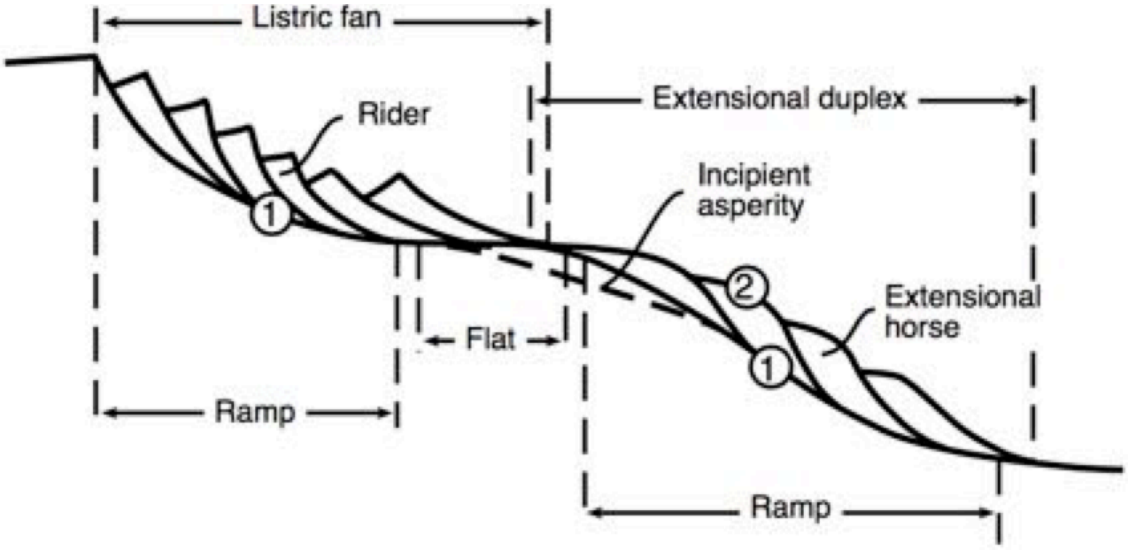

Fig. 3: Illustration of a ramp-flat-ramp fault with secondary structures. The collective term of a fan of riders is a listric fan, and an array of extensional horses is an extensional duplex. The numbers indicate a floor fault (1) and a roof fault (2). The figure is modified from Gabrielsen et al. (2001), and is based on Gibbs (1984) and Childs et al. (1997).

Fault scaling relations

The scaling relationships of faults and their extent, their displacement-length relationships and the amount of strain accommodated by brittle deformation has been actively studied (Schlische et al., 1996). Isolated faults has a constant distance-length relationship (Walsh et al., 2003). A global data set of observed displacement and length relationships show a linear trend over more than 8 orders of magnitude in a log-log plot (Schlische et al., 1996). This relationship is given by $D=cL^n$, where D is displacement, c is a constant of rock properties, L is length and *n* is an exponent, of which the latter *n* value is controversial (Cowie et al., 1992; Schlische et al., 1996; Rotevatn et al., 2012).

CHAPTER 3 Theoretical background of analogue modelling

3.1 Introduction

This chapter gives an overview of previous work and literature concerning structural analogue experiments. The accumulation of displacement and fault length in a deformed medium is dependent on the formation of slip surfaces. The processes of which larger extensional faults form and grow by the interactions and linkage of smaller fault planes has been and are still actively studied in the field (Cartwright et al., 1995; Schlische et al., 1996; Bastesen et al., 2010), in seismic data (Yielding et al., 1991; Fossen et al., 2000; Fisher et al., 2001; Osmundsen, 2002; Ehrlich et al., 2004; Rotevatn et al., 2011), in experimental studies (Withjack et al., 1995; Fossen et al., 1996; McClay, 1996; Koyi, 1997; Clifton et al., 2000; Gabrielsen et al., 2001; Mansfield et al., 2001; Lindanger et al., 2004) and how these structures are scaled accordingly (Cowie et al., 1992; Fossen et al., 1996; Schlische et al., 1996; Ackermann et al., 2001).

A wide range of techniques and materials has been used in experimental modelling in order to reproduce deformation structures. The pioneering experiments (Hall, 1815; Cadell, 1888) studied compressional regimes and lay the base for further experimental modelling. Among first to model extension was Mead (1920). Previous work regarding the extensional regime in the later years as well as plaster modelling at the University of Bergen will be in focus.

3.2 Theoretical background

3.2.1 Modelling

Stüwe et al. (2012) define three properties to define a model to be good: “It should describe a large set of observations with a comparably small set of parameters. A good model must be useable as a tool to make predictions about fact that have not been observed yet. It must be possible to test a good model by making new experiments or observations”. A good model should give an understanding of nature and may aid the prediction of how the geology will look in the field.

3.2.2 Scalability

According to Hubbert (1937), in order to produce structures similar to nature in a smaller scale, one need to use materials that show great weakness as opposed to great strength as its natural counterpart. Hubbert refers to Galileo Galileis *Two new sciences* where the scalability of materials, flora and fauna is discussed. Galileo states that it would be impossible to scale up a medium without increasing its strength, or it would not be able to hold up its own weight. Hubbert concludes that "small bodies of a given material are strong; large bodies of the same material are weak, and the larger the body the greater its weakness". The properties of a scaled medium must be scaled accordingly in the different dimensions as length is scaled along a one-dimensional lineation, an area is scaled in two dimensions and a volume is scaled in three dimensions. Therefore, a weak material at a small scale is needed in order to produce structures similar to those found in the crust at a large scale. Hubbert (1937) defined three degrees of similarities:

i. Two mediums are geometrically similar when all corresponding lengths and angles within the bodies are proportional and equal. The bodies have the same form.
ii. Two mediums are kinematically similar if they are subject to similar deformation during the similar time scale, in proportion, required for the same amount of deformation to occur. The motion of the bodies is similar.
iii. Dynamic similarity considers the masses of bodies and the ratio of forces acting upon the corresponding particles in two bodies. The coefficient of cohesion and the coefficient of internal friction in the two bodies are the same for dynamically similar bodies.

Two bodies are geometrically and kinematically similar if their configuration of form, mass and acting forces has the same orientations and proportional magnitude (Hubbert, 1937).

3.2.3 Scaling of sand, clay and plaster

The grain sizes, physical properties and intergranular processes are difficult to scale correctly. Clay and sand are well-suited materials for generating nature like structures, however the size-variations of the generated structures is relatively small and a problem arises when it comes to preserving the end model. Granular shear processes form fault zones in analogue sand models without fracturing of grains, which does not represent nature accurately (McClay, 1996). Analogue fault modelling in sand thus produces relatively wide fault zones rather than a fault plane. The fine-grained plaster models have a cohesive strength until brittle

deformation occurs, leading to a narrow fault plane with visible associated small-scale structures. The cohesion of natural rocks is neglected in sand experiments, while plaster and clay has a larger cohesive strength than natural rocks when scaled up (Fossen et al., 1996).

Ultimate tensile strength

Coffin et al. (1964) presented plaster of Paris to be an effective material for dynamic testing for several reasons. Plaster of Paris has a high ratio of compressive to tensile strength. Low modulus of elasticity and low tensile strength require relatively small loads for brittle deformation to occur, which is suitable when deforming a medium under its own weight. Plaster of Paris has a linear stress-strain relationship for both compression and tension. The compressive strength, density, tensile strength and elastic modulus increase with decreasing proportions of water. The compressional and tensile strengths were tested on solidified samples of plaster with a plaster to water ratio of 1.54. The strengths are tested on a certain brand of plaster of Paris, and are therefore treated as an estimate for other brands. The ultimate strength in static test for plaster to water ratio 1.54 was 2410 psi (≈16.6 MPa) and 500 psi (≈3.4 MPa) for compression and tensile strength, respectively.

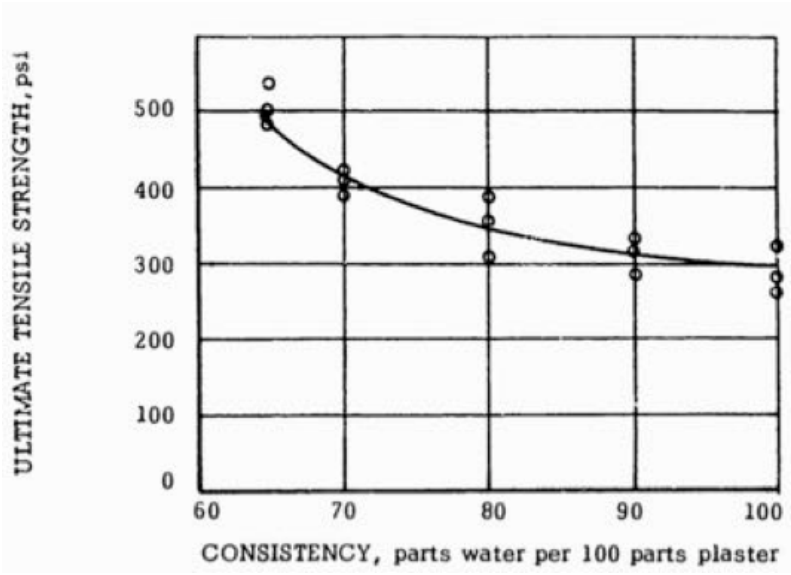

Fig. 4: The ultimate tensile strength vs. consistency (Coffin et al., 1964). 65 parts water to 100 parts plaster is a plaster to water ratio of ca. 1.54. 75 parts water to 100 parts plaster equals to a ratio of 1.33.

3.3 Previous analogue experiment studies

Experimental analogue modelling of crustal deformation has been done for centuries using various materials. In the following, key contributors to the field are presented chronologically followed by a description of a few of the pioneers within the field, as well as more recent experimental work using plaster. Most used materials in analogue experiments are clay and sand where dry sands is a frictional material, which represent brittle deformation in the upper crust (Koyi, 1997; Clifton et al., 2000; Atmaoui et al., 2006). The materials are used separately or as a combination. The physical and mechanical properties of plaster of Paris is described in Coffin et al. (1964) and is presented in short. Graveleau et al. (2012) provides a thorough review of sand box experiments with focus on experimental modeling of orogenic wedges.

Findings that is directly relevant for this thesis is presented along with the aim and short introduction of methods for the different studies.

3.3.1 Early experiments

The earliest experiments of deformation of the crust attempted to recreate the structures observed in folded strata in orogens. Various materials have been used as a modelling material. Amongst the very first to perform experiments on the structural evolution of the crust was Sir James Hall (1815). Hall used pieces of cloth stacked rather high as a representative for stratigraphic layers in a compressional regime (Fig. 5A). A door and weights overlay the cloth layers horizontally, while vertical walls were placed at two opposing ends. The force of a mallet pounding was applied to each of the vertical walls, forcing them to move towards each other. The cloth layers buckled and folded to form nature-like structures (Koyi, 1997).

Analogue models of fractures and folds were performed by Favre (1878), Daubrée (1879), Pfaff (1880) and Schardt (1884). A. Daubrée (1879) used various materials like glass, plaster, wax and strips of metal to study fracturing and folding at a small scale. Pfaff (1880) used sandbox experiments investigating the compressional regime using layers of wet sand and plaster of Paris.

One of the very first scientists to publish his investigations of crustal deformation using analogue modelling was Cadell (1889). He used sandbox experiments to model the formation of the thrust and fold systems in the Scottish Highlands. The experimental box, called a

squeeze box, was filled with alternating layers of sand, clay and plaster of Paris (Graveleau et al., 2012). Pressure was applied from one side using a vertical plate attached to a worm screw. The applied compression lead to buckling, folding and thrusting of layers, which was similar to structures found in nature.

Bailey Willis investigated the structures found in the Appalachians by using alternating layers of materials of different consistencies like plaster of Paris and waxes, which was overlain by a pressure block within a pressure box. Willis (1891) used damp clay and clay mixed with sand of various strength in his compressional experiments. The layers separated and formed hollow arches, which is not an accurate model for natural processes. Softer clay was used between the layers to allow slip between the planes, a process that is promoted when beds in nature are heavily folded.

Mead (1920) was one of the first to experiment with the extensional regime. Mead used an apparatus built of a rigid rectangular frame of gas pipe, which supported two clamps (Fig. 5B). A heavy sheet of rubber covered with a thin layer of paraffin is stretched between the two clamps. The relative position of the clamps could be moved to produce tension, compression, torsion and shear in the rubber sheet. The structures produced were visible in the paraffin coating. Structures produced in the tension experiments were tension cracks perpendicular to the rubber sheet, and produce at right angles to the direction of movement.

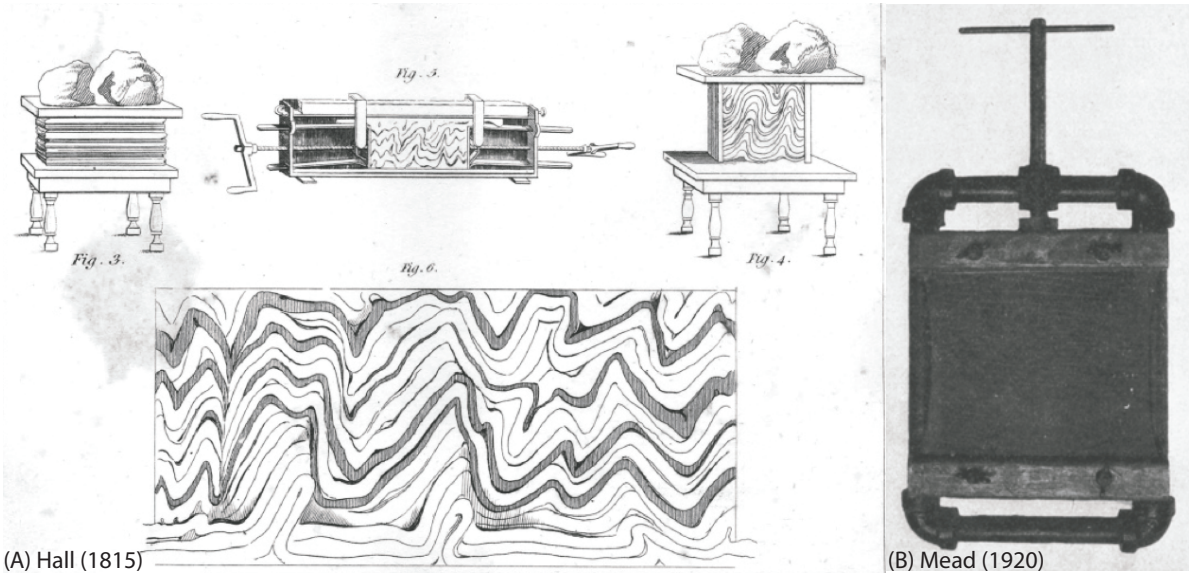

Fig. 5: Illustrations and photo of previous analogue model set-up. (A) Hall (1815). (B) Experimental apparatus from Mead (1920). Fractures produced by tension. Tension applied to a rubber sheet covered with paraffin produced tension cracks. Modified from (A) Hall (1815) and (B) Mead (1920).

Extensional analogue modelling

The structural evolution of extensional setting has been modelled by using various materials and experimental set-ups, of which sand and clay I mostly used and more recently plaster is mostly used. The German geologist Cloos' clay models (Cloos, 1955) stand out as the dimensional scalability of the models and rock properties were considered, which had not been common before. Cloos conducted mainly extensional experiments and used clay wetted with varying amounts of water in order to test the mechanical properties of the clay. The experimental set-up for non-rotational deformation by the stretching of a square wire-net underlying a square slab of clay is shown in Fig. 5C, the extension direction is diagonal to the square net. McClay et al. (1987) used quartz sand of grain size 700 μm to model the development of extensional fault geometries overlying varying basements (Fig. 6B). Mansfield et al. (2001) used plaster to model fault growth in a two-layer sequence of baryte and plaster with focus on surface deformation. Faults grew by repeating overlap, relay formation, breaching and linking with interacting fault segments. Their model set-up is illustrated in Fig. 6C.

Left: Experimental set-up

Right: Resulting model

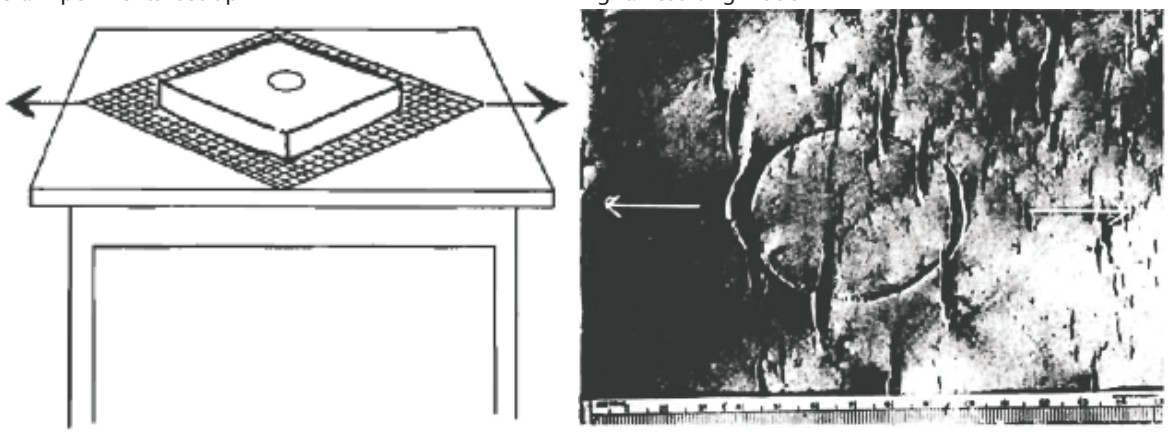

(A) Cloos (1955): Clay experiment

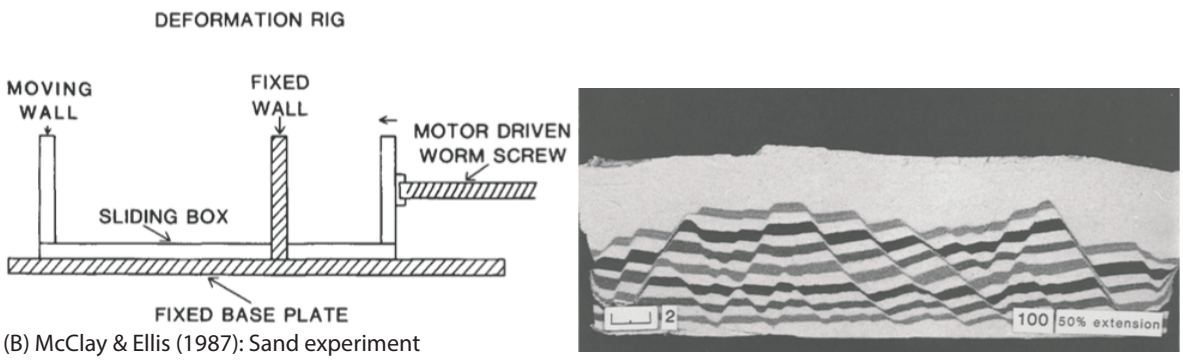

(B) McClay & Ellis (1987): Sand experiment

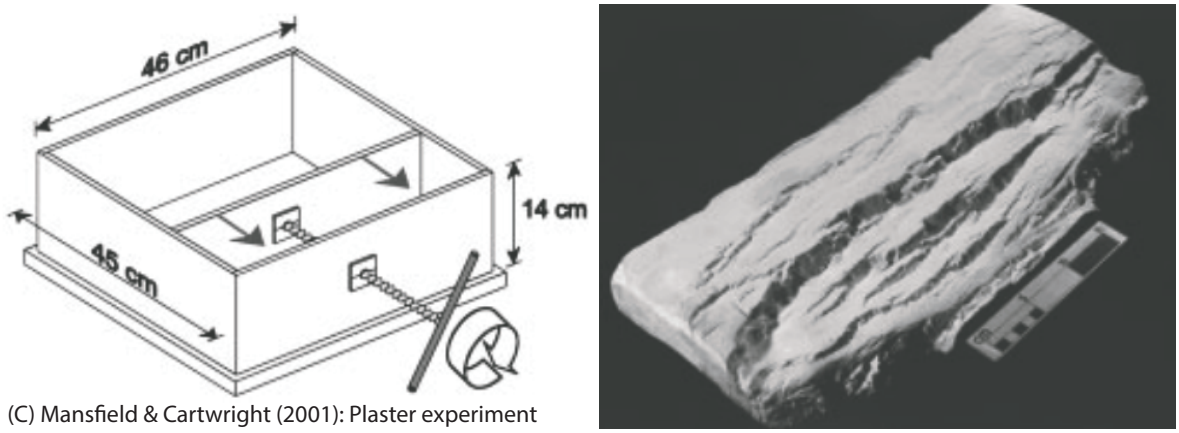

(C) Mansfield & Cartwright (2001): Plaster experiment

Fig. 6: The experimental set-up and results showing extensional deformation structures of a selection of clay, sand and plaster models. (A) Clay experiment set-up on the left and a finished model with tension fractures on the right from Cloos (1955). The arrows indicate extension direction. (B) Experimental set-up by McClay et al. (1987) on the left and a finished sand model on the right. (C) Experimental set-up of plaster model from Mansfield et al. (2001) on the left and a finished model on the right showing surface deformation. Modified from (A) Cloos (1955), (B) McClay et al. (1987) and (C) Mansfield et al. (2001).

3.3.2 Plaster modelling at the University of Bergen

John Sales, whom together with Roy H. Gabrielsen established the first analogue plaster modelling lab in Norway, introduced analogue plaster modelling to the University of Bergen. The analogue plaster models produced is presented in the Master Thesis of Odinsen (1992). The experimental description provided in Sales (1987) is included in this section as it is accounted as the precursor for experimental modelling at the University of Bergen. The experimental box set-up (Fig. 7) is the same as the wide box used in this thesis and is described in chapter 4.1.1.

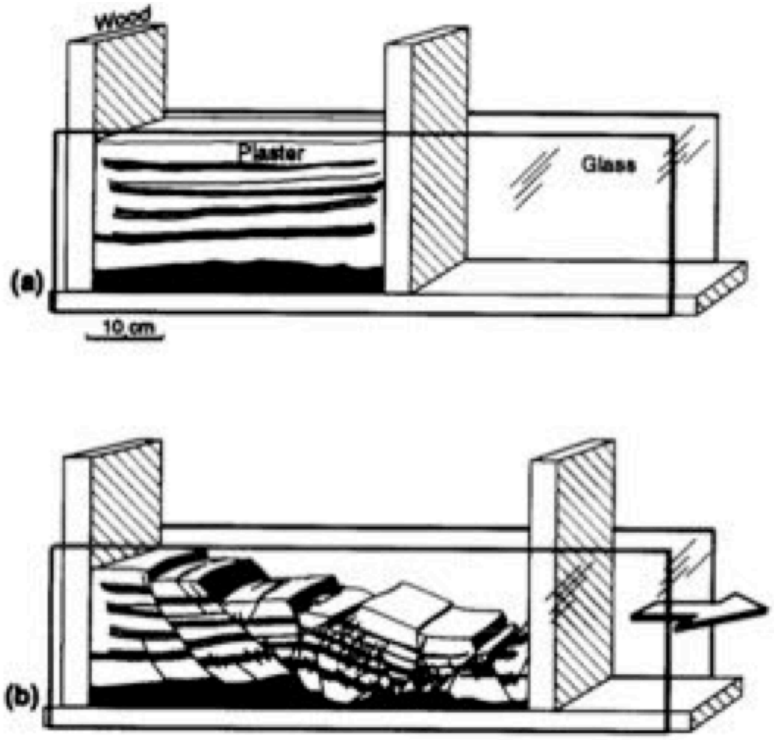

Fig. 7: Illustration of the experimental box set-up used for the experiments presented in Fossen et al. (1996). (a) The experimental box filled with a baryte base and a plaster cover with marker layers added. (b) The moveable vertical wooden wall was moved to the right.

Sales (1987) provide a concise description of the theory of mechanical scale models and discuss materials used for modelling. Sales promote stitching wax, certain clays, partly solidified plasters and baryte mud fluid as suitable modelling materials. These materials are viscoelastic materials that shear and flow during extension and can model structures found in nature. Experimental approaches for various structures like décollement, thrusts, extensional fault blocks, strike-slip wrench faults, salt domes and glaciers are described to be replicable. The extensional models described in Sales (1987) are made with a layer of plaster on top of a relatively dense baryte layer. The plaster to water ratio was ca. two parts plaster to one part

water. The layer thicknesses in the extension experiment are ca. 5 cm and 7.6 cm for baryte and plaster mixtures, respectively.

Odinsen (1992) describes the structural development in extensional plaster models and test conditions for balancing and restoration of deformed sections. The first faults form after 5-10% extension and nucleate at the interface between the basal layer and the plaster cover proximal to the vertical moveable wall. The fault plane geometry fall into two categories, (1) the geometry is typically sub-planar as the faults form, and change to a more convex-upwards geometry as extension continues, (2) the fault plane is formed as a listric fault plane and keeps this geometry or develop a more wavy fault plane. Accommodation structures form synthetic to the main fault zone.

Fossen et al. (1996) describe three plane-strain extensional plaster experiments with slightly different boundary conditions. The experimental set-up and materials are the same as the wide box used for this thesis (Fig. 7 and Fig. 8). The plaster mixture was similar for the three experiments, while the basal layer properties varied. The basal layer of the first run was stiff baryte, the second of a softer baryte and for the third run five aluminium plates covered the interface between a soft baryte and the plaster mixture. The aluminium plates were cut to promote a block-formation similar to the configuration in the Gullfaks field in the northern North Sea. The large- and small-scale structural development and their geometric and kinematic relationships in pure extension were studied. The structures produced are similar to those found in naturally deformed rocks. A through-cutting fault plane is typically formed at β 1.25, or 25% extension. Two categories of fault morphologies are identified. The first category is lens-shaped geometries and the second category is associated minor synthetic faults with a steeper dip angle compared to the main fault zone. Main fault planes accommodate 60-70% of the total extension, while the ductile component and sub-resolution faults are estimated to account for less than 20-30%. Footwall collapse near the surface flattens the dip angle of the main fault plane in the upper part.

Gabrielsen et al. (2001) describe characteristic stages of the development of a fault zone and secondary structures as horses and extensional duplexes in the extensional regimes using analogue plaster models. A more detailed description of the presented characteristic stages is given in Appendix A: Definitions. The experimental set-up and materials is the wide box set-up described and used for two experiments in this thesis. A difference lies in the basal layer material. Gabrielsen et al. (2001) used different configurations of wooden pieces and a soft

mixture consisting of baryte and water. According to the experiments presented in Gabrielsen et al. (2001), a master fault is typically formed at 5-12% extension, where tip-line bifurcation processes are active. Asperity bifurcation processes are active as the fault plane is sheared, which in their experiments typically is after 10-25% extension. A fault plane with irregularities may promote the formation of first-generation asperity bifurcation horses.

Lindanger et al. (2004) used analogue modeling with plaster of Paris to model hanging-wall deformation above ramp-flat-ramp extensional faults and to test the validity of their structural reproduction in reflection seismic data. The experimental set-up is the same as described in Fossen et al. (1996). Their analysis show that shallowly dipping master faults produce multiple fault branches through processes such as asperity bifurcation or fault splaying within the footwall or hanging-wall. Early formed structures in the lower hanging-wall are sometimes cut at a later stage, which produces a complex fault pattern. An irregular fault plane enhances the structural complexity in the model, along with the number of master faults in the model and their processes of formation.

CHAPTER 4 Methodology

A description of the experimental approach and the equipment and materials used for gravity-driven plane-strain plaster modelling of the extensional regime is presented in this chapter.

4.1 Materials and Equipment

4.1.1 Deformation box

Two deformation boxes of the same design in different dimensions are used for the experiments. The vertical walls of the box are made of two fixed glass plates (100x30x0.6 cm) and two moveable wooden plates (Fig. 8A). The base of the box is made from a wooden plate. A handle is fixed to each of the vertical wooden walls. The width of the short walls and base plate is 16 cm and 11 cm for the wide and narrow box, respectively. The three wooden plates are lined with rubber bands, which act as a buffer against the glass walls to seal the box. The box is fastened using wedges of wood and a vice, which together with two opposing wooden pieces tighten the gap between the glass plates and the rubber bands. The inside of the box is sprayed with canola oil, which reduces friction along the sides of the moveable wall. One of the short walls is pulled manually along the horizontal base for unilateral extension, respectively.

4.1.2 Basal layer

A mix of baryte ($BaSO_4$), water and food colouring is used to form different structural basement templates and to seal the box on the inside as well (Fig. 8B). The baryte does not solidify and can be reused. The ductile basal layer may accommodate space problems related to deformation in the plaster cover. The barite mixture is more viscous relative to the plaster mixture at the start of experiment and provides a stable layering of the model. The interface between the plaster mixture and the basal barite mixture may act as a sliding plane, which in turn may enhance deformation. Adding canola oil can reduce friction along this plane. Different geometries of the basement template can affect the deformation pattern.

4.1.3 Marker stripes

Marker stripes are used as a reference for displacement on photos taken throughout the experiments and in the solidified model. The stripes are passive markers, which can be used to identify piercing points. In previous experiment and in the early experiments of this thesis, the marker stripes were made of a mixture of carbon powder and water. This gives clear

stripes, but they can easily be affected by water percolating through the plaster. If it is mixed too thin the carbon powder often does not give coherent stripes, but rather aligned dots of black powder, which can be challenging during data interpretation. An adjustment was made, and the carbon powder was replaced with acrylic paint. The replacing mixture consists of blue acrylic paint mixed with water and is applied to the glass plates by a modified toothbrush after the plaster has been poured into the box (Fig. 8B). The acrylic paint gives a clear colour as well as coherent stripes. It also sticks to the toothbrush better, which limits the bleed when the toothbrush is dipped into the plaster when adding marker stripes. As the marker stripes are applied manually to the glass plates, they are not directly comparable from one side to the other. The orientation and thickness of the stripes varies as well as the blank space between them, meaning that an apparent change in vertical thickness and dip angle at a point in deformation history must be compared against the marker stripes in the unstrained model.

4.1.4 Plaster of Paris

Formula Saint-Gobain produces the plaster of Paris used for the experiments under the brand name of Molda 3 Normal. The plaster has the chemical composition of $CaSO_4 \cdot \frac{1}{2}H_2O$ with a high gypsum purity of minimum 91% and has an off-white colour (Saint-Gobain, 2015). The plaster produces heat on setting in an exothermic process and has a linear expansion of 0.19 in a mixture with plaster to water ratio of 1.55:1 by weight. The final setting time is 39 minutes, meaning that the model is solidified and ready for analysis within a short hour. The ratio used in the experiments vary around 1.5:1 in volume and is specified for each experiment. Particle size of the plaster is measured by sieve analysis. Weight retained is 0.1% and 3% for mask sizes 200 µm and 100 µm, respectively. This means that 97% of the dry plaster has a particle size smaller than 100 µm, as provided by the product data sheet (Saint-Gobain, 2015). Particle-size analysis was performed by Lewry et al. (1994) on gypsum crystals prepared by wet methods (such as autoclaving) and dry methods (such as calcining) and are called α-form and β-form, respectively. They determined a mean particle size of 11.4 µm and 8.6 µm for α-form and β-form, respectively, giving an average value of 10 µm.

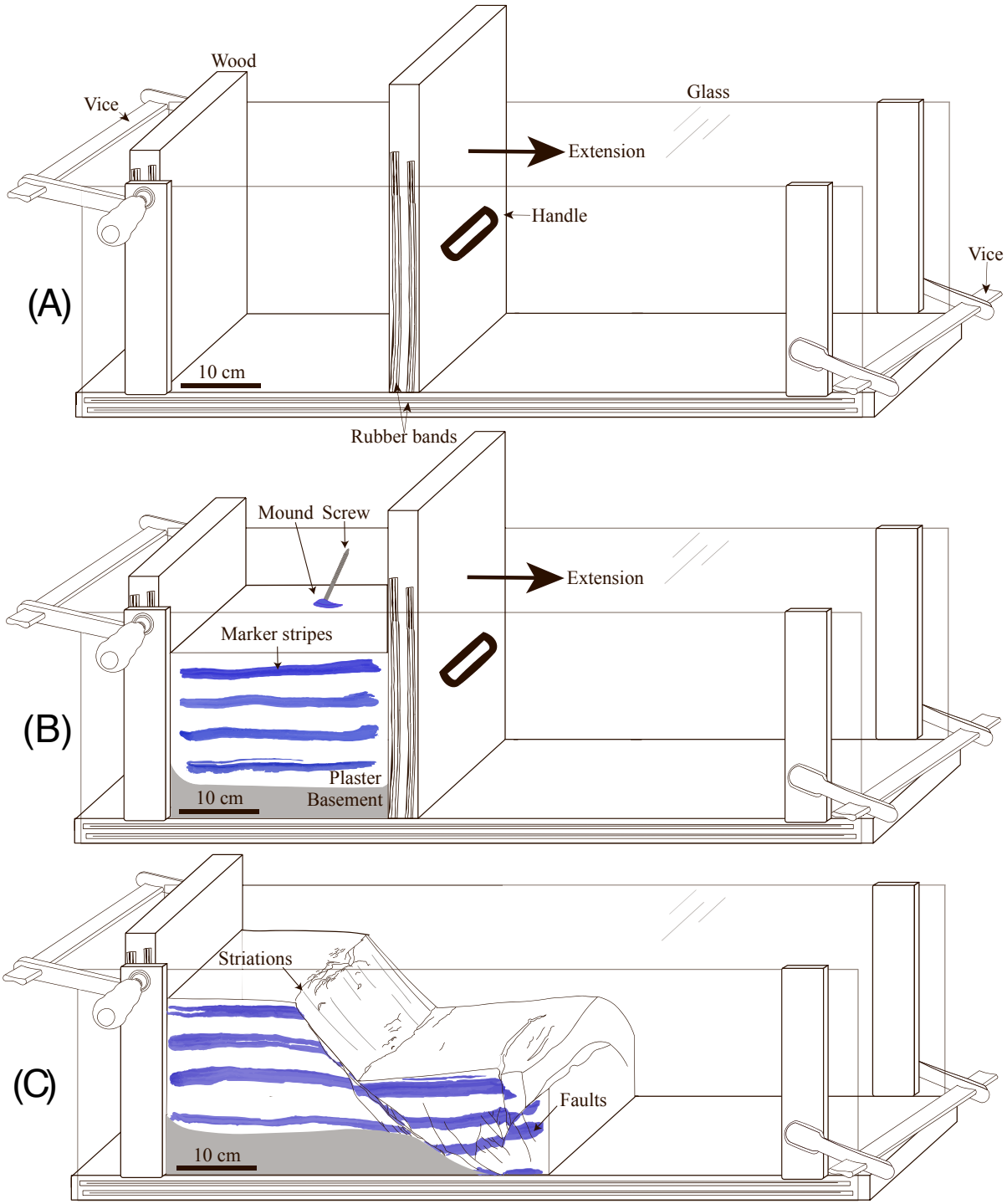

Fig. 8: A principle sketch of the deformation box and materials used. (A) Set-up of the deformation box used for plaster experiments. A handle is attached to the moveable wall, which will be pulled to the right along the horizontal base for extensional plaster experiments. (B) Deformation box with added basement of baryte, plaster mixture and marker stripes. Dipping a screw head to see if a mound is formed confirms the preferred plaster consistency. (C) A plaster model after extension, where the moveable vertical wall is removed.

4.1.5 Plaster consistency

The properties of the plaster mixture are dependent on temperature and the plaster to water ratio. Cold water is used in these experiments and the plaster to water ratio is measured for each experiment. The plaster solidifies relatively fast and therefore timing is crucial when performing these experiments. The plaster consistency must be just right, as the main driving force is gravity. When extending the length of the box, accommodation space is given. If the plaster is too soft, the deformation is ductile and the plaster will fill the available space without fracturing. If the plaster is too stiff, few or no structures are produced. The preferred plaster consistency is when one can make a small mound at the surface when dipping the head of a nail (Fig. 8B). At this point the plaster has a consistency of thick pancake batter. At this consistency it is expected that the plaster will flow in the extension direction, leading to a structurally complex model with both large- and small-scale structures (Fig. 8C).

4.1.6 Data collection

Three Nikon D800 cameras, each with an AF-S Nikkor 50mm f/1.4G lens is used to document deformation in the experiments at a shutter speed of 1/80 sec. Photos are taken at a rate of 3.9 photos per seconds. The image size is 7360 x 4912 pixels. Two cameras are oriented perpendicular to the glass walls to capture the structural evolution in the profile plane. A third camera overlooking the deformation box captures surface deformation.

4.1.7 Data processing

Photographs of the experiments are used to study deformation at different stages and intervals, and can be compiled to short videos showing the deformation history. By studying photos, videos and the solidified models in detail, the deformation patters are investigated.

4.1.8 Determination of extension

The amount of extension is described by elongation (ε) and stretching factor (s=β) (Fossen, 2010). The elongation is the amount of length

$$\varepsilon = \frac{L - L_0}{L_0} \quad (1)$$

where L_0 is the initial length and L is the extended model length

$$\beta = 1 + \varepsilon \quad (2)$$

where ε is elongation.

Combining elongation and stretching factor can be simplified to,

$$\beta = \frac{L}{L_0} \tag{3}$$

where L_0 is the initial model length and L is the extended model length. The ratio represent a constant of proportionality of length between two models, the value of which is larger than one if the body has been enlarged compared to the original length and is less than one if the body has been reduced. The definition of the β-factor provided in equation 3 is based on the constant of proportionality (λ) in Hubbert (1937).

The amount of extension can also be expressed in per cent. For this thesis, an extension of 100% would represent a doubled initial length, or β=2. The amount of extension is easier to compare between experiments when the per cent extension is based on the initial length, which is relatively similar, than the final length of models. Thus, the majority of experiment presented in this thesis does not reach 100% extension.

The average extension rate is calculated using the elongation and the time in seconds. The extension rate is an estimate based on the time signature provided by the cameras.

$$\dot{\epsilon} = \frac{\varepsilon}{t} \tag{4}$$

where ε is elongation (mm) and t is time (s)

4.2 Experimental approach

4.2.1 Step-by-step

1. Box is set up and fastened (Fig. 8A)
2. Basement and canola oil added (Fig. 8B)
3. Plaster is mixed and poured into the experimental box
4. Marker stripes added
5. Plaster consistency monitored by using the head of a nail
6. Cameras are set
7. Start of extension: one wall is set in motion for unilateral extension
8. End of extension: model is left to solidify before it is removed from the box (Fig. 8C).

4.2.2 Experimental description

A basal layer of baryte mixture is smeared on the base of the box and along cracks to prevent leakage (Fig. 8B). The geometry and thickness for the baryte layer varies between experiments in order to investigate its subsequent effect on the plaster cover. The inside of the box is sprayed with canola oil, which reduces friction along the sides of the moveable wall. Canola oil is not added to the interface between the plaster mixture and the moveable vertical wall to preserve adhesion and to reduce the chance that the plaster slips off the moveable wall during the experiment. The plaster is mixed and poured into the box and marker stripes are added. Timing is important as the plaster sets relatively fast and water accumulated on the surface may make the evaluation of plaster consistency difficult. Surface water may also affect and smooth the structures formed during the experiment. The consistency of the plaster mixture controls the start of the experiment and is tested continuously. The experiment start when one can make a mound when dipping the head of a nail into the plaster. The preferred consistency usually means that the plaster will behave brittle and produce structures similar to those found in the upper crust. The extension rate is controlled manually, and strain rate is not constant during the experiment. An erratic movement may be similar to how seismogenic faults behave in nature, according to Fossen et al. (1996). One vertical wooden plate is fixed during unilateral extension experiments. The extension is terminated when the plaster no longer flows in the direction of movement. At this point structures are no longer produced. The tension of the vices and other fastening equipment is partially released and the model is left to solidify (Fig. 8C). The model is ready for analysis within a few hours.

CHAPTER 5 Results

5.1 Introduction

The purpose of analogue modelling is to study fault evolution in laboratory conditions where initial and boundary conditions are set and monitored. A total of 14 extensional models were made of which five experiments are selected for further analysis. A total of 52 experiments were performed for the extended plaster modelling group with regards to strike-slip, contraction and extension.

The five experiments presented in this thesis are chosen for their variations in structural complexity and fault growth patterns as well as the following criteria:

i. The volume of the baryte basal layer and plaster cover is constant throughout the experiment.
ii. The experiments are well documented by photographs.
iii. Marker stripes can be traced during the experiment

The initial length the selected models are similar, but not equal for all experiments. The basal layer geometry varies between experiments as well as the total extension and the mean extension rate. An overview of specifications for the experiments is provided in Tab. 1.

One of the wooden vertical walls is pulled out during unilateral experiments, which means that unilateral experiments are extended in one direction to produce dip-slip dominated faults. The unilateral experiments are divided into two groups. Multiple master faults form and interact in the experiments of group 1, while group 2 model the evolution of a single master fault. Group 1 consists of experiments E1 and E2, which are made in the wide box set-up with marker stripes of black carbon powder mixed with water. Group 2 consists of experiments E3, E4 and E5, which are made in the narrow box set-up with marker stripes of blue acrylic paint mixed with water.

The profile planes are drawn from each side of the model and are labelled A and B. The visible structural evolution is described separately in tables and illustrated by figures showing critical points in deformation history. The deformation is summarised at the end of the

description for each experiment. For definitions of terms and processes used to describe the fault development, see Appendix A: Definitions. The results are discussed in chapter 6.

Tab. 1: Overview of experiments described in this thesis.

Experiment	Geometry of basal layer	Initial length (L_0, cm)	Final length (L, cm)	Mean extension rate ($\dot{\epsilon}$, mm s-1)	Stretching factor (β)	Description, subchapter/Fig.
E1 (03-13) wide box	Horizontal $h \approx 6$ cm	30	51	7.7	1.70	5.1.1/ Fig. 10 and Fig. 11
E2 (06-13) wide box	Horizontal $h \approx 2$ cm	34	66	9.7	1.94	5.1.2/ Fig. 13
E3 (50-14) narrow box	Ramp $\alpha \approx 13°$	30	46	2.4	1.60	5.1.3/ Fig. 15 and Fig. 16
E4 (51-14) narrow box	Horizontal $h \approx 6$ cm	30	41	2.4	1.37	5.1.4/ Fig. 19 and Fig. 20
E5 (52-14) narrow box	Horizontal $h \approx 6$ cm	30	52	11.6	1.73	5.1.5/ Fig. 23 and Fig. 24

Descriptions of plaster experiments

For simplicity,

i. The descriptions of side A and B of the same model are organised in separate sections along with an overview of the amount of extension expressed by the beta-factor (β) and a reference to the corresponding illustration.
ii. The marker stripes are labelled alphabetically from top to bottom. If there are three marker stripes in a model, the uppermost stripe will be referred to as A, the middle stripe B and the lowermost stripe will be C.
iii. Faults indicated in the figures are numbered accordingly to the relative time of formation, meaning that a fault marked F1 formed first, or was first apparent in the model, and subsequently F2, F3 and so on. This label is provided at the first appearance after formation in the figures.
iv. Faults that are referenced in the text are coloured in the corresponding figure and labelled at the stage of formation with an arrow and text in the same colour. The fault planes are coloured in the subsequent stages as well in order to be recognised at later stages without a direct label.
v. For unilateral experiments the extension direction is to the right.
vi. The dip direction for described faults is towards the right in the extension direction, unless states otherwise, while antithetic fault is described to have a dip towards the left.

5.1.1 Group 1: Experiment E1

Laboratory reference	03-13		
Experiment box	Wide model		
Marker stripes	Water and black carbon powder		
Basal layer	Horizontal geometry of barite layer, 6 cm thick		
Plaster to water ratio	1.33	ε	21 cm
Initial length	30 cm	$\dot{\epsilon}$	7.7 mm s^{-1}
Final length	51 cm	β	1.70

Comments: Plaster cover column is 13 cm. The estimated plaster mixture volume is 6.24 L.

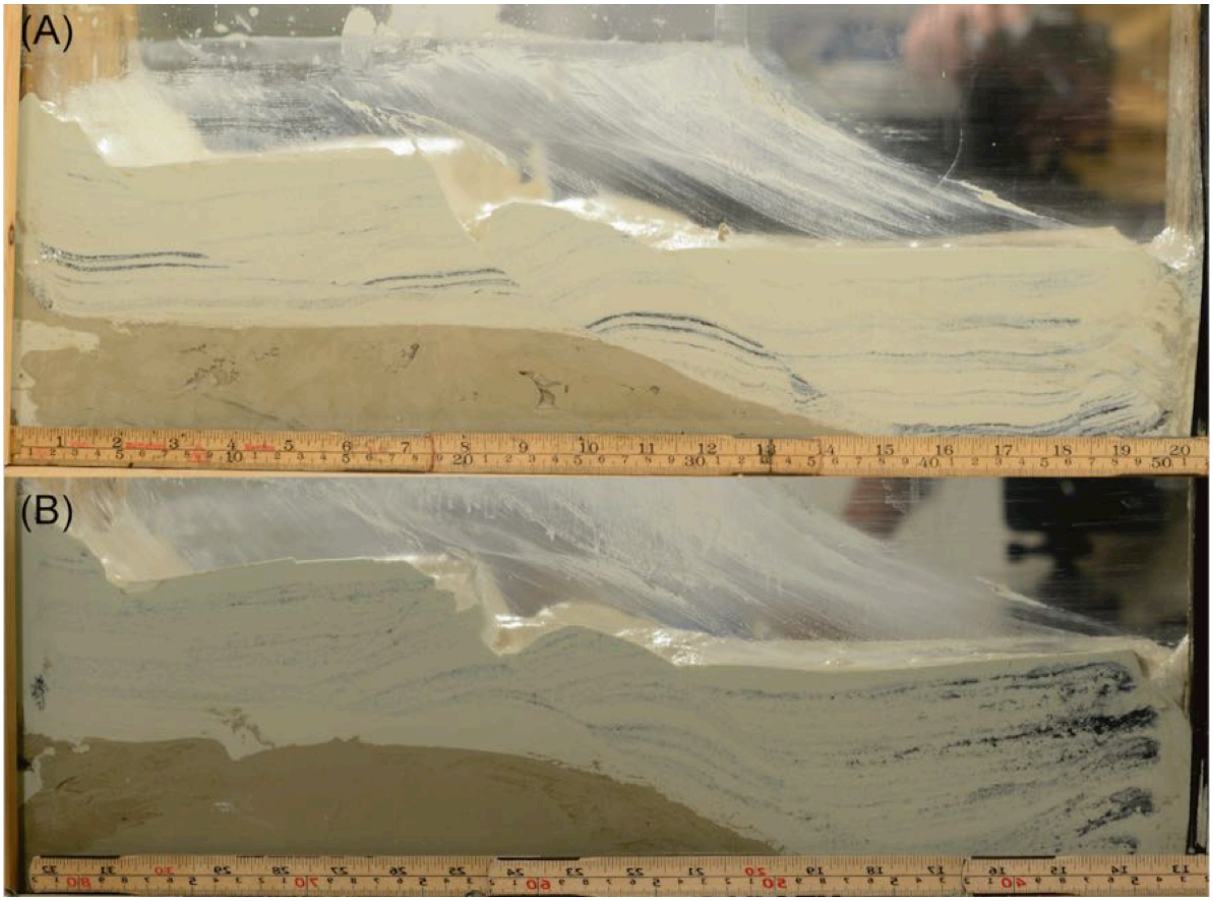

Fig. 9: Photographs of the final stage of model E1 at β 1.70 for side A in (A) and for side B in (B). The scale bars represent cm on the lower row and inches in the upper row.

Description of fault development in E1 Side A

β 1.00 (Fig. 10A): Five lines (A-E) are traced from photos shot during the experiments and will be used as a reference for the unstrained state relative to the following descriptions.

β 1.00-1.15 (Fig. 10B): The barite layer is thinning in the right side of the model (towards the moving wall) to form a ramp on which two planar normal faults called F1 and F2 form almost simultaneously and propagate upwards. F1 is planar and cuts the surface with an angle of 30˚. F2 does not reach the surface and only show displacement in the lowermost marker layer. The vertical overlap between F1 and F2 causes a clockwise rotation similar to a releasing overlap zone. The footwall of F1 seems stable, whilst the hanging wall keeps moving steadily.

β 1.15-1.23 (Fig. 10C): At this point the barite layer stops moving and the rightmost 5 cm of the once flat barite layer has formed a ramp, which dips with roughly a 30° angle and ends at the 37 cm mark. The minor F2 fault plane curves and intersect the master F1 plane to form an extensional horse I, which rotates anti-clockwise. The combined fault plane of F1 and F2 is called F1', and this cuts through the extensional horst and is the most active fault plane at 23% extension, leaving the lowermost part of F1 less active. Smaller scale structures develops; for example a rider, which can be seen in the footwall where F1' cuts the surface. An extensional duplex is seen along the roof fault of F2, which is short lived as these and other minor irregularities associates with the linkage of F1 and F2 along the segmented F1' is smeared out.

β 1.23-1.35 (Fig. 10D): The F1' plane propagate down to form an irregular geometry above horse I. To the far left into the footwall, a listric fault F3 forms from the surface and propagates down. The low-angle portion F3 plane acts as a detachment fault on which the hanging wall can rotate anti-clockwise. Simultaneously, the front end of the F2 hanging wall is transported over the ramp and is folded to a very gentle anticline. A second extensional horse forms in the hanging wall of F1' with a minor curved roof fault, F4.

β 1.35-1.60 (Fig. 10E): At this stage the rotated fault blocks between F4 and F1 compartmentalises by three faults, F5, F6 and F7. The two normal faults F3 and F5 are dipping towards each other to form a graben, while F5 and F1' is dipping in opposite directions to form a horst. The antithetic fault F6 is formed sub-parallel to F5 in the graben, leaving F5 less active. At around 6 cm displacement accumulated along F1', the newly formed F7 cuts the horst between F5 and F1' with a 30° angle dipping right and propagate

downwards to link up with the F4 just above the ramp formed by the baryte layer. Displacement along F1' is then less active, and the displacement is instead accumulated along F7.

β 1.60-1.70 (Fig. 10F): At this stage F7 continues to grow as a curved listric fault above the ramp in the baryte layer, producing an anti-clockwise rotation within the hanging wall of F7 and a minor antithetic fault with a small displacement. The F1' plane is rotated to a generally lower angle. In addition, many very small right-dipping faults form near the base between F7 and F8.

Description of fault development in E1 Side B

β 1.00 (Fig. 11A): Five lines (A-E) are traced from photos shot during the experiments and will be used as a reference for the unstrained state relative to the following descriptions.

β 1.00-1.15 (Fig. 11B): The basal layer is moving out to form a ramp with dip angle 20° towards the right. The first faults F1 and F2 are initiated near the interface between the plaster cover and the baryte with a dip angle of 45° above the ramp geometry. A few minor faults cut the surface and are limited to the top of marker stripe A. Initially many minor sub-parallel faults form in a zone, where F1 cuts through to a master fault plane. F1 is an uneven fault plane, which cut the surface and reaches the basal layer and follows the ramp geometry. The displacement at the surface is 1.5 cm at this point.

β 1.15-1.23 (Fig. 11C): At this stage the area with most deformation is directly above the baryte ramp slope to the left in the model. Many minor faults form in the zone directly above the ramp, while ductile deformation within the small blocks occurs along the base as the plaster cover rotates anti-clockwise along F1 and moves towards the right. Displacement along F1 is here 4.5 cm and the fault plane is more planar due to smearing along the fault plane. Further into the footwall of F1, a curved fault plane forms near the surface and propagate downwards (F2 with a dip angle of 60° near the surface and 30° through marker stripe D). Some displacement is visible along the middle parts of the fault plane, but decrease towards the tips.

β 1.23-1.35 (Fig. 11D): Displacement along F2 increases to 2 cm at the surface and the fault plane propagates downwards to the right, forming a listric fault plane. F2 follow the ramp geometry around 1-2 cm above the interface between the basal layer and the plaster cover. The minor faults along the base of the plaster cover are enclosed in the footwall of F2 and

remain passive throughout the rest of the experiment. The hanging wall rotates anti-clockwise near the steeper part of F2, while the front of the hanging wall is stretched as it flows over the ramp geometry. In the footwall of F1, three minor faults have linked together to form F3, which cuts semi-parallel to the F1 plane, F3 does not accumulate significant displacement and F1 is the most active fault plane of the two. Antithetic faults F4 and F5 form in the transition from a rotational movement to extensional movement over the ramp. F6 is starting to propagate upwards from the fault plane of F2 above the ramp. While the hanging wall of F2 slides out and over the ramp, F1 and F3 is subsequently rotated anti-clockwise and pushed towards the right to form a fault plane that has a more shallow dip near the surface and base and a steeper dip along the middle.

β 1.35-1.60 (Fig. 11E): Displacement along F2 is 6 cm. The hanging wall of F2 is divided into a graben and a horst, and both are transported down the detachment fault F2. F6 has propagated upwards and cut the horst, forming a block enclosed by F6 and F1. Normal faulting occurs within the graben as F6 accumulate displacement, where F7 has the largest displacement of 0.5 cm. The semi-solidified plaster cover is slipping off the vertical moving wall, which leads to some compression in the rightmost end of the model, where a normal fault called F8 form in marker stripe C.

β 1.60-1.70 (Fig. 11F): As extension continues, the most active fault is F6. Displacement along F6 at this final stage is 4 cm. The last faults to form are another normal fault F9, which is parallel to F8 and a left-dipping normal fault (F10) forms as the plaster that slipped off the vertical moveable wall moves down.

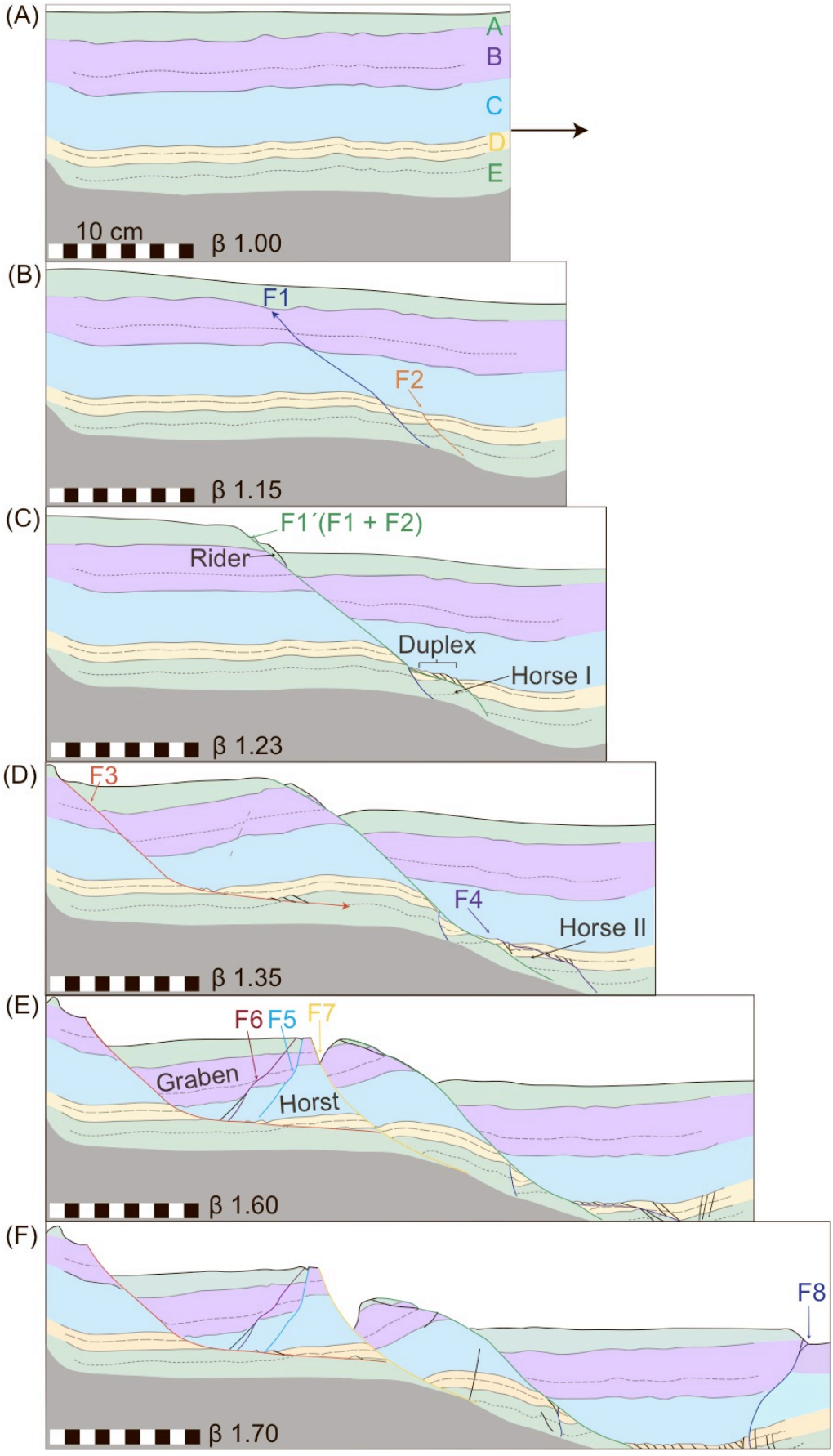

Fig. 10: Structural evolution of model E1 seen in profile plane A.

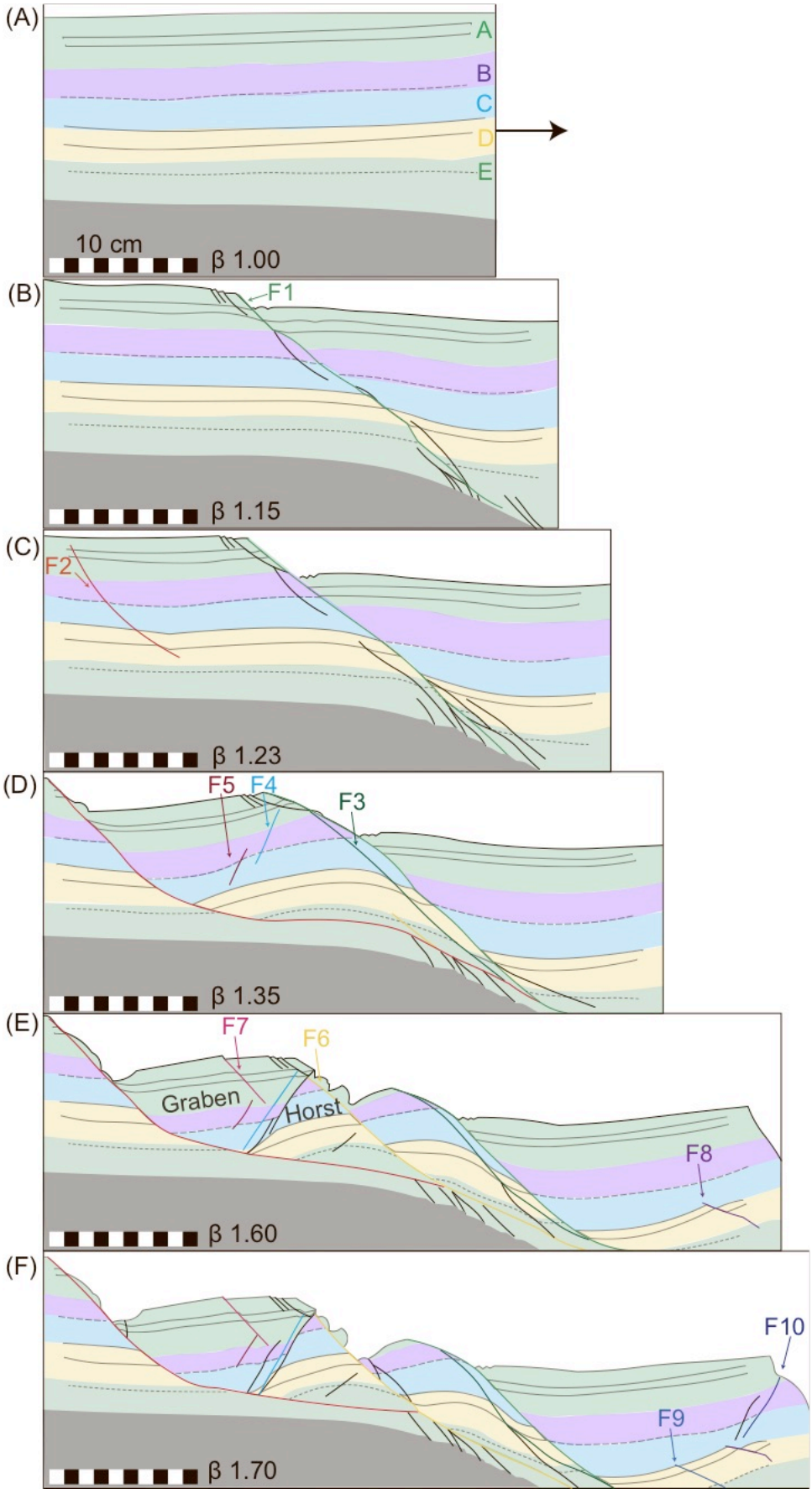

Fig. 11: Structural evolution of model E1 seen in profile plane B.

Summary of E1 side A and B

Three right-dipping major fault planes form. The major faults are not numbered equally due to a slightly different formation sequence from side A to B. The corresponding faults are F1A/F1B, F3A/F2B and F7A/F6B. The formation patterns of the fault planes are very similar from side A to B, however side B seems to be slightly ahead of side A when it comes to timing.

The first major fault form within the first 20% of extension with an angle of 30-40°, steepening downwards. The second large fault plane forms further into the footwall with a listric geometry on which the hanging wall rotates anti-clockwise. The internal anti-clockwise rotation is larger along the left margin within the hanging wall relative to the right margin, leading to a zone of antithetic fault trajectories, of which a few fault planes are apparent and illustrated in Fig. 10E-F and Fig. 11D-F. A graben is enclosed by the leftmost listric fault plane and the antithetic fault planes, while a horst structure is enclosed by the antithetic faults and the first formed master fault. As extension continues the horst is cut by a listric fault plane, which accumulate a relatively large amount of displacement. The final maximum fault zone is ca. 3 cm wide, measured perpendicular to the faults.

The accumulated displacement along the fault plane on the surface for F1A/F1B, F3A/F2B and F7A/F6B is 8 cm, 5.5 cm and 4.5 cm, respectively. The heave of the larger faults has been measured to be quite similar for side A and B with 14.8 cm. The total extension in the horizontal plane is 21 cm. The accumulated heave equals to 70% of the total horizontal extension for the largest faults. The maximum fault core width is 3-5 mm.

Side A		Side B	
Faults	Distance	Faults	Distance
F1 and F3	14 cm	F1 and F3	12 cm
F3 and F5	13 cm	F2 and F4	14 cm
F3 and F7	14 cm	F4 and F3	4 cm
F1 and F8	23 cm	F4 and F6	4 cm
		F1 and F10	20 cm

The distance between the main faults are measures in the horizontal plane and near the surface. F1A and B, F5A, F7A, F3B, F4B and F6B all form in the area above the ramp geometry.

5.1.2 Group 1: Experiment E2

Laboratory reference	06-13		
Experiment box	Wide model		
Marker stripes	Water and black carbon powder		
Basal layer	Horizontal geometry of barite layer, 2 cm thick		
Plaster to water ratio	1.66	ε	32 cm
Initial length	34 cm	$\dot{\epsilon}$	9.7 mm s^{-1}
Final length	66 cm	β	1.94

Comments: Plaster cover column is 16.75 cm high. The estimated plaster mixture volume is 9.12 L. Photos from side B are not available.

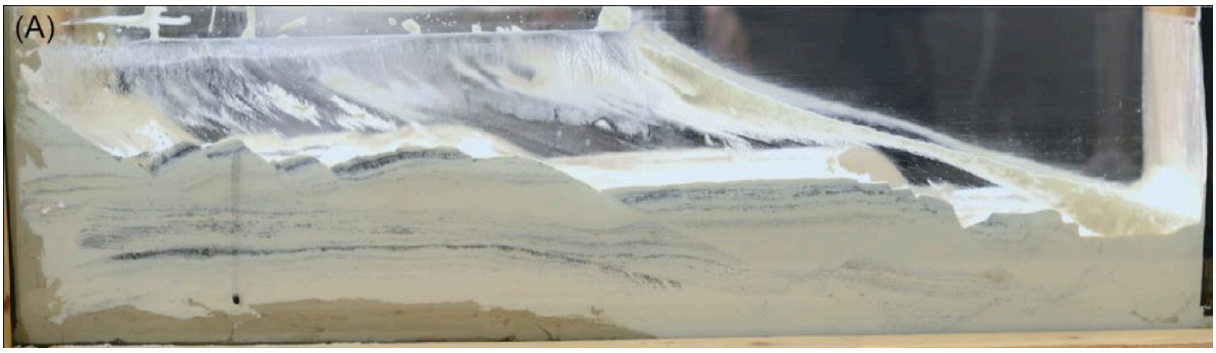

Fig. 12: Photographs of the final stage of model E2 at β 1.94 for side A in (A).

Description of fault development in E2 Side A

β 1.00 (Fig. 13A): Five marker stripes (A-F) are used as reference for displacement.

β 1.00-1.16 (Fig. 13B): Three visible faults form, two in the rightmost part of the model in marker stripe F and one cutting the surface. F1 cuts marker stripe F at a 45° angle, while F2 has a steepening dip of ca. 15° to ca. 30° towards the right. F1 is intersected by F2 in the top end. The length of F1 is 4 cm and F2 is 7 cm. F3 propagate downward from the surface at a 40° angle for 2 cm.

β 1.16-1.23 (Fig. 13C): F2 is propagating upwards to reach marker stripe C and to form a ramp-flat-ramp geometry, with dip angles of ca. 30° in the tips and a shallower portion of ca. 12° in the middle. The length of F2 is 14 cm. Two normal faults of ca. 1.5 cm length form at the surface, F4 dips at a 50° angle and F5 dips at a 60° angle.

β 1.23-1.32 (Fig. 13D): A master fault F3 propagate downwards at an angle of ca. 30° for 18 cm to reach marker layer E, where the dip angle increases to 65° for ca. 2 cm. Displacement accumulated at the surface for F3 is 2 cm. F7 propagate down from the surface to form a listric geometry, where the dip angle changes from 40° near the surface to 16° for 13 cm until the fault plane flattens out in marker stripe D to an angle of ca. 3° for 7 cm. The lower tip of F7 is intersected by an upwards-propagating F2. F2 reaches the middle of marker stripe C, where it flattens and dips towards the left at an angle of 1.5° for 3.5 cm and intersects with the fault plane of F7. Further down-dip, F2 dips at an angle of 12° for 21 cm to marker stripe E, where the dip angle steepens to ca. 40° for 3 cm. The segments of F2 and F7 links together to form horse I with very little internal deformation except some compression towards the right. F4 has propagated down to a length of 3 cm and has the same dip angle near the surface of 40° as F7. F5 is in the footwall of F3 and has a higher dip angle of 52° and a length of 2 cm. F6 represent the orientation of many small splay faults forming in the wedge between F3 and F7. These minor faults are difficult to constrain as the most active slip-surfaces are shifting trajectories and the marker stripes are unclear.

β 1.32-1.56 (Fig. 13E): The floor fault of horse I, which is the old lower part of F7, is left inactive. The roof fault is activated in the master fault plane of F2, which now has a length of 41 cm and an accumulated displacement of the surface of 5 cm. F2 forms a ramp-flat-ramp geometry. F3 has an average dip of ca. 27° and has a length of 24 cm. Displacement accumulated is 2.5 cm. The footwall of F7 moves down and over the flat roof fault of horse I, where three normal faults form riders in marker layer A. F8 dips shallowly of 13° towards the left with a length of 11 cm. F8 cuts shallowly through marker stripe A, on which the hanging wall is moved left relative to the footwall. The total movement direction is to the right for the whole model. F5 intersects with F3 to form rider I. F8 and F3 defines a horst, which is transported towards the right along F2.

β 1.56-1.80 (Fig. 13F): Faults F2 and F8 are dipping towards each other to form a graben. The graben is heavily faulted with generally right-dipping fault planes. Two antithetic through-cutting fault planes, F9 and F10 form. F9 cuts the lowermost parts of fault F2 and F3 to form a graben with F3. Three right-dipping normal faults form in the rightmost part of the graben, along the upper fault plane of F9. F9 has a dip angle of 30° for 7.5 cm down to marker stripe C, where the dip changes to ca. 46°. F10 has a curved geometry, with a dip angle of ca. 40°

and a length of ca. 12 cm. Between F9 and F10, a small graben of originally marker stripe A has been displaced. The section is a series of grabens and horsts.

β 1.80-1.94 (Fig. 13G): The most active part before reaching the full extension is in the rightmost section. F9 and F10 from stage F are cut again by right-dipping through-cutting fault planes F11 and F12.

Summary of model E2

The accumulated displacement on the surface for the two largest fault planes was 7 cm and 5 cm for F2 and F3, respectively. The accumulated heave for the largest fault planes is 22.5 cm, which equals to 70% of the total extension of 66 cm. The maximum fault zone width is estimated to be ca. 3 cm wide measured perpendicular to F2. The maximum fault core width is 4 mm. The width is difficult to constrain for all the faults given the nature of the marker layers.

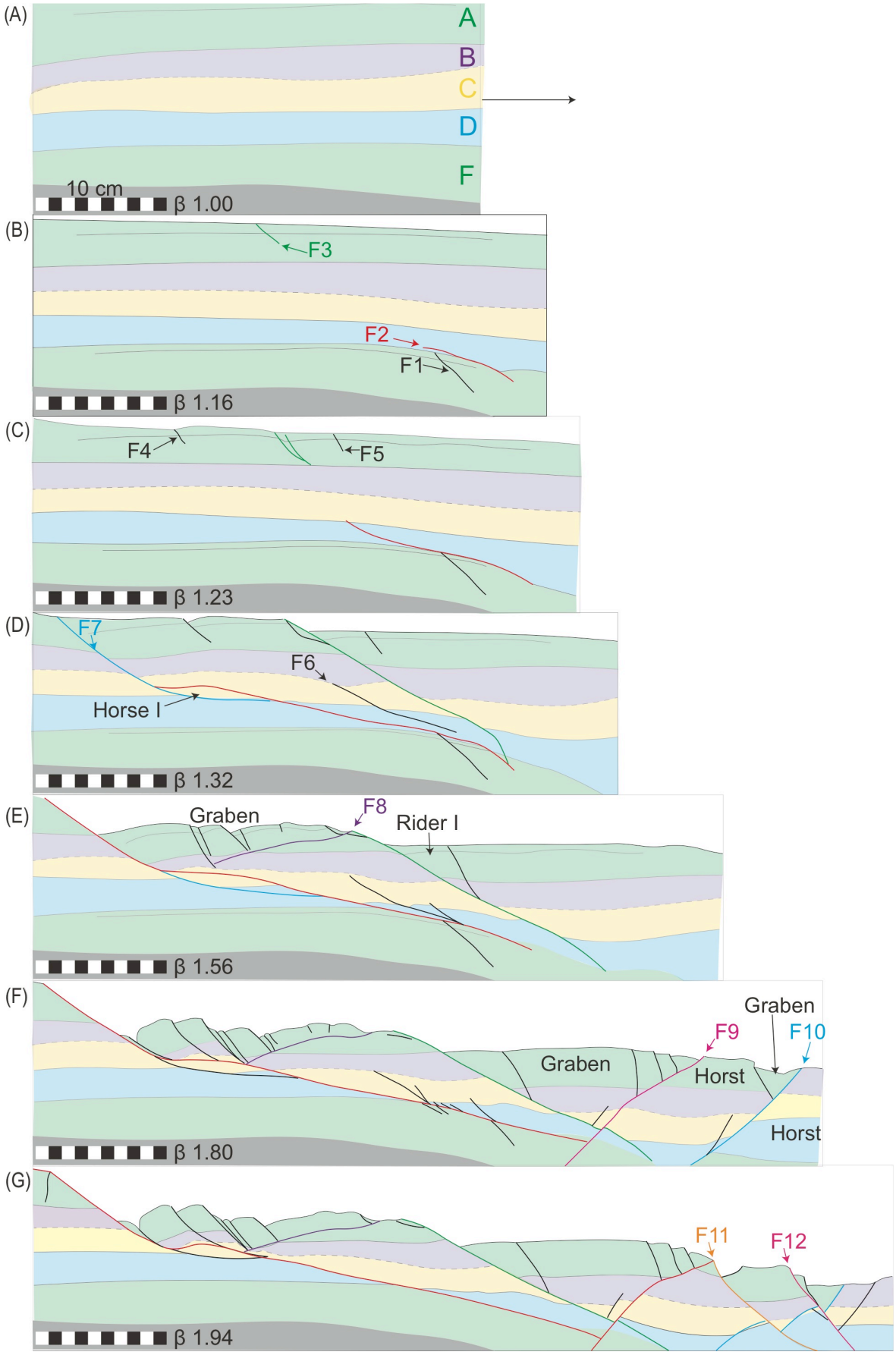

Fig. 13: Structural evolution of model E2 seen in profile plane A.

5.1.3 Group 2: Experiment E3

Laboratory reference	50-14		
Experiment box	Narrow model		
Marker stripes	Blue acrylic paint with water		
Basal layer	Low-angle planar ramp of 30°, where the maximum thickness is 8 cm against the fixed vertical wall and decreases towards the moveable vertical wall to a thickness of 1 cm.		
Plaster to water ratio	1.66	ε	18 cm
Initial length	30 cm	$\dot{\epsilon}$	2.4 mm s^{-1}
Final length	48 cm	β	1.60

Comments: Plaster cover column is 20 cm high. The fixed vertical wall was gently tapped using a hammer. Canola oil was applied to the interface between plaster and the basal barite layer and on the fixed vertical wall. The estimated plaster mixture volume is 5.41 L.

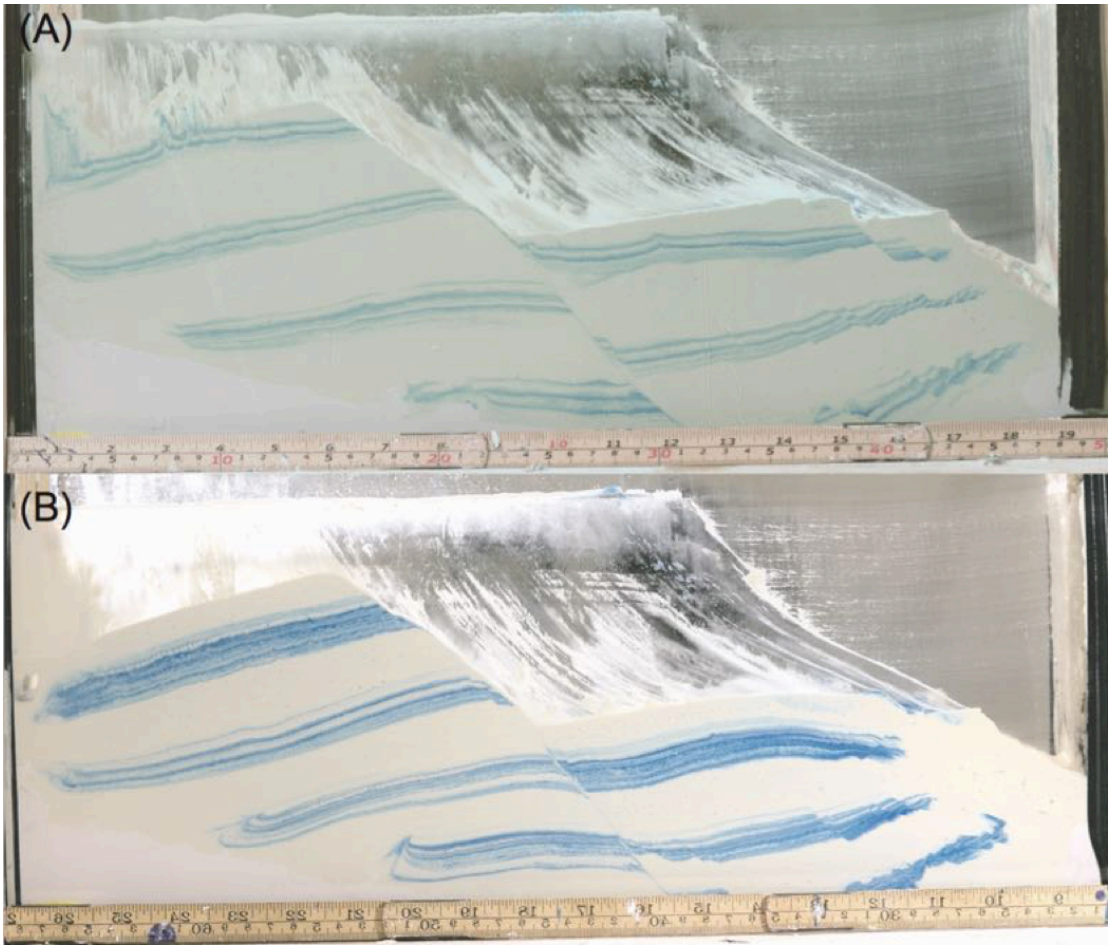

Fig. 14: Photographs of the final stage of model E3 at β 1.60 for side A in (A) and for side B in (B). The scale bars represent cm on the lower row and inches in the upper row.

Description of fault development in E3 Side A

β 1.00 (Fig. 15A): Four marker stripes, A-D are used as reference for displacement.

β 1.00-1.03 (Fig. 15B): As extension starts, the whole plaster cover is moving towards the right. The first visible brittle deformation occurs after just β 1.016. Steep fractures with dip between 70-80° are visible in marker stripe D form first. The fractures have varying dip directions. Seen from right to left is 3 cm of right-dipping fractures and the orientation changes to be left-dipping fractures for the next three cm. The fractures are intersected and overprinted by a dipping fault F1 shortly after their formation. F1 have a 70° dip towards the right and is located in the transition zone between right- and left- dipping fractures. A group of minor left-dipping fractures are apparent in marker stripe C above F1.

β 1.03-1.07 (Fig. 15C): A right-dipping fault (F2) initiate at a low 30° angle and steepen upwards to 70°, the fault propagate upwards to cut marker stripe C. Several minor splay faults intersect with F2 along the base. A normal fault F3 is first visible in marker stripe C, and propagate in both directions, linking together with F2 towards the base and cutting marker stipe B. F3 is relatively planar with a 55° dip angle towards the right between marker stripes B and C, below C the dip angle is a shallower 30-40°. Between F2 and F3, two minor antithetic faults form along the fracture planes of the left-dipping fractures to form a graben enclosed by antithetic fault F3 and F4 and a horst enclosed by F2 and F4 in marker stripe C.

β 1.07-1.13 (Fig. 15D): The master plane F3 is generally very gently curved. F3 accumulate displacement and propagate upwards to cut the surface with an angle of 65°, the dip angles below marker stripe C are not significantly changed from the previous steps. The displacement at the surface is 2 cm. Minor synthetic faults intersect F3 in marker stripe A and B to form a wedge shaped faulted zone in the hanging wall of F3. Right-dipping normal faults are visible in marker stripes A, B and C near the vertical moveable wall.

β 1.13-1.33 (Fig. 15E): The footwall of F3 is starting to rotate along the basal layer. As both the footwall and the hanging wall rotate, the F3 fault plane is gently being rotated to a gentler dip of 52°. The fault plane changes its signature from a curved fault plane to a more planar fault plane. Displacement accumulated along F3 is 6 cm. A layer of smear along F3 is starting to be visible, but it is generally less than 1 mm wide. The plaster cover is slipping off the vertical moveable wall and is separated down to marker stripe B. Faulting in the marker

stripes in close proximity to the vertical wall has increased in numbers and their spacing differs from over 2 cm, to less than 1 cm and around 2 cm again in stripe A, B and C, respectively.

β 1.33-1.60 (Fig. 15F): A layer of smear is growing along F3, where the width varies between 1-5 mm. A lens containing a relatively unaffected sample of marker stripe B has been displaced 10 cm. The footwall of F3 is rotating anti-clockwise and is limited towards the right by the hanging wall. The wedge under F3 in the footwall at the base is compressed, which leads to a large number of minor faults in marker stripe D. A large number of dominantly normal faults have formed in the hanging wall in the rightmost 7 cm of the model. The footwall of F3 rotates further anti-clockwise, leading to a final dip angle of the surface to be ca. 14° towards the left. The rotational component decreases towards the base, where marker stripe D has dominantly been compressed and moved towards the right, and has not been rotated significantly.

Description of fault development in E3 Side B

β 1.00 (Fig. 16A): The photos are rotated -1 degree to level the model.

β 1.00-1.03 (Fig. 16B): The whole plaster medium sinks down and towards the given space. The first structures to form are a large number of near vertical fractures, most of which is found in the plaster cover to the right of the basal ramp. The fractures are first apparent in marker stripes D and C and shortly after in B and A. Their orientation varies, however the large majority is dipping towards the left. The first minor normal faults form in the rightmost 5 cm of the model along the base, with a 50° angle to the right. After 1 cm extension a fault plane F1 is already apparent through marker stripes D, C, B in that order. The fault plane is wavy and has a steep dip of 60-65°. Four left-dipping normal faults form in marker stripe C, of which F2 is marked in the figure as it forms a small horst with F1.

β 1.03-1.07 (Fig. 16C): A normal fault F3 propagates down from the surface and cuts marker stripe B. In the area between the tips of F1 and F3 in stripe C, a second array of left-dipping normal faults forms. They are rotated clockwise from 50° to a gentler dip angle of 30° during ca. 1 cm extension. The rotational component is very small in marker stripe C, when regarding the first array of left-dipping faults (F2).

β 1.07-1.13 (Fig. 16D): At β 1.10, F3 has propagated downwards sub parallel to F1 and is undercutting the left-dipping faults in stripe C. These are now limited towards the base by a curved F3 plane dipping right, cutting the horst at the base and intersecting with F1 in the lowermost part of the fault plane. At the same time, the left-dipping faults in stripe B are overprinted by synthetic right-dipping normal faults, still in the zone between F3 and F1. F1 propagate upwards through this zone and the segment links up with F3 to form a roof fault to an extensional duplex. Where F3 intersect with F1 towards the base, the newly formed fault plane is wavy. The bump in the footwall of F3 in the lower most part collapses, and is smeared along the fault plane. F3 is at β 1.10 the most active fault plane. F1 is relatively inactive. The hanging wall of F3 is relatively passively transported downwards, while minor asperities along the fault plane are smeared out. The fault plane of F3 rotates anti-clockwise to a gentler dip.

β 1.13-1.33 (Fig. 16E): The anti-clockwise rotation of the footwall of F3 increases, which rotates the fault plane to a curved steepening downwards geometry. The exposed fault plane of F3 above the surface has a 48° dip and is relatively planar compared to a gently curved section with a 51° dip under the hanging wall surface level. Displacement accumulated along F3 is ca. 8 cm. Several normal right- and left-dipping faults form in the rightmost part of the model. The plaster cover is sliding off the vertical moveable wall and the anti-clockwise rotation increases in this section.

β 1.33-1.60 (Fig. 16F): The F3 fault plane section above the surface of the hanging wall has a dip angle of 35°, while the section under the surface has a dip angle of 55°. The surface of the footwall dips with a dip angle of 15° towards the left while the surface of the hanging wall has a very gentle dome shape and is dipping very gently towards the left with a maximum 7°.

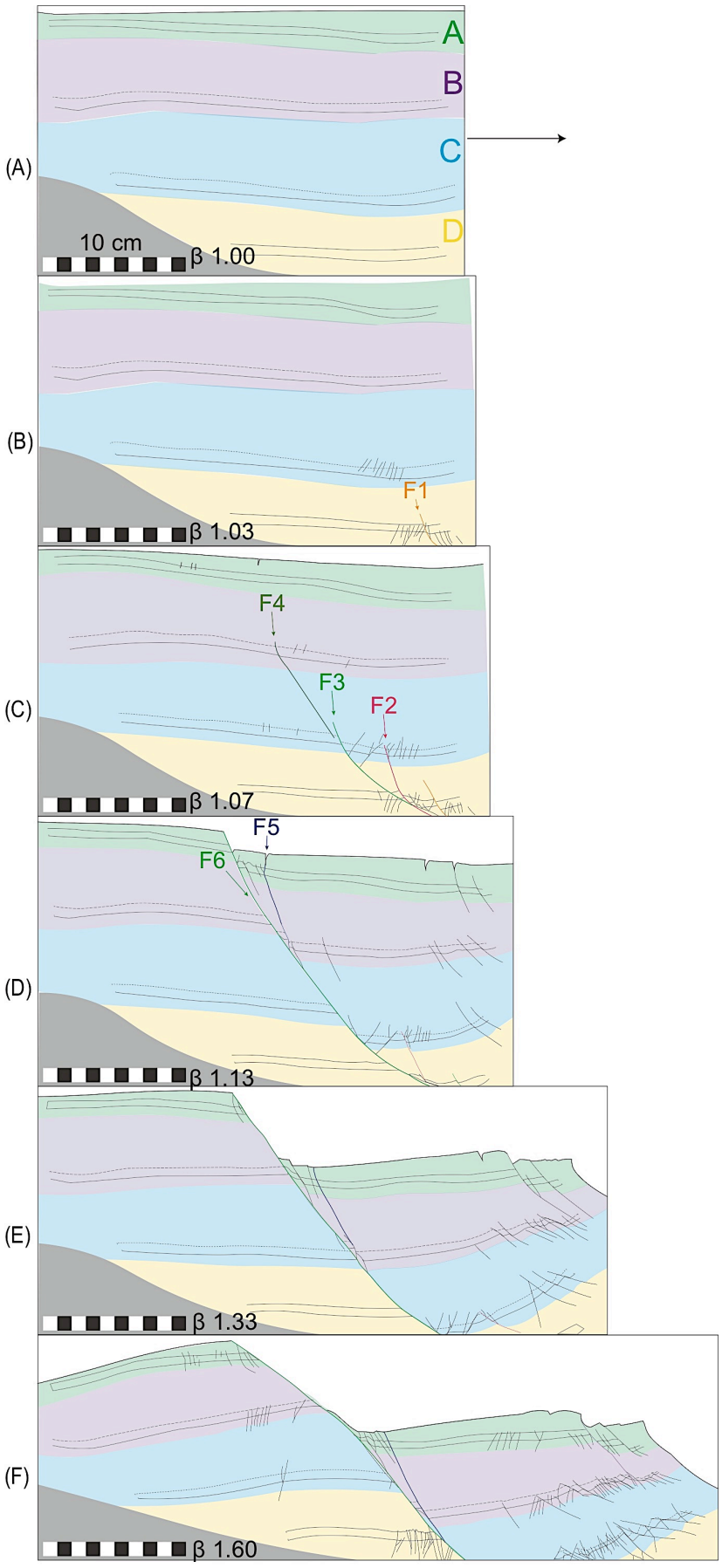

Fig. 15: Structural evolution of model E3 seen in profile plane A.

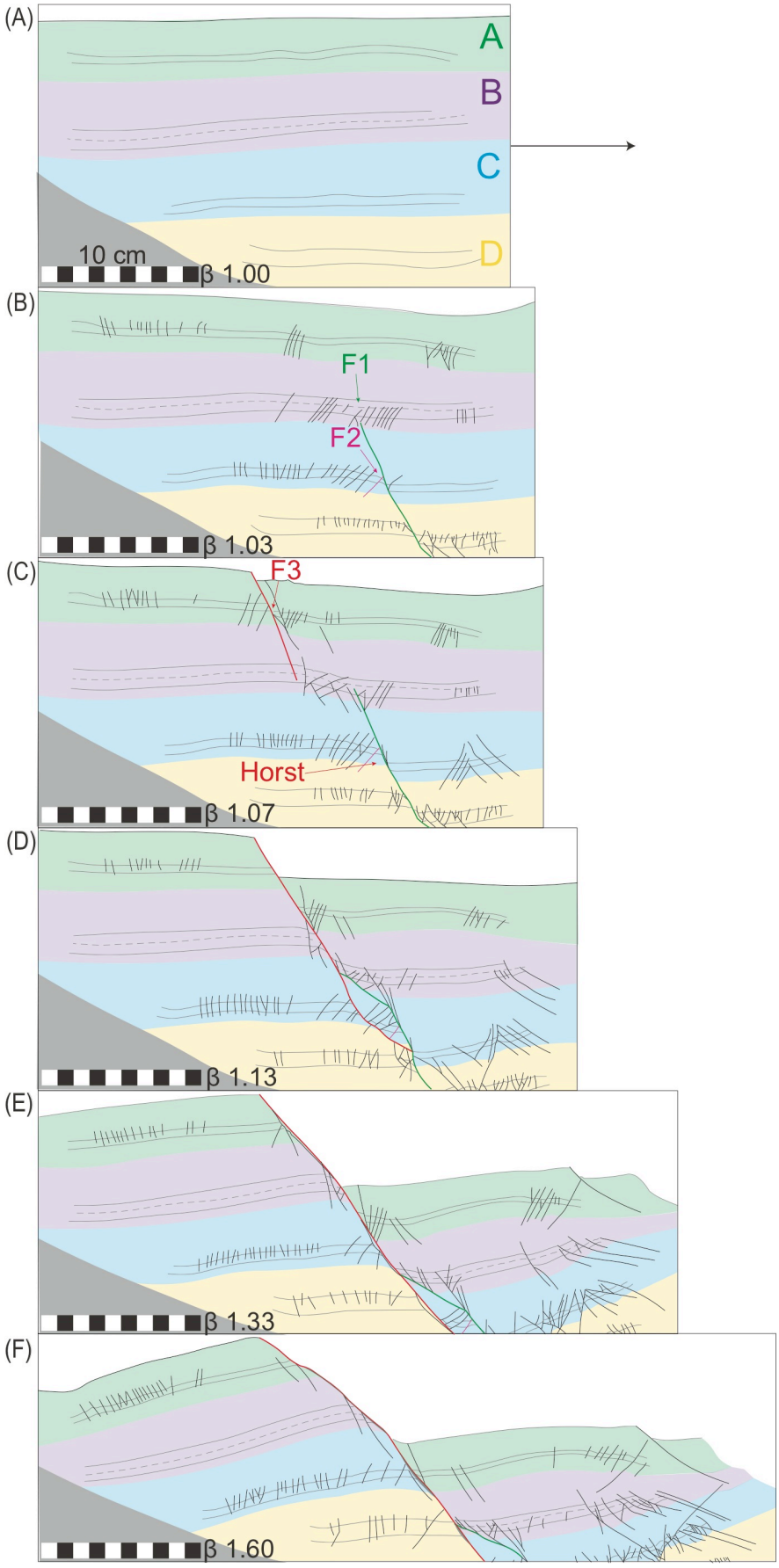

Fig. 16: Structural evolution of model E3 seen in profile plane B

Summary of E3 side A and B

One master fault forms in this experiment, which has a slightly different geometry between the sides. The formation of a through-cutting master fault varies between the two sides. In model E3 side B, many small fractures formed with varying dip directions. A through-cutting master fault formed by segment linkage. The first fault plane (segment 1) formed at the base and propagated upwards with a planar geometry within the first 1 cm of extension. A fault plane initiated at the surface (segment 2) and propagated downward sub-parallel to the first fault plane. A series of left-dipping faults formed in the 4 cm wide zone between the tips of the two segments, which were rotated and subsequently cut through by right dipping fault. A through-cutting fault plane formed as the tips of the two segments overlapped and formed a lens.

In model E3 side A the formation of a through-cutting fault plane is a relatively clean upward propagation. The marker layers are cut in sequence from base to surface to form a generally planar fault plane with a slight decrease in dip angle towards the base. A through-cutting fault plane on side A forms at a slightly later stage relative to side B. Few minor structures form on side A relative to side B. A few splay faults are visible to the master fault and a few antithetic fault planes form where the slope of the master fault plane decreases towards the base.

The quantity of visible smaller structures is larger for side B than side A, The formation of a through-cutting master fault plane is more complex on side B and also precedes the formation in side A. Side A show a relatively smooth and gently curved fault plane, while side B is slightly more wavy. The deformation expressed on side B is then assumed to be the controlling factor, and may explain why small-scale structures is not as dominant on side A.

The fault plane geometry varied throughout the experiment. The major fault plane was irregular shortly after the formation at β 1.13. A more planar fault plane developed by asperity bifurcation, seen at β 1.33. The fault plane developed a more curved steepening downward geometry as the footwall rotated anti-clockwise. Early formed faults are rotated anti-clockwise and cut again to form a complex pattern within the lower hanging-wall.

The accumulated displacement on the surface was 11 cm and 10,5 cm for side A and B, respectively. The accumulated heave is 8.8 cm and 7.8 cm for side A and B, respectively. The measured heave equals to 49% and 43% of the total horizontal extension of 18 cm. The final fault zone width is ca. 3 cm for both sides. The maximum fault core width is 4-5 mm.

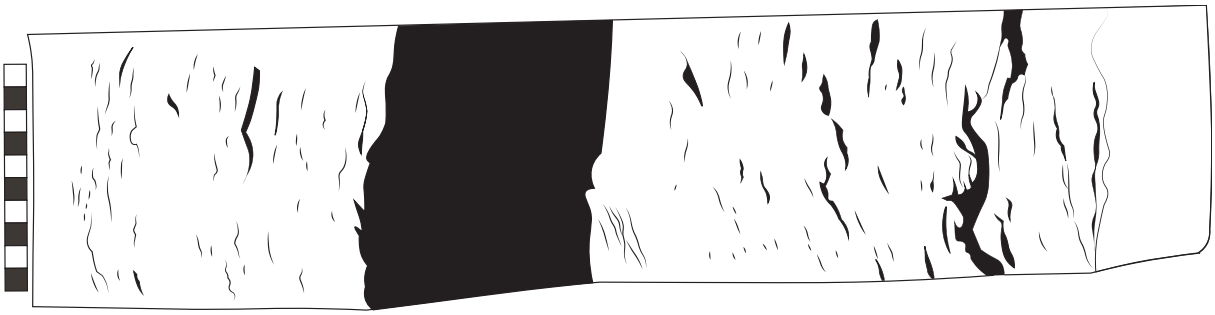

Fig. 17: Illustration of the surface deformation for experiment E3 at β 1.60. Side A is in the upper profile plane, side B is in the lower profile plane. The black lines and fields represent displacement surfaces and discontinuities. The extension direction is towards the right in the figure and the scale bar to the left represents 10 cm.

The end model surface shows many discontinuities of varying size with a general slip-perpendicular strike orientation (Fig. 17). The master fault plane on side B is visible on the surface a few moments before the master fault in side A. Both master fault strands are first apparent on the surface near the edges of the walls and propagates towards the centre of the model. Their tips propagate sub-parallel and form a very short-lived relay ramp with a few minor discontinuities sub-parallel to the two master fault strands. The relay ramp is breached at β ≈1.13, at which the master fault plane geometry consists of two semi-planar traces connected by a ≈30° segment. Displacement is accumulated along the established master fault, with an increasing number of surface fractures near the moveable vertical wall and on the footwall near the master fault plane. The rightmost 5-10 cm is affected by edge effects.

5.1.4 Group 2: Experiment E4

Laboratory reference	51-14		
Experiment box	Narrow model		
Marker stripes	Blue acrylic paint with water		
Basal layer	6 cm thick and horizontal		
Plaster to water ratio	1.66	ε	11.5 cm
Initial length	30 cm	$\dot{\epsilon}$	2.4 mm s^{-1}
Final length	41 cm	β	1.37

Comments: The extension rate is the same as for experiment E3. Plaster cover column is 15 cm high. The estimated plaster mixture volume is 4.95 L.

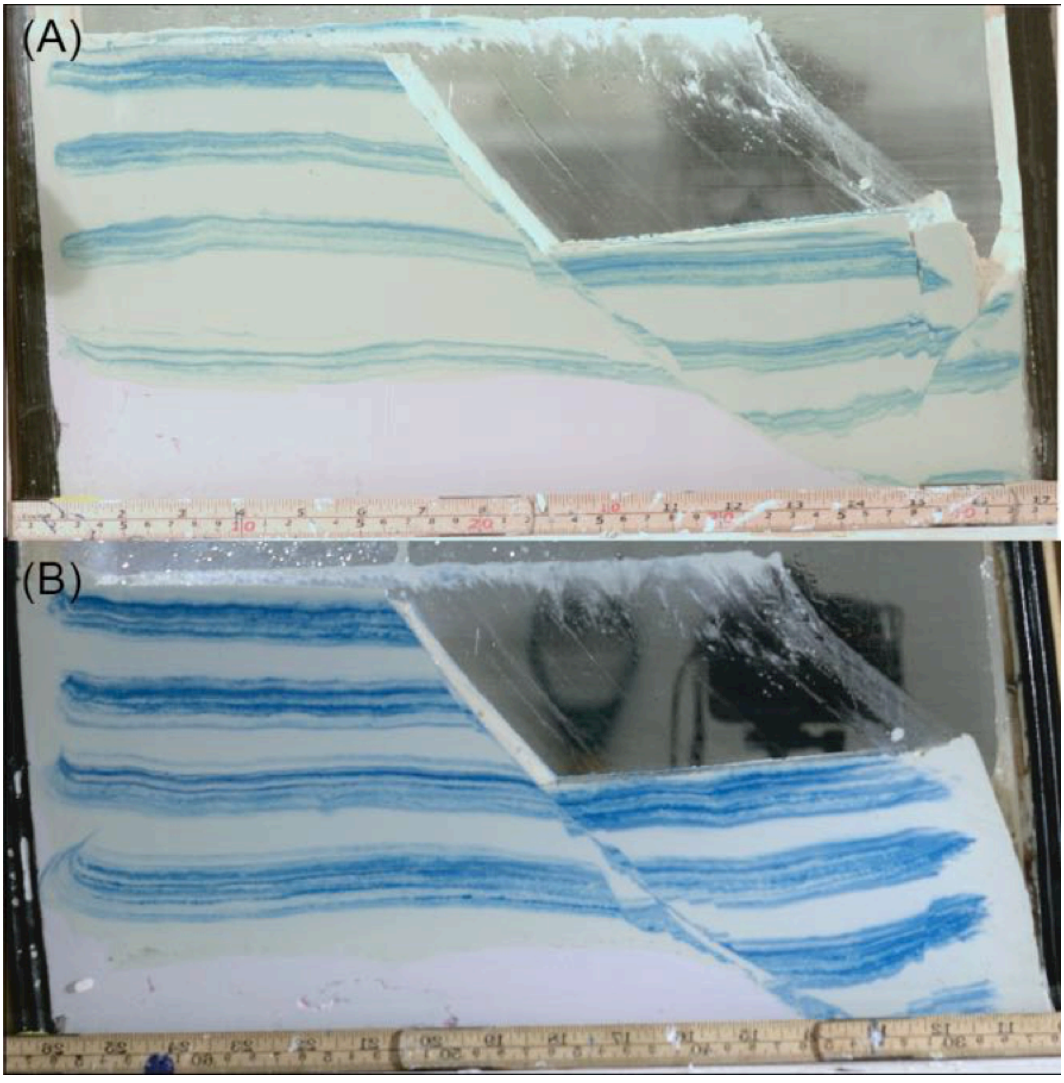

Fig. 18: Photographs of the final stage of model E4 at β 1.37 for side A in (A) and for side B in (B). The scale bars represent cm on the lower row and inches in the upper row.

Description of fault development in E4 side A

β 1.00 (Fig. 19A): Four marker stripes, A-D are used as reference for displacement.

β 1.00-1.03 (Fig. 19B): A gentle folding occurs for the first cm of extension. The folding is heaviest near the moving wall and the dip angle of the marker stripes decreases towards the fixed wall. The first fractures are formed at the base of the plaster medium and are dipping 60° right. The baryte is moving out to form a curved flattening downward geometry, where the dip angle increases towards the base.

β 1.03-1.07 (Fig. 19C): A wide fracture zone of 14 cm is formed above the ramp geometry formed by the basal layer. Several minor normal faults form from the top of the basal layer at the break-off zone of the ramp and propagate upwards for around 3 cm into the base of the plaster. Four larger normal faults (F1-F4) form within a 14 cm wide zone from the base and up to the surface. These four faults are not linked up. F1 cuts the surface and marker stripes A and B, F2 and F3 only cut marker stripes B and C, while F4 cut marker stripe C and D. F1, F2 and F3 are planar, while F4 has a gently curved geometry. F1 has a 58° dip towards the right, F2 and F3 have a dip angle closer to 70° and F4 range from 70° in marker stripe C to 40° near the base.

β 1.07-1.12 (Fig. 19D): The F1 fault seen in B is from now on called F1' as it intersects and cuts F2 and F3, forming a master fault plane that cuts the model from the free surface to the base. The remaining F2 in the hanging wall of F1' propagate upwards to link up with F1' forming a small horse I. F1' and F2 form the floor and roof fault, respectively. F1' propagate downward and cuts the fault plane of F2 and F3, thus incorporating the lower parts of the two fault planes in the F1' footwall. Within horse I, two smaller synthetic normal faults are limited by an antithetic normal fault. F3 and F4 do not have an apparent active propagation upwards, and appears to be passively transported down-dip as the hanging wall moves down. F4 reaches the transition between the plaster cover and the basal baryte layer, but is eventually intersected by F1' as F1' reaches the base and follows the ramp geometry of the basal layer. F1' is at this stage a wavy fault plane with bends/two small ramps.

β 1.12-1.20 (Fig. 19E): The slope of the basal ramp is 9,5 cm and have a 30° dip. This stage is dominated by the reworking of existing faults, and the development of a more planar master fault plane F1'. Asperities along F1' are bifurcated as the fault plane cuts through the bumps and bends on the fault plane, forming a more planar fault. F1' cuts through horse I leaving the

foot fault of horse I to be incorporated into the footwall of FI' and inactive. The top half the horse I, incorporated in the hanging wall, moves downward on the master fault plane, shearing and forming several minor fault. These faults have a near vertical dip towards the right and the marker stripes within the faulted horse have a near horizontal dip. At the right end, the top of the plaster cover has separated from the vertical moveable wall. Minor right-dipping normal faults form before being cut by F5. F5 is a curved steepening downward normal fault plane dipping left.

β 1.20-1.37 (Fig. 19F): A displacement accumulate along F1' and F5, these fault are both normal and they are dipping towards each other. It is not apparent if the two fault planes intersect, therefore the semi-enclosed block is not called a graben. The block is subject to both anti-clockwise rotation and pure shear. Both right- and left-dipping faults form. A fracture forms in the rightmost part of marker stripes A and B in the hanging wall of F5.

Description of fault development in E4 side B

β 1.00 (Fig. 20A): Four marker stripes, A-D are used as reference for displacement.

β 1.00-1.03 (Fig. 20B): The plaster cover is folding gently as extension starts, the dip of marker stripe A has changed from horizontal to a dip of 5° right. Minor normal faults F1 and F2 form at the interface between the baryte basal layer and the plaster cover, near the vertical moveable wall. Both F1 and F2 are curved fault planes with a dip angle range from 70°-40° from top to base. F1 cuts through marker stripes D and C.

β 1.03-1.07 (Fig. 20C): Normal faults forms in a 10 cm wide zone in the rightmost half of the model. F1 and F2 are propagating upwards. The minor unnumbered fault in stage B has been activated together with the upper fault plane of F1, leaving the lowermost part of F1 from stage B less active. Newly formed F3 and F5 are dipping ca. 70° towards the right. F5 only cut marker stripe B, while F3 cuts stripe C and D. F4 cuts the surface and propagate downwards with a ca. 50° dip angle.

β 1.07-1.12 (Fig. 20D): The basal layer forms a ramp dipping 30°. F4 is cutting through the fault planes of F5, F3, F1 and links up with F2 near the base, this through going fault plane is from now on called F6. An antithetic fault forms to F6 near the surface, while a horse forms in marker stripe B. The remnant lowermost parts of the cut faults are incorporated in the footwall and is inactive except for lowermost F3, which forms horse II with F6 that moves

down and rotates anti-clockwise. Also rotating anti-clockwise is an array of normal faults in the footwall of F6, enclosed by lowermost F1 to the left and F6 to the right to form horse III. The cut fault planes incorporated in the hanging wall of F6 is relatively inactive as the hanging wall moves down-dip. The dip angle of F6 is 55° towards the right above marker stripe B and 45° below this the displacement is 2.5 cm.

β 1.12-1.20 (Fig. 20E): Displacement accumulated at this stage is 6 cm along F6, the dip angle is unchanged from step D. Faults F5 and F3 in the hanging wall is propagating upwards, cutting through marker stripe B. F2 in the hanging wall has linked up with F6, forming a small horse IV. A normal antithetic fault F7 forms in the rightmost part of the model to form a graben enclosed by F6 and F7.

β 1.20-1.37 (Fig. 20F): Some asperity bifurcation along the fault plane is the lowermost part of F6 increases the width of the smear zone to 0.3 cm in some areas, while in generally along the fault plane the zone is a very narrow 0.05 cm. The plaster is relatively stiff, and accumulation of displacement is only apparent for F6 and F7. The total amount of displacement along F6 is 11 cm, while F7 show a displacement of 0.5 cm.

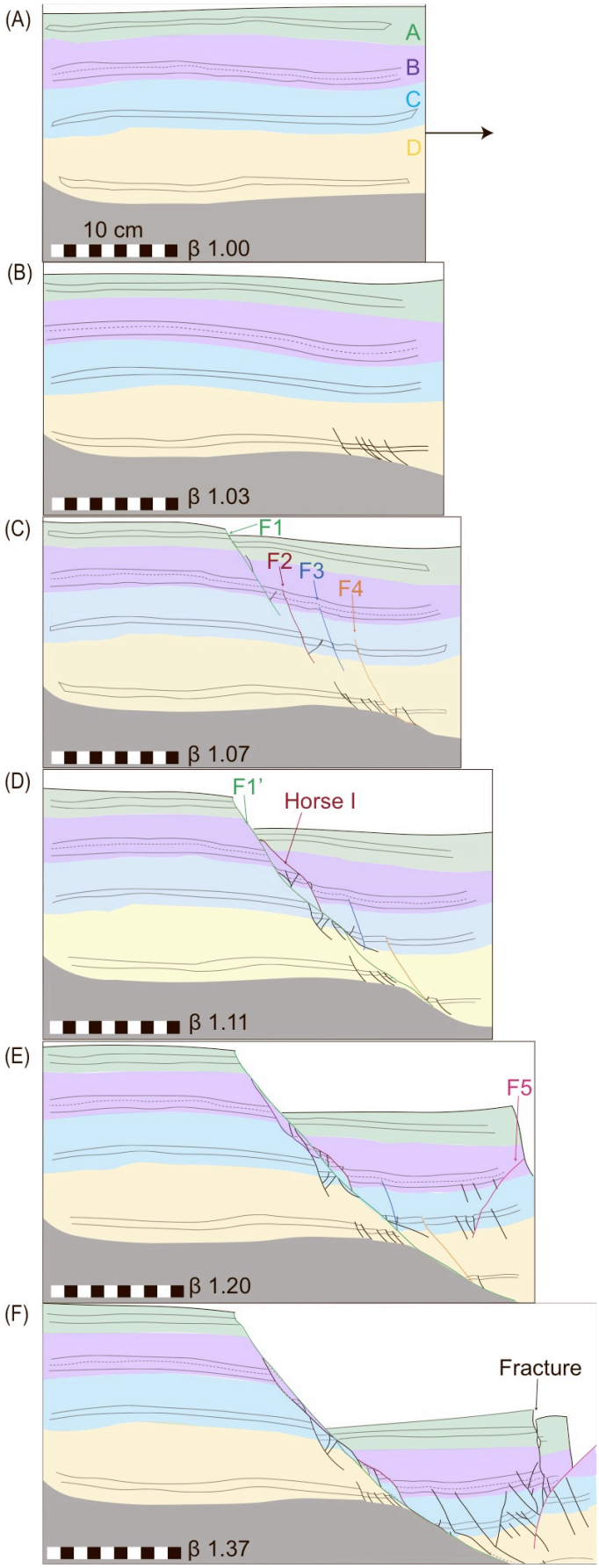

Fig. 19: Structural evolution of model E4, seen in profile plane A.

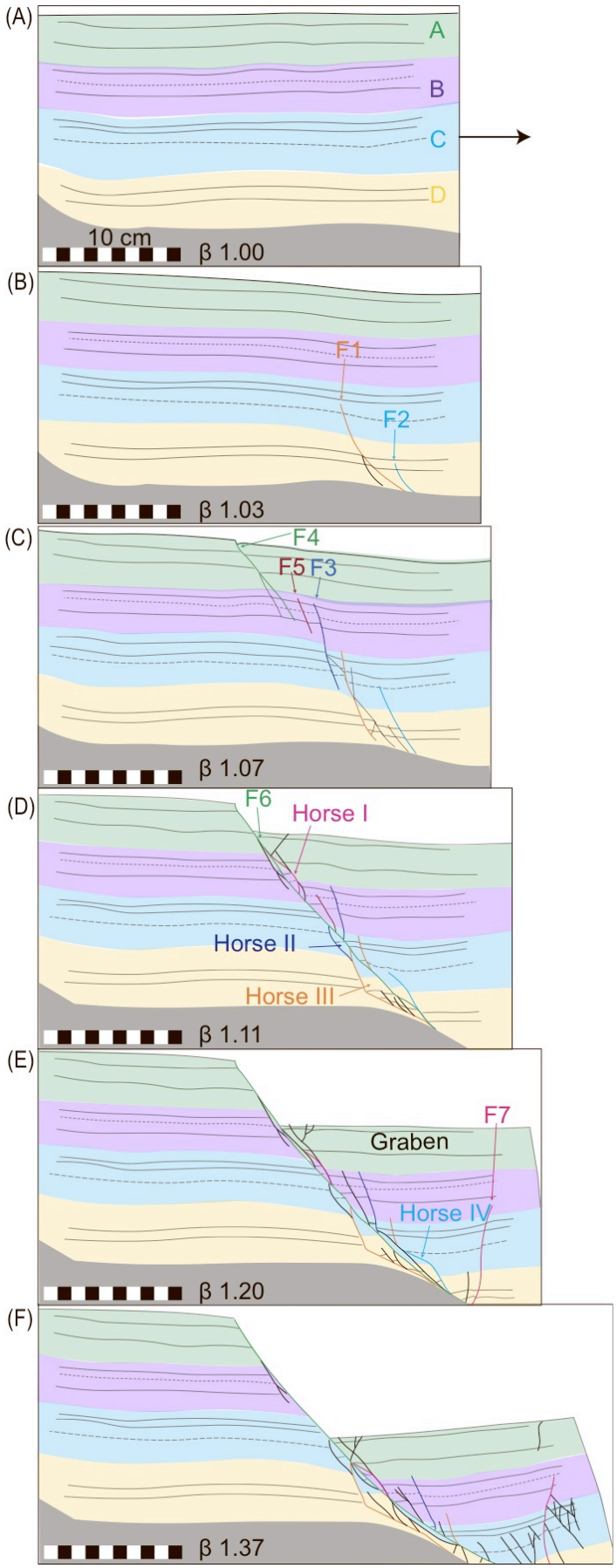

Fig. 20: Structural evolution of model E4, seen in profile plane B.

Summary of E4 side A and B

The mechanisms leading to the formation of a through-cutting master fault plane are similar for side A and B. The first brittle structures form at the interface between the plaster and the basal layer in the lower right corner of the model. Several sub-parallel faults cut sequentially upwards until the surface is breached and a through-cutting fault plane forms. The master fault plane cuts through the first generation of faults, which is left relatively inactive in the footwall and hanging wall. A left-dipping fault forms in the rightmost part of the model and many minor faults form in the lower part of the hanging wall. A fracture forms from the surface and propagate downwards on side A, the block slides down the left-dipping fault plane to increase the amount of smaller faults in the hanging wall.

The fault zone is ca. 4.5 cm wide at maximum, both measured in the horizontal plane and perpendicular to the fault plane. The deformation width decreases towards the surface to an mm-scale. The accumulated displacement on the surface was 11 cm for both side A and B. The accumulated heave was 10.3 cm and 9.3 cm for side A and B, respectively. The measured heave of larger faults equals to ca. 80% and 89% for side A and B, respectively, of the total extension of 11.5 cm. The maximum fault core width is 6-7 mm.

The surface shows very few discontinuities or displacement structures (Fig. 21). The master fault plane strands appears to breach the surface close to simultaneously. The surface breaches near wall A roughly a second before it breaches near wall B. The two tips propagate towards each other in a gently curved manner and connect to form an uneven fault trace at β 1.05 and a lens of surface material enclosed by two normal faults of which the one to the right is the visible, connected fault plane. The rightmost 5-10 cm is affected by edge effects.

Fig. 21: Illustration of the surface deformation for experiment E4 at β 1.37. Side A is in the lower profile plane, side B is in the upper profile plane. The black lines and fields represent displacement surfaces and discontinuities. The scale bar to the left represents 10 cm.

5.1.5 Group 2: Experiment E5

Laboratory reference	52-14		
Experiment box	Narrow model		
Marker stripes	Blue acrylic paint with water		
Basal layer	6 cm thick, stiff and horizontal		
Plaster to water ratio	1.66	ε	22 cm
Initial length	30 cm	$\dot{\epsilon}$	11.9 mm s^{-1}
Final length	52 cm	β	1.73

Comments: Plaster cover column is 15 cm high. The initial conditions are the same as experiment E4, however the extension rate is relatively higher for this experiment with a rate of 11.9 mm s^{-1} compared to 2.4 mm s^{-1} for E4. The estimated plaster cover volume is 4.95 L. A hammer is used to gently tap the underside of the experiment table.

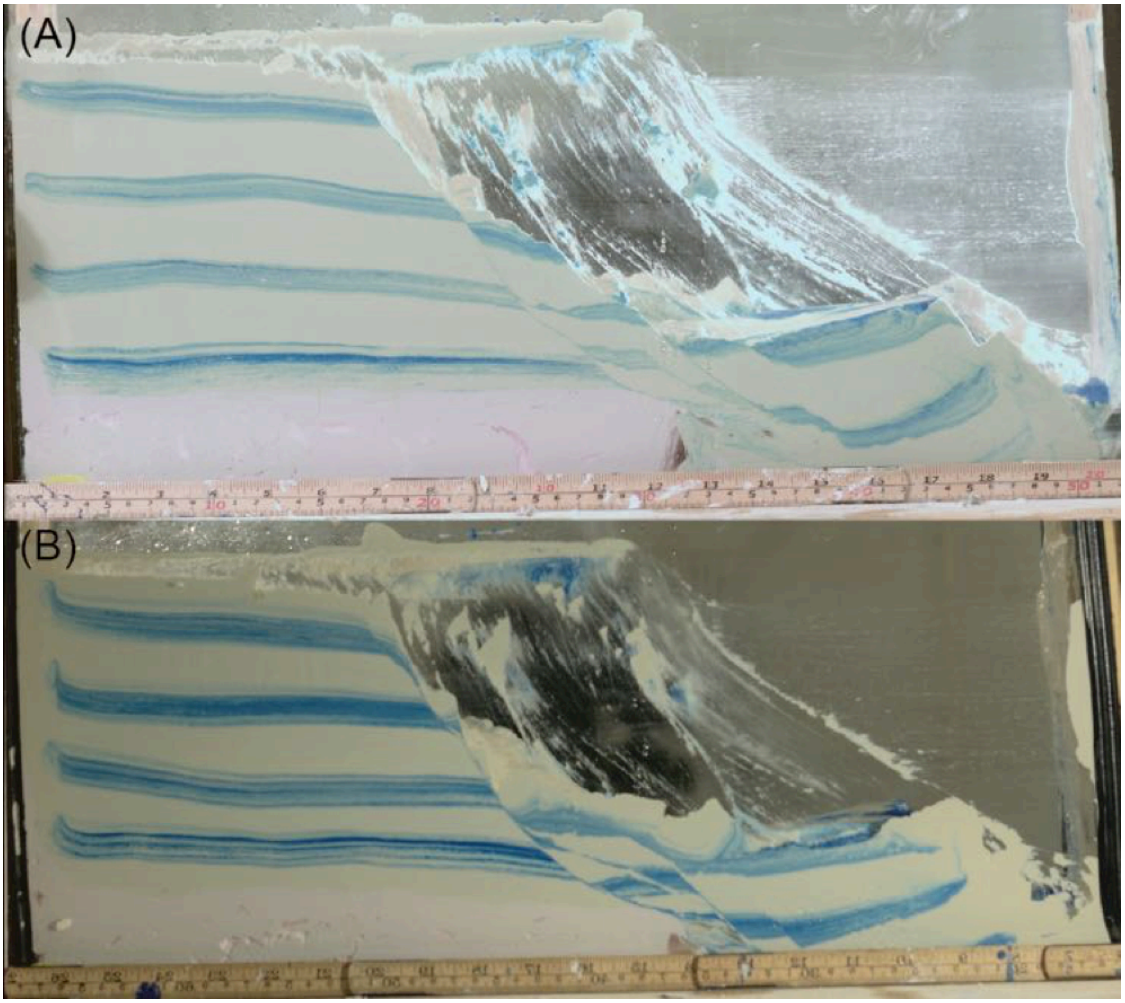

Fig. 22: Photographs of the final stage of model E5 at β 1.73 for side A in (A) and for side B in (B). The scale bars represent cm on the lower row and inches in the upper row.

Description of fault development in E5 side A

β 1.00 (Fig. 23A): Five marker stripes, A-F are used as reference for displacement. The photos are rotated anti-clockwise 1° to level the model.

β 1.00-1.11 (Fig. 23B): The stiff basal baryte layer forms a near vertical drop-off zone as the experiment starts. The plaster cover flows towards the given space and spills over the baryte edge. Marker stripe C has changed dip angle from horizontal to ca. 14° right. Normal faults with a dip angle of 45-50° right form at the interface between the rigid baryte layer and the plaster in close proximity to the drop-off zone. F1 forms 2 cm from the baryte edge at a 45 ° angle and cuts marker stripes F and E. F2 forms at the very edge of the baryte towards the right and propagates upwards relatively fast compared to F1. F2 cuts in reverse sequence the marker stripes B and C at a 60° dip angle and D, E and with a dip angle of 45°, sub parallel to F1. Many minor faults are apparent in marker stripes D, E and F surrounding F1 and F2 in the rightmost 10 cm of the model.

β 1.11-1.18 (Fig. 23C): F1 and F2 propagate upwards sub parallel with a 50° angle. Splay faults with a dip of ca. 65° form from F1 and F2 in their hanging walls. F3 is one of many splay faults to nucleate from F2, however it stands out as it accumulates relatively more displacement of 0.5 cm in marker stripe C and it cuts the surface. In the footwall of F1 there is relatively little deformation, except for a few normal faults that lie sub parallel in close proximity to F1. In marker stripe E, two minor normal faults intersect with F1. The deformation is concentrated in the rightmost 20 cm of the model.

β 1.18-1.26 (Fig. 23D): The F1 fault plane changes its course and cut through the splay faults and marker stripe D to follow the fault plane of F2. The newly formed master fault plane is called F4. The uppermost part of F2 in marker stripes A, B, C and ca. 1 cm of top D is now a splay fault to F4. Displacement accumulated along F4 at surface level is 2 cm. The F4 geometry is a 55° ramp from marker stripe A-D, a flatter portion of 35° from middle stripe D to middle E, and a steeper portion of 60° down to base. F5 is also a splay fault, which runs parallel with F3, and is located furthest to the right. The lowermost fault planes of F1, F2 and other right-dipping normal faults are enclosed in the footwall of F4 to form three horses with a shared roof fault in F4. Collectively, the horses are called an extensional duplex. The array of splay faults can be called riders as their tips are free towards the surface, and collectively they are called a listric fan.

β 1.26-1.40 (Fig. 23E): A displacement accumulates to ca. 4 cm along F4, the fault plane again changes below marker stripe C to follow the path of the floor faults of horses I and II. This new most active fault plane is wavy, and the hanging wall is flowing in an apparently ductile style down-dip. F2 has accumulated 3.5 cm of displacement, while F5 has accumulated ca. 1.5 cm. Splay faults to the abandoned F4 plane formed in stage D has accumulated ca. 0.5 cm each and has cut the surface.

β 1.40-1.73 (Fig. 23F): The most active fault plane is F2, which have accumulated 7 cm displacement. The second most active fault plane is the wavy F4, which have accumulated ca. 8.5 cm displacement. The marker layer in the footwall of F4 is relatively unchanged, affected only by a modest rotation anti-clockwise and very few deformation structures are apparent.

Description of fault development in E5 side B

β 1.00 (Fig. 24A): Five marker stripes, A-F are used as reference for displacement. The photos used for references are reflected horizontally and rotated clockwise 0.5° to level the model.

β 1.00-1.11 (Fig. 24B): The stiff baryte basal layer is forming a steep drop off zone as the vertical moveable wall is pulled to the right. The first faults form at 3 cm extension, β 1.10, near the edge of the model. F1 and F2 propagate upwards to reach the lower parts of marker stripe B, where their spacing is 3.5 cm. The fault planes are generally sub-planar with a slight decrease in dip near the base. F1 and F2 dip 60° and 70° towards the right above marker stripe E, respectively. The dip angle decreases to ca. 30° below marker stripe E for both F1 and F2 and the displacement along the faults decrease upwards. F3 only cut through marker stripe D with an angle of ca. 60°. The dip of the plaster surface above the proximal footwall of F2 has changed from horizontal to 10° right. The dip angle of the minor faults and splay faults marked in black range between 60-80°.

β 1.11-1.18 (Fig. 24C): F1 plane propagate upwards to cut the surface, while F2 is relatively inactive. The F1 fault trajectory fans upwards and cuts the surface to form smooth footwall fault plane and a rider in the hanging wall at the surface. The fault plane is generally listric with a gentle bump in marker stripes C and D. Splay faults form in the hanging wall of F1, especially in areas where the dip angle increases or decreases rapidly. The length of F1 is ca. 20 cm and the displacement accumulated at the surface is ca. 1 cm. F3 propagates upwards to

reach lower marker stripe A and downwards to intersect with a play fault to F1. A small normal fault forms outside the basal layer at a 60° angle. The upper part of marker stripe A in the hanging wall of F1 is curling up as the slab moves down.

β 1.18-1.26 (Fig. 24D): Displacement accumulated along F1 is ca. 3.5 cm. F4 forms with a ca. 40° angle and cuts over the area of F1 plane where the slope change is largest, meaning where the slope changes from a steeper 55° to a lower 25° between marker stripes E and F. F4 accommodate displacement at the same time as the original F1 plane, they are both active. The top of marker stripe D has been displaced ca. 1 cm along F4, while relative to the original F1 fault plane the displacement is 3 cm. F4 forms the roof fault of horse I with F1 as floor fault. The dip angle of the surface in the proximal hanging wall of F3 is relatively flatter of ca. 5° right compared to 10° at β 1.11. F1 is undulating at this stage due to formation of riders, small horses and splay faults in the hanging wall, Rider II is the largest of the newly formed riders. Marker stripe A is faulted near horizontally, where the upper part is a coherent slab moving to the left, and the lower part moves towards the right as the hanging wall of F1.

β 1.26-1.40 (Fig. 24E): Displacement accumulated along the master fault F1 is 5 cm, while 2.5 cm displacement is accumulated along the rightmost limiting fault of rider I. The F1 fault plane above the point of intersection with rider I is inactive from this point. An antithetic fault F5 form in the proximal parts of F1 hanging wall. The two normal faults F3 and F5 dips away from each other to form a small horst, while a graben is defined between F1 and F5. The structures are transported downwards along F4, while horse I rotates anti-clockwise and slides down F1.

β 1.40-1.73 (Fig. 24F): The layering within horses I and II rotates anti-clockwise and many small splay fault form within. In horse I, a few antithetic fault forms where the curvature is largest near the base. The total amount of displacement accumulated along F1 and rider I combined is 8 cm. A few synthetic fault forms in the hanging wall of F2. A vertical section through the fault zone shows a column of stacked horses and riders.

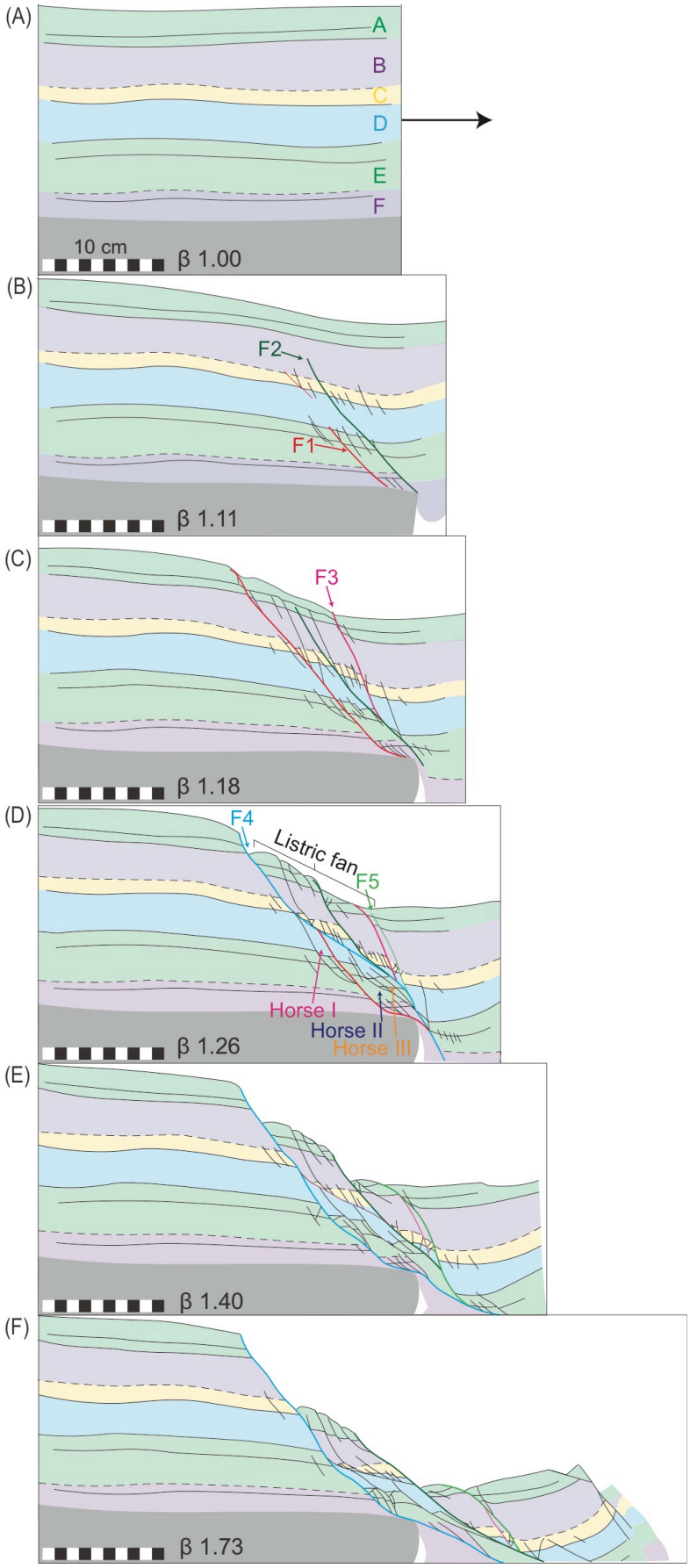

Fig. 23: Structural evolution of model E5 seen in profile plane A.

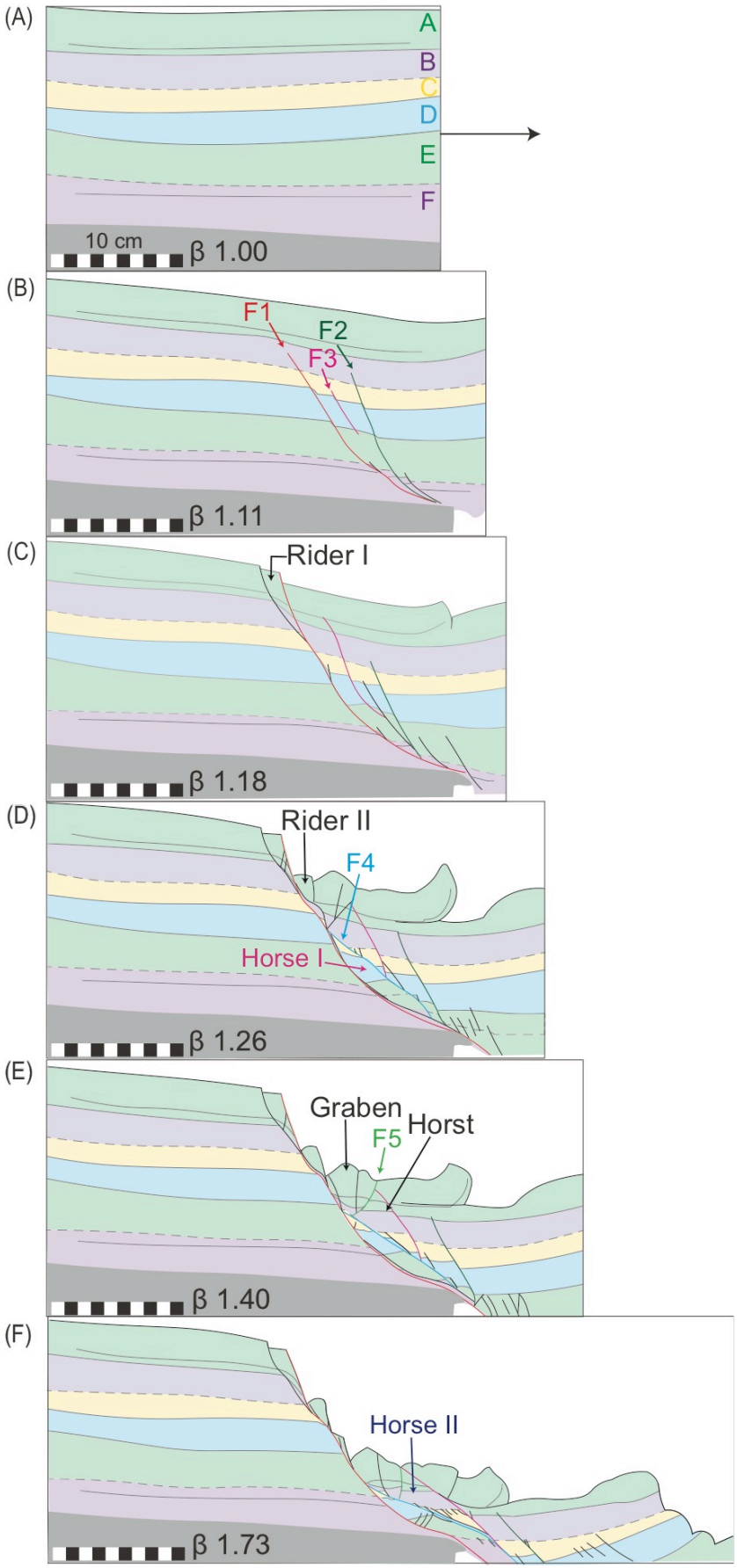

Fig. 24: Structural evolution of model E5 seen in profile plane B.

Summary of E5 side A and B

Only a few minor antithetic faults form close to the major fault plane in the hanging wall, in horse I on both sides A and B. The final fault zone is the widest in this model, compared to E1-E4, due to a shifting fault plane trajectory. This model can be divided in to three blocks. The first block is the relatively unstrained footwall of F4 to the far left. The second block is a heavily faulted and displaced block, enclosed by F1 and F2, seen in Fig. 23F. The third block to the far right is a faulted and rotated hanging wall block of F2. Block two accommodates a large amount of displacement during the experiment as the most active fault plane changes its trajectory.

A measured accumulation of 13.8 cm and 10.8 cm heave for side A and B, respectively, equals to 63% and 49% of the total horizontal extension of 22 cm. The displacement accumulated on the surface is 8 cm and 8,5 cm for side A and B, respectively. Most of the displacement has been accommodated in the collective fault zone, which consists of several minor faults and lenses of plaster. The width is 6 cm, measured horizontal, and the most of the fault zone is found in the hanging wall of F4. The maximum fault core width is 3-4 mm.

Discontinuities on the model surface are marked black in Fig. 25. Their general strike orientations form an acute angle with the glass wall towards the direction of movement, which is to the right. They run semi-parallel to the vertical short walls. Tension cracks. The fractures appear to form an acute angle with the glass walls towards the right for both profile plane A and B close to the fixed glass walls. The rightmost 5-10 cm is affected by edge effects.

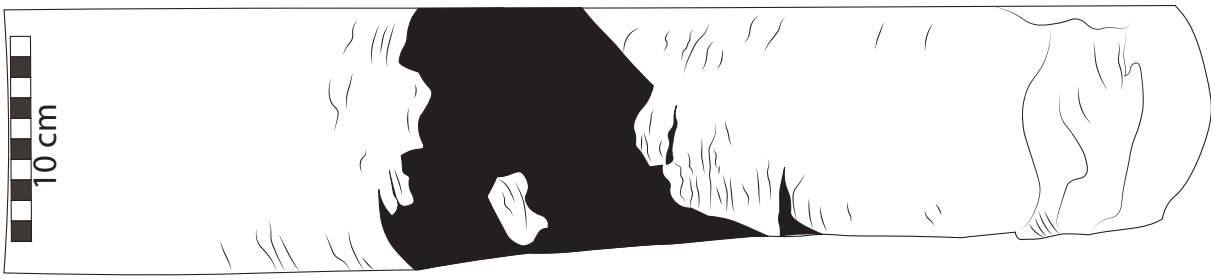

Fig. 25: Illustration of the surface deformation for experiment E5 at β 1.73. Side A is in the upper profile plane, side B is in the lower profile plane. The black lines and fields represent displacement surfaces and discontinuities. The scale bar to the left represents 10 cm.

5.2 Fault development and further results

The data collected from the experiments are presented in this section. The relations of the geometric and structural development of the basal layer and the plaster cover with increasing strain such as fault initiation, displacement-length and the development of fault geometry is presented as plots and figures.

5.2.1 The development of basal layer geometry

During an experiment, the basal layer may shift and alter the original geometry. The originally horizontal basal geometry developed into a flat-ramp-flat geometry within for E1 and E4 within 0-23% extension. The dip angles were 20° for E1 and 30° for E4. The near horizontal basal layer only change shape to a small ramp in the rightmost 2 cm for E2. The initial dip angle for the ramp geometry for E3 was 29°, while the final dip angle was 16°. The originally horizontal base layer in E5 was relatively viscous compared to E1-E4, and formed a steep drop-off zone rather than a ramp.

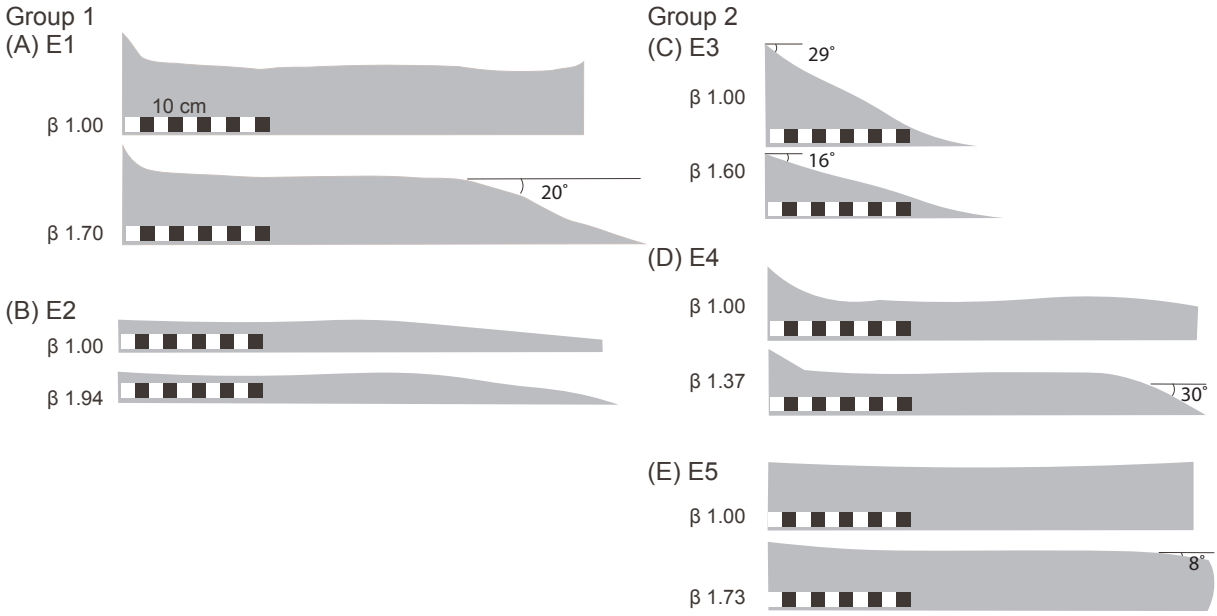

Fig. 26: The amount of shape change of the basal layers varies between experiments. (A) The horizontal basal layer in E1 slides out to form a ramp of 20°. (B) The near horizontal basal layer only change shape to a small ramp in the rightmost 2 cm. (C) The planar ramp of 29° in E3 rotates and form a shallower 16° ramp. (D) The horizontal basal layer in E4 flattens to form a ramp of 30°. (E) The horizontal basal layer in E5 is relatively stiffer and forms a steep drop-off zone at its rightmost end.

5.2.2 Displacement field and particle path

Visualisation of the displacement field in models E1-E5 is provided in this section. Each displacement vector represents the translation of a traced point. The vectors do not represent the exact particle path, but the initial and final position of certain points in the model. The vectors therefore represent the shortest path possible from the initial stage to the final stage of deformation and exclude any rotational component for the individual points. Faults are discontinuities with displacement, which results in discontinuities in displacement rates and patterns. Particle paths are what one could imagine when observing structures in nature, going from a deformed medium and putting the pieces back together into a near complete and unstrained section. In order to balance a section correctly, the level of details in reference data is crucial. The advantage of plaster modelling is that the structural evolution can be recorded and the stepwise particle paths illustrated in section 5.2.3 can be used for further reference. The models are divided into colour-coded blocks to enclose traced particles with relatively parallel vectors and similar lengths. The displacement field and particle paths can therefore be used as reference lines for balancing a deformed section to the initial state.

Displacement field for model E1

Model E1 is divided into seven colour-coded blocks that portray similar displacement patterns and coherent blocks enclosed by faults.

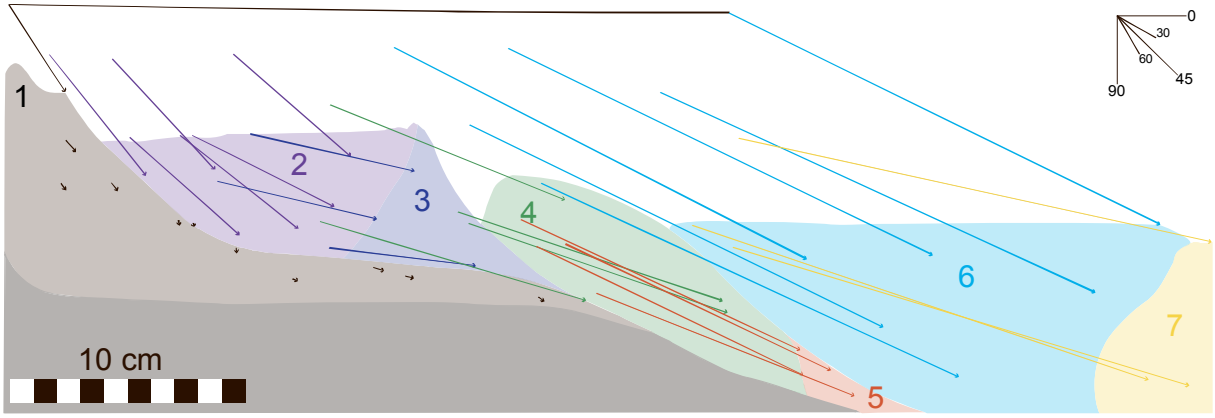

Fig. 27: Visualisation of the displacement field for experiment E1 at β 1.00-1.70. The model is divided into seven blocks representing similar displacement patterns. The top black line represents the original surface level and start length of the model. Vector arrows represent the shortest displacement path and angle of translation, pointing from the initial stage to the final stage of deformation. The arrows are colour-coded corresponding to the end-position of the traced particle.

Block 1 to the far left in Fig. 27 has the shortest average displacement vectors of 0,4 cm and has mostly been moved slightly obliquely towards the right. There are three trends, which are 53°, 82° and 24° angle when looking from left to right in Fig. 27. Displacement vectors of block 2 have an average trend of 6,5 cm length and 41° right, with the highest value of 52° in the left margin and 27° towards the right margin. Block 3 represents the horst structure. The general trend of the displacement vectors is close to a 7 cm length with an angle of 13° dipping right, with a shallower dip of 7° near the base. The average vector trend in block 4 is a length of 11.5 cm and an angle of 19° dipping right. Block 5 represents the horse structure and the vector average is a length of 13 cm with an average angle of 25° dipping right. The vectors are on average 20 cm long with dip angle 26° and 20,5 cm long with dip angle 16° for block 6 and 7, respectively.

Displacement field for model E2

Model E2 is divided onto seven colour-coded blocks that portray similar displacement patterns.

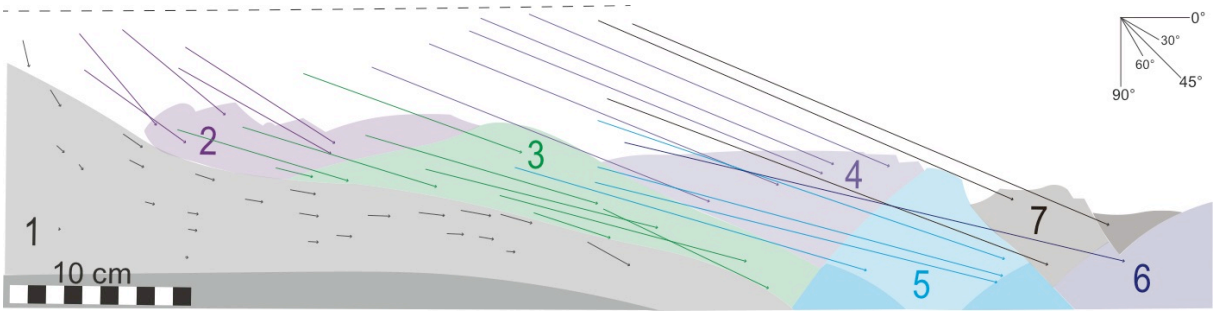

Fig. 28: Visualisation of the displacement field for experiment E2 at β 1.00-1.94. The model is divided into 7 colours representing coherent blocks. The top black dashed line represents the original surface level and start length of the model. Vector arrows represent the shortest displacement path and angle of translation, pointing from the initial position to the final position of the traced particles.

Displacement vectors in block 1 has relatively short displacement vectors with dip angles gradually changing from a steep dip angle of 75° near the original surface and decreasing towards the base to a near horizontal dip angle. Block two has crossing displacement paths, indicating rotation along the left margin. The dip angles vary between 30-50°, while the displacement length varies between 5-7 cm. The general dip angle of displacement vectors in block 3 is 15-20°, while the length increases from ca. 3 cm at the base to ca. 9 cm towards the top. Block 4 has a relatively uniform trend of displacement length 15 cm at an angle of 22°. Block 5 has been displaced an average of 17 cm, at an angle of 15-20°. Block 6 has few traceable points, and has been displaced minimum 21 cm at a relatively low angle of 13°. Block 7 has been displaced an average of 20 cm at an angle of 20°.

Displacement field for model E3

Model E3 is divided into two colour-coded blocks that portray similar displacement patterns.

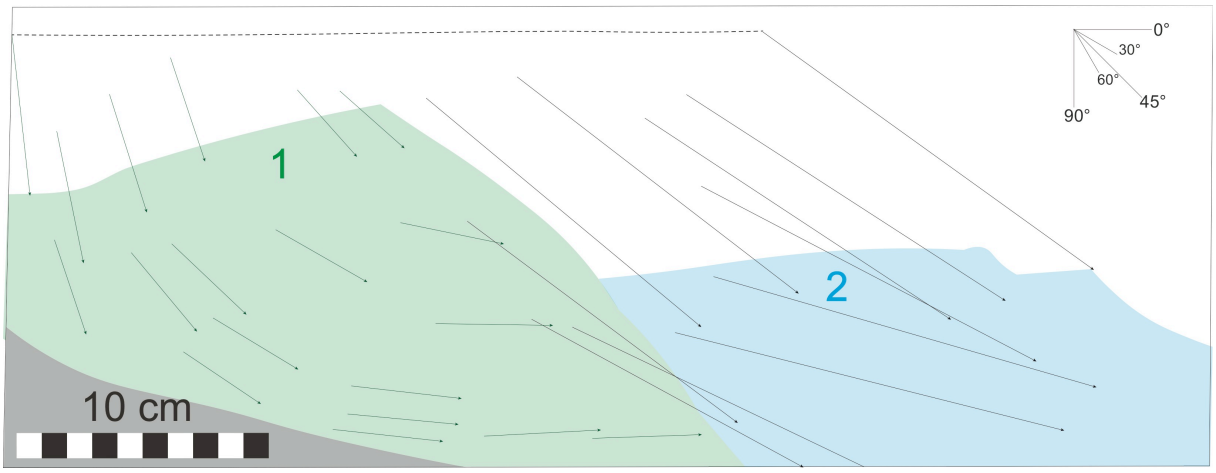

Fig. 29: Visualisation of the displacement field for experiment E3 at β 1.00-1.60. The model is divided into two colours representing coherent blocks. The top black dashed line represents the original surface level and start length of the model. Vector arrows represent the shortest displacement path and angle of translation, pointing from the initial position to the final position of the traced particles.

Displacement field vectors in block 1 have a relatively more variable dip angle than block 2. Traced points near the surface in block 1 have dropped a maximum of ca. 6.5 cm height and show a small horizontal component, giving the displacement vectors a steep dip angle of 70-85°. From surface to base the vectors in block 1 have similar lengths, while the dip angle changes from steep to near horizontal. At the base, close to the boundary between block 1 and block 2, the displacement vectors show an upward trend of -2°. Displacement vectors of traced particles with end-position within block 2 show a more uniform trend. The dip angle is at a maximum of ca. 40° near the surface and the boundary of block 1 and block 2. The dip angle changes from 40° to 35° from left to right in the upper parts of block 2. Particles with a final position near the base in block 2 have a steeper dip near the boundary between block 1 and 2 of 30-35°, and a shallower dip of ca. 15° towards the rightmost end.

Displacement field for model E4

Model E4 is divided into two colour-coded blocks that portray similar displacement patterns.

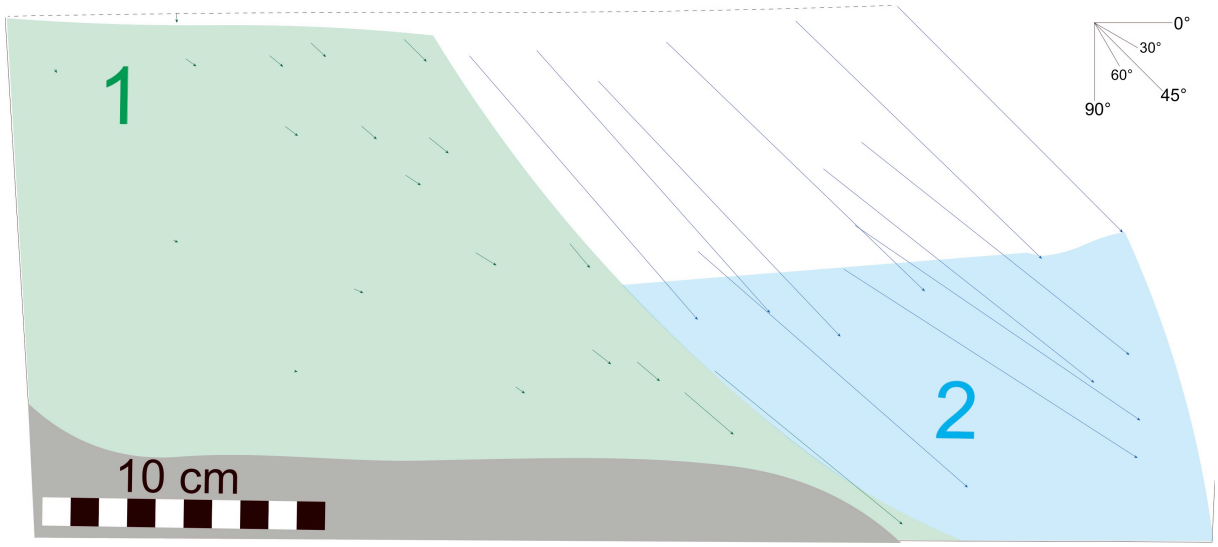

Fig. 30: Visualisation of the displacement field for experiment E4 from β 1.00-1.33. The model is divided into two colours representing coherent blocks. The top black dashed line represents the original surface level and start length of the model. Vector arrows represent the shortest displacement path and angle of translation, pointing from the initial position to the final position of the traced particles.

Displacement vectors in block 1 are generally short, with a length of a few mm furthest to the left and increasing to ca. 1 cm towards the boundary between block 1 and 2. The exception is found near the base at the boundary between block 1 and 2, where one vector has been moved ca. 2.5 cm and another traced particle has been displaced 8.5 cm. The latter originated in block 2 and was at a later stage incorporated in block 1. The displacement vectors of block 2 have two trends. Traced particles near the surface have a dip angle of 50° near the boundary between block 1 and 2, which decreases towards the right to 45°. Displacement vectors with an end-position near the base show an similar trend form left to right, where the dip angles vary from 40°-35°. The displacement vector lengths in block 2 are ca. 12-13 cm.

Displacement field for model E5

Model E5 is divided into three colour-coded blocks that portray similar displacement patterns.

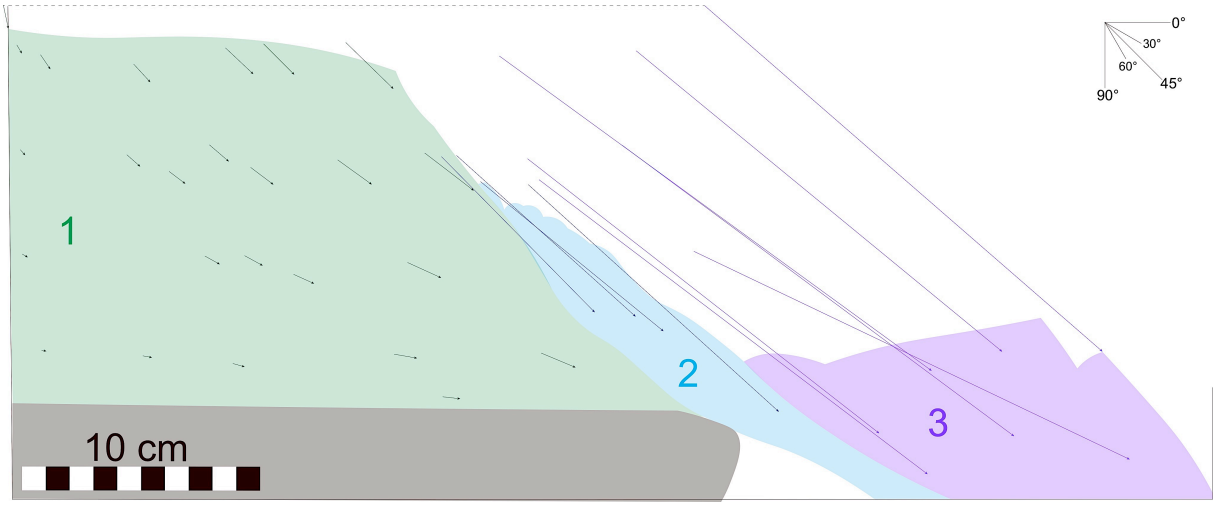

Fig. 31: Visualisation of the displacement field for experiment E5 from β 1.00-1.73. The model is divided into two colours representing coherent blocks. The top black dashed line represents the original surface level and start length of the model. Vector arrows represent the shortest displacement path and angle of translation, pointing from the initial position to the final position of the traced particles.

Displacement vectors is block 1 are relatively short and the dip angle trend changes gradually from a 45°-50° angle near the surface to a lower dip angle of 5° towards the base. The length of the displacement vectors increase towards the boundary between block 1 and 2 from only a few mm to 2.5 cm. The displacement vectors in block 2 are relatively longer than in block 1, with a length variation of 9-13 cm and a dip angle of 40-45°. The traced particles in block 3 have been displaced 19-22,5 cm, with a general dip of 40°, while the parts of block 3 near the base is displaced at an 25° angle.

5.2.3 Particle path for model E1 and E3

The combined traced path of single points forms a flow pattern of the deformed model, here presented in a vertical section. The particle traces also indicate a relative strain rate and vorticity within the strain intervals. Traced points are easy to follow and recognisable throughout the experiment. The intervals chosen are the same critical points in deformation history as the figures illustrating structural evolution. One model from each group is chosen, E1 from group 1 and E3 for group 2. The displacement field figures are made by matching points on photographs of the initial unstrained model and the fully extended model in illustrator and cross-referenced with the corresponding video.

Description of particle path E1

The particle paths are traced for model E1 using photos shot during the experiments and are selected at a maximum interval of 1.25 seconds, which equals to a maximum of 9.6 mm according to the mean extension rate. Each figure illustrates the particle path within 10-15% extension, and the beta-factor interval (β) for each stage is stated in Fig. 32 and described below. The extension direction is towards the right.

β 1.00 – 1.15 (Fig. 32A): The movement vectors are shortest to the left in Fig. 32A and increases generally towards the right. The general dip angle trend of the particle paths is 30°, while the longest paths towards the right has a steeper general trend of 40° towards the right.

β 1.15 – 1.23 (Fig. 32B): The particle paths in this interval show two apparent trends, where the right side is more active than the left side. The left side show very short paths and a wide range of dip angles; from left to right the trend changes from steep (60-70°) to intermediate (30-60°) to near horizontal. The right side has longer particle paths and shows a relatively uniform dip angle of 30°. There is a sharp division of the two trends, which corresponds to the formation of F1 Fig. 10B. The shortest particle paths are found in the footwall, while the longer paths are found in the hanging wall.

β 1.23 – 1.35 (Fig. 32C): At this stage, the larger part of the model shows longer particle paths. The relatively inactive left side seen in stage B show ca. 2.5 cm long displacement paths with a varying orientation. The area in close proximity to the fixed vertical wall and above the base show very short displacement paths of ca. 2 mm. The longer paths are steeper a few cm above the base layer towards the left side and flatten towards the area left of the ramp break-off zone. Above the ramp geometry and towards the right, the paths show a more

uniform trend of 4 cm and a 20-30° angle. The activated left side corresponds to the footwall of F3, seen in Fig. 10D.

β 1.35 – 1.50 (Fig. 32D)*:* The particle paths show the same general trend as in stage C. The largest difference is a slightly steeper angle of the particle paths of the particles that move towards the break-off zone of the ramp geometry.

β 1.50 – 1.60 (Fig. 32E): Particle paths above the flat basal geometry to the left are relatively shorter than the particle paths above the break-off zone and towards the moveable vertical wall. In the model from left to right; the particle path orientations change from intermediate 40°, to a shallow angle of maximum 11° before the ramp break-off zone, to a curved and a relatively steeper angle of ca. 30° above the ramp and finally towards the right is a more uniform trend of 15-20° in the upper parts and near horizontal geometry along the extended base.

β 1.60 – 1.70 (Fig. 32F): Again, as in stage B, the particle paths show two trends. The left side of the model show very short paths with relatively low angles. The particle paths are significantly longer from the break-off zone of the basal ramp geometry and towards the right. The general trend of the paths is a ca. 20° dip towards the right, with steeper dip up to 40° above the break-off zone and a lower dip of ca. 17° above the lowermost part of the ramp geometry and near horizontal angles near the base of the vertical moveable wall.

β 1.00 – 1.70 (Fig. 32G): The total particle path from 0-70% extension is illustrated by combining the particle paths from the previous steps A-F. The area closest to the fixed wall and near the base on the left has very short particle paths. Particles that have moved a relatively long way above the flat parts of the basal geometry have a steeper angle near the surface and flattens out towards the base. Particles that moved from the flat basal layer and over the ramp geometry show a generally curved steepening downward geometry, meaning that the path is steepening downwards towards the right. Particles that originated near the moveable wall show a particle trace with a relatively long path, where the orientation is steeper of 40° and a quite uniform trend near the surface, the angle decreases with increasing extension. Particles that originated near the base also have similar particle traces as the basal geometry.

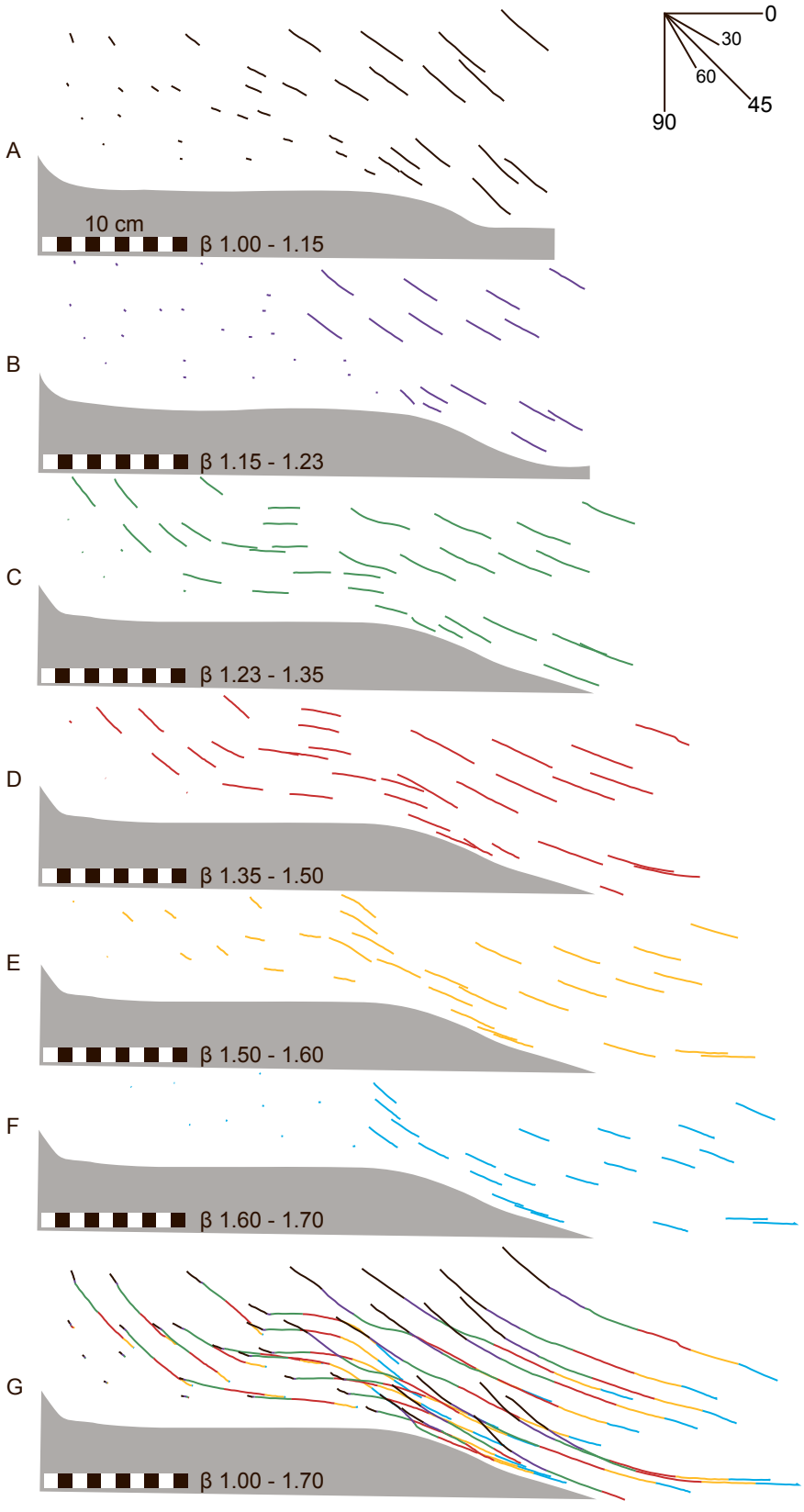

Fig. 32: Figures A-F illustrate the particle path traced in six β-factor intervals, illustrated in reference to the fixed vertical wall (left). The extension direction is towards the right. Figure G show the

collective particle path from the initial stage to the final stage. The scale is 10 cm and the coordinate system in the top right corner reference the angular relationship.

Description of particle path E3

The particle paths for model E3 are traced using photos shot during the experiments and are selected at a maximum interval of 1.25 seconds, which equals to a maximum of 3 mm according to the mean extension rate. Each figure illustrates the particle path within 6-27% extension, and the beta-factor (β) interval for each stage is stated in Fig. 33 and described below. The extension direction is towards the right.

β 1.00 – 1.07 (Fig. 33A): The whole plaster cover is in motion. The particle paths decrease in length away from the moving wall, while the dip angle trend is steeper in the upper right corner with ca. 45° angle and decreases towards the base and towards the left.

β 1.07 – 1.13 (Fig. 33B): Two trends are apparent at this stage, where the left side is nearly still while the right side is moving ca. 2 cm on average. The particle traces are relatively planar and uniform in the upper right corner, while towards the left boundary their collective form is curved and flattening downwards from 55° near the surface to 15° along the base.

β 1.13 – 1.33 (Fig. 33C): The left side is again activated as shown by 1-2 cm long particle paths with a full range of dip angles form a near vertical dip angle near the surface and a horizontal dip angle towards the base. The right side moves on average 5.5 cm and shows the same trend of a gradually shallower dip from 45° near the surface and horizontal towards the base as the left side.

β 1.33 – 1.60 (Fig. 33D): The gradual dip angle change from near vertical near the surface to horizontal near the base is still strong in the left side, while slightly weaker on the right side. The paths are slightly shorter of ca. 3 cm on the left side than the right side of ca. 6 cm.

β 1.00 – 1.60 (Fig. 33E): A larger rotational trend is apparent in the left side compared to the right side from the collective particle paths. The full trend is a steeper dip angle near the surface and a near horizontal near the base.

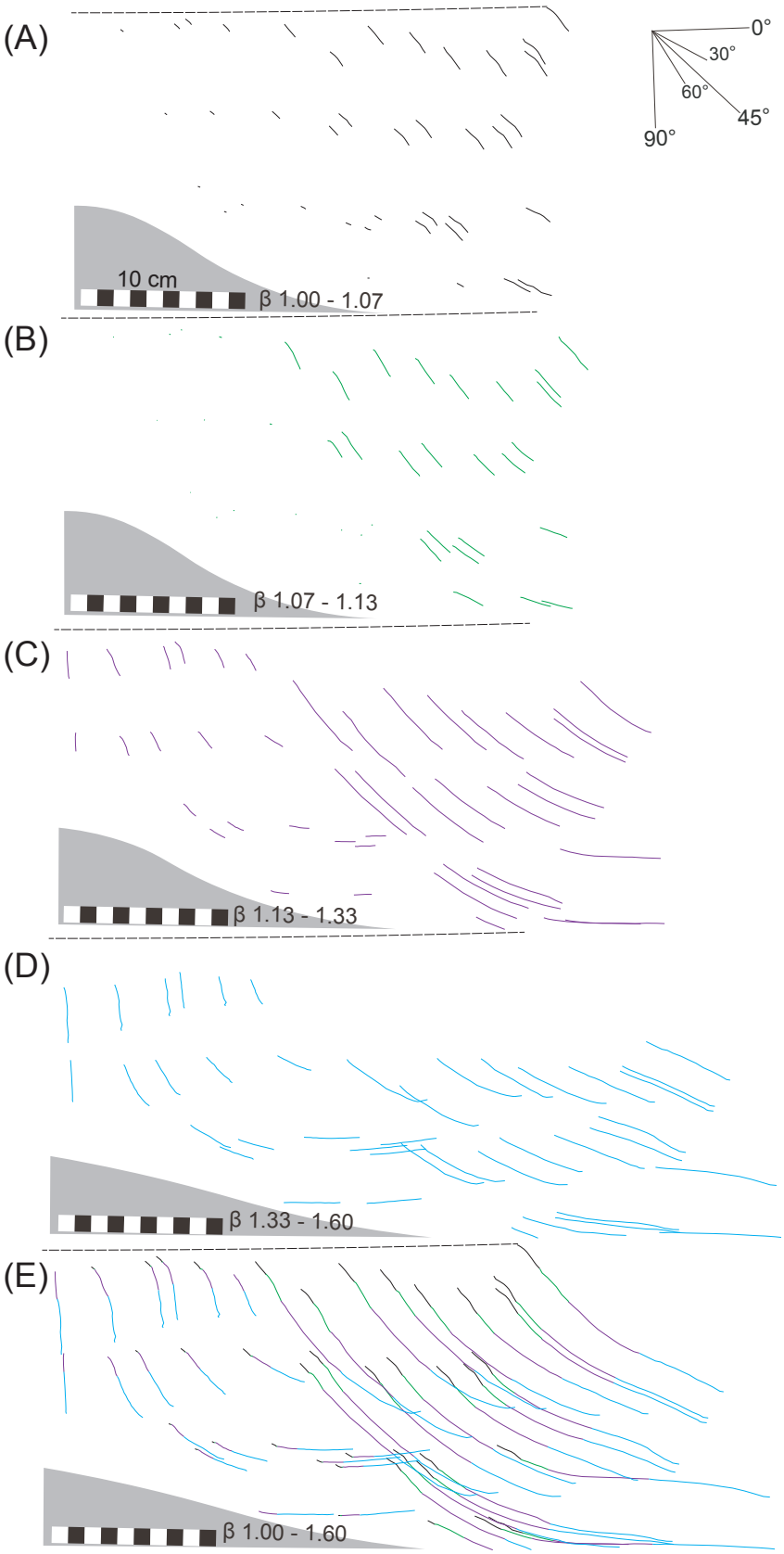

Fig. 33: Figures A-D illustrate the particle paths traced in four strain intervals, illustrated in reference to the fixed vertical wall (left). The extension direction is towards the right. Figure E show the collective particle path from the initial stage to the final stage. The scale bar represent 10 cm and the coordinate system in the top right corner reference the angular relationship.

5.2.4 Formation of faults during increasing strain

Plotting and comparing results from each experiment can estimate the amount of strain needed to produce brittle structures. The beta-factor (β) representing the point of the first brittle structures for each experiment and for each side is plotted as black boxes in Fig. 34. The grey boxes represent the amount of strain accumulated when a fault plane cuts the plaster column from base to surface. The percentage interval from the formation of the first brittle structure to the formation of a through cutting fault plane is indicated with numbers in the graph in Fig. 34. The plaster column height of the models vary, the column height is 13 cm for E1, ca. 17 cm for E2, 20 cm for E3 and 15 cm for both E4 and E5. The dip angle of the first master fault is reflected on the time it takes between the first formations of brittle structures to a through-cutting fault plane. The first brittle structures form in the β-interval 1.02 – 1.10, while a through cutting fault plane forms within an β-interval 1.07-1.17 in the five models presented in this thesis, and all models have generated at least one through-cutting fault plane within β 1.23. All plotted faults in Fig. 34 are active to the end of the experiment and their length and displacement development is presented in this chapter below.

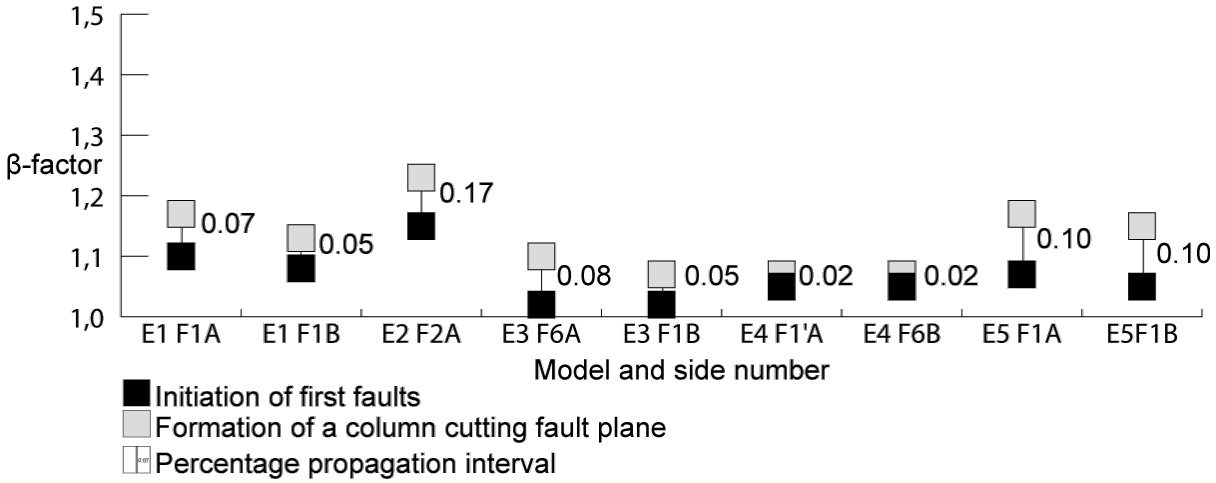

Fig. 34: The x-axis represents the model and profile plane name, e.g. E1 A means model E1 and side A. The y-axis represents the β-factor, or the amount of linear strain accumulated. β 1.00 represents an unstrained model. The grey boxes indicate the β-factor of first formation of brittle structures, in the corresponding model. The black boxes indicate the β-factor at which a fault plane cutting the plaster cover from the base and through the surface is formed. The numbers placed next to the line connecting the grey and black boxes represent the amount of strain accumulated in the interval between the formations of the first brittle structures to the formation of a through cutting fault plane.

5.2.5 Fault initiation angle during extension

The initiation angle of newly formed faults is plotted against the amount of strain at the time of formation. The plot does not include any development of the fault dip angle. Group 1 and group 2 are plotted separately in Fig. 35 and Fig. 36, respectively. The plots show very different trends. Group 1 have a wide range of initiation angles, from shallow ca. 10° to a steeper maximum of ca. 68°. The large majority of the initiation angles lie within the moderate dip angle interval between 30° and 60°. The large majority of faults of group 2 initiates at a dip angle between 30° and 75°. New faults form throughout the experiments of group 1. In group 2 the formation of new faults generally end at β 1.30, excluding a few outliers. The average initiation angle of experiments of group 1 differs from ca. 50° in E1 to 39° for E2. The average initiation angle of experiments of group 2 is 57.5±1°. Several large fault planes form throughout the experiments in E1, while only one large fault plane form in the experiments of group 2, excluding some antithetic faulting towards the very end.

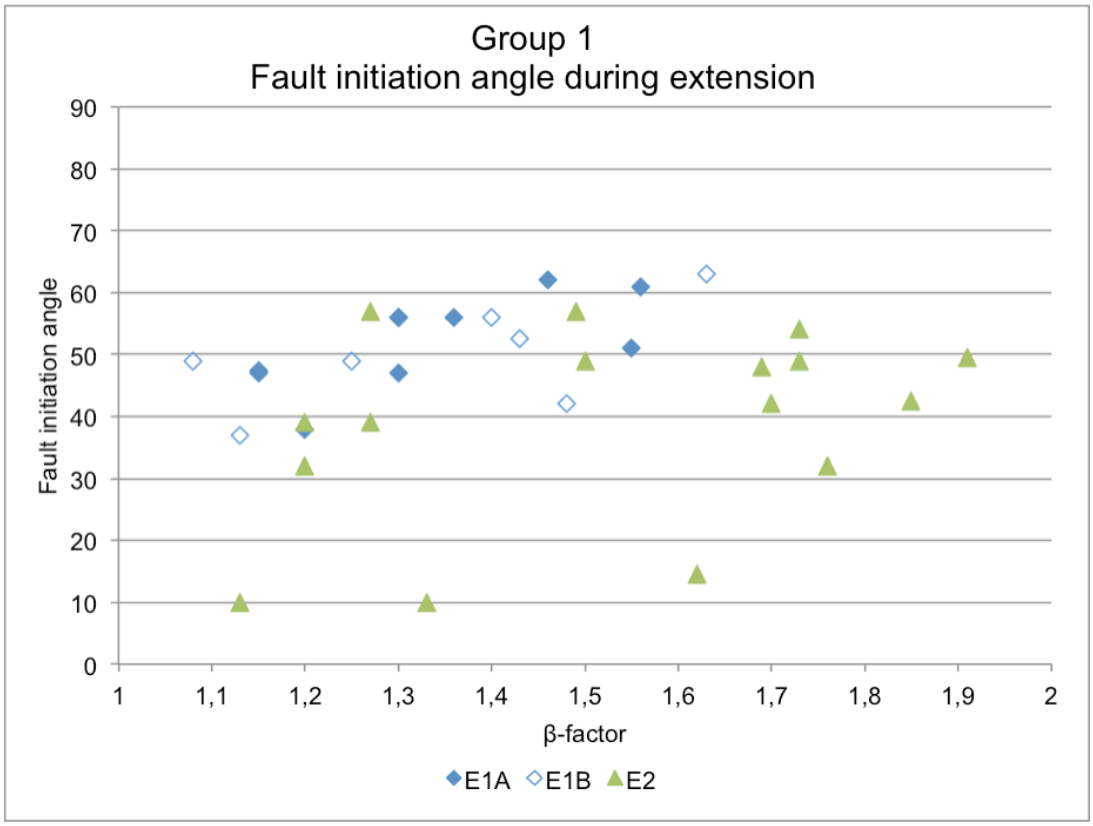

Fig. 35: Fault initiation angle of newly formed faults in experiments E1 side A and B and E2 side A.

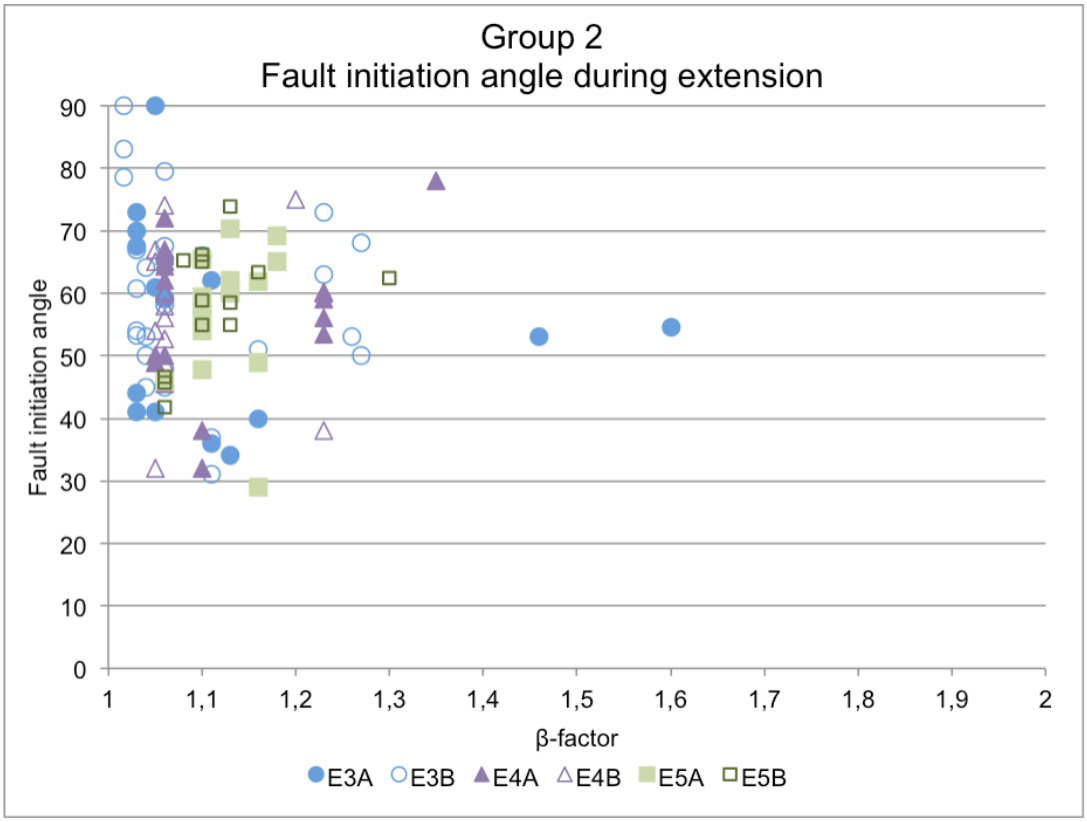

Fig. 36: Fault initiation angle of newly formed faults in experiments E3-E4 side A and B.

5.2.6 Cumulative plot of faults during extension

Faults of all sizes are included in these plots to compare the amount of minor deformation structures between the experiments. The data is plotted with a log-log scale in order to investigate the relationship between the two factors. For the normal plot, see Appendix B: Additional results.

A linear trend in a log-log plot indicates a constant relationship. From the log-log plot in Fig. 37, there is a curved trend flattening upwards, meaning that the number of faults increases faster during the early stages of extension and flattens out during the experiment and that the relationship is not constant. The largest cumulative number of brittle structures is found in model E3 with 163 faults. The smallest cumulative number is found in model E1 with 16 faults visible on side A. Most of the models average to a cumulative fault count of 36 faults.

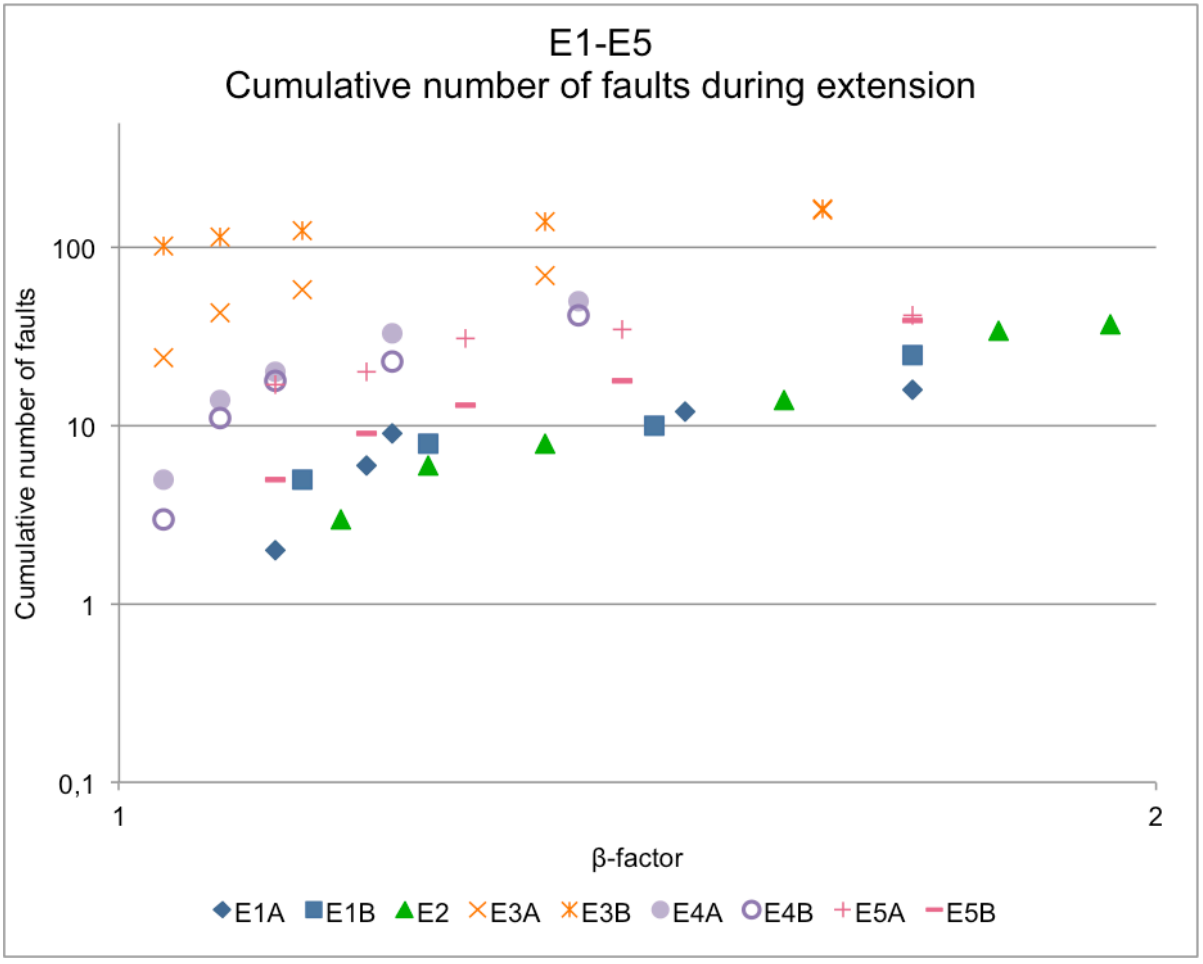

Fig. 37: Log-log plot of the cumulative number of faults formed during extension for experiments E1, E2, E3, E4 and E5.

5.2.7 Evolution of master fault length during extension

The fault length of master faults is plotted against an increasing strain, or β-factor. The results are divided into two groups. The first group consists of E1 and E2 modelled in the wide box set-up and group 2 consists of E3, E4 and E5 modelled in the narrow box set-up. The corresponding fault strands on side A and B are plotted in the same plot. Note that the fault strands are numbered according to chronological time of formation for each profile plane A and B, hence numbers do not always correlate and are described for each plot. The corresponding fault strands are labelled with model reference, a roman number and the fault reference in parenthesis. The plots for each experiment are provided in Appendix B: Additional results.

The plots in Fig. 38 and Fig. 39 show two general trends of the development of maximum displacement vs. fault plane length. The first trend is a dominating increase in fault length compared to the amount of strain up to an average of β 1.35 for group 1 and β 1.15 for group 2, where the second trend is dominated by a very small increase in fault length compared to the amount of strain imposed. Some fault lengths of group 1 are getting shorter, which is a result of newly formed faults cutting the existing faults, therefore shortening the length of the relatively older faults. The intersected fault planes still accumulate displacement after shortening.

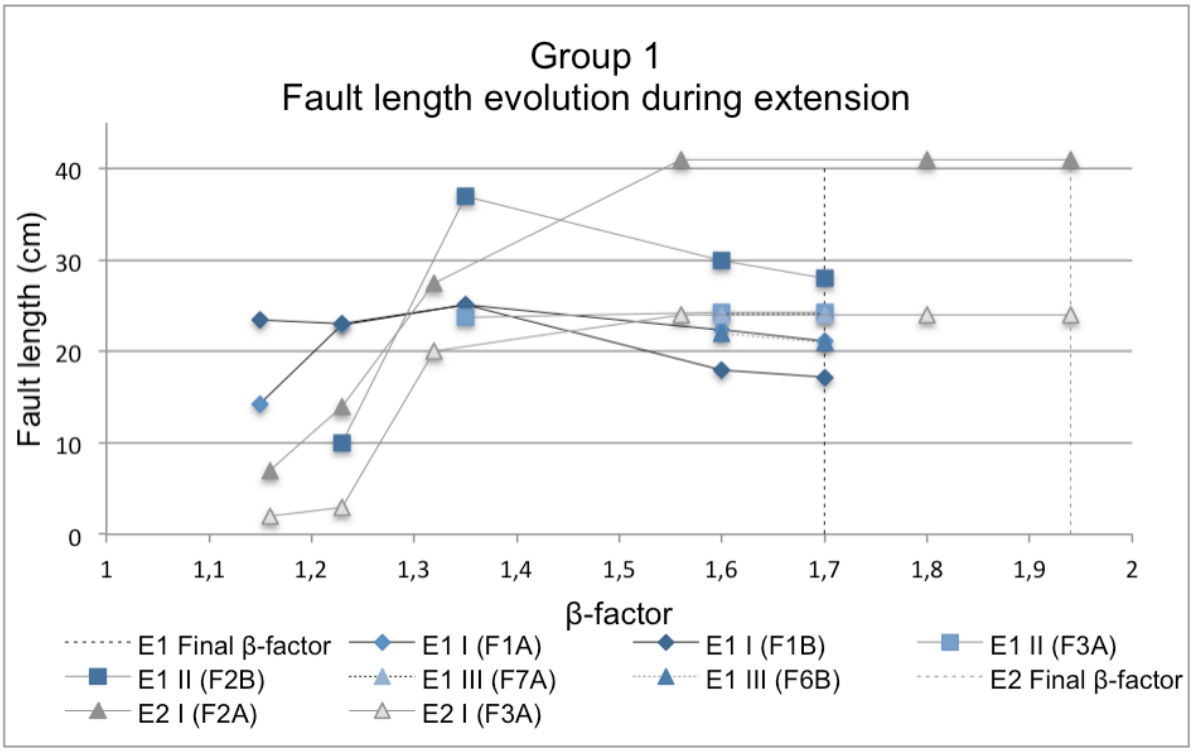

Fig. 38: The length of master right-dipping fault planes in models E1 (blue) and E2 (grey) is plotted against the β-factor. The dashed vertical lines represent the total stretching accumulated in the experiments.

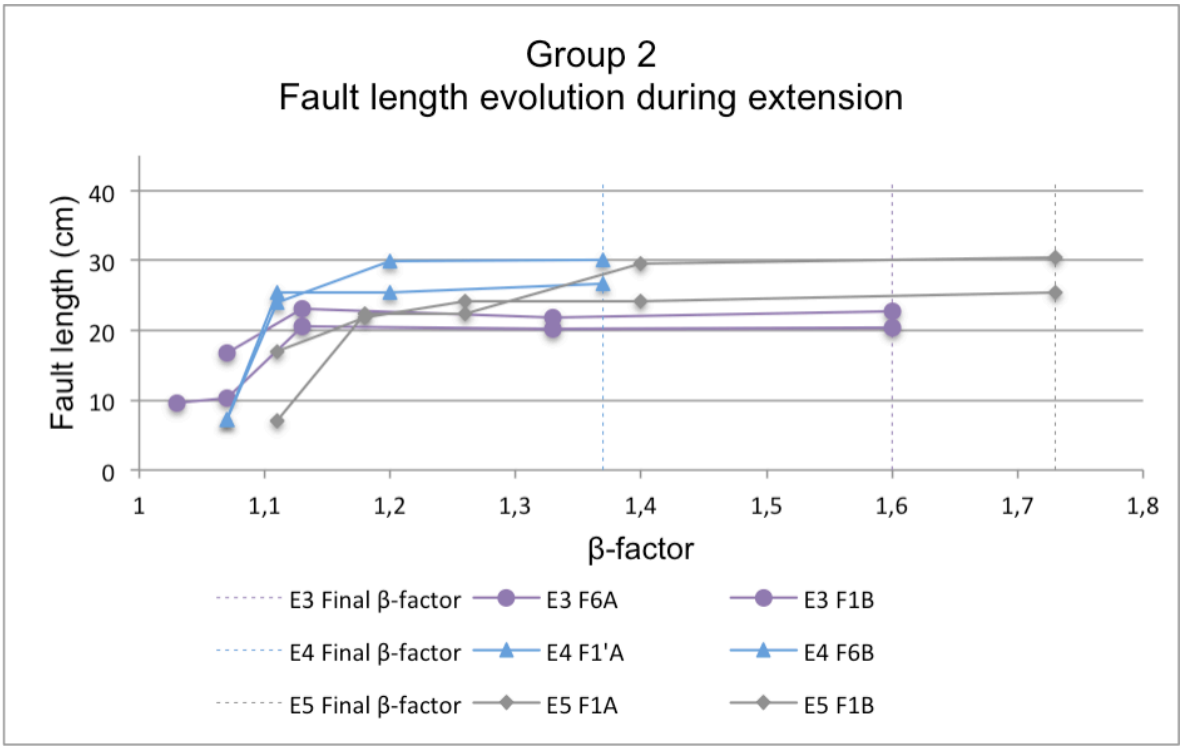

Fig. 39: Fault length evolution in experiments E3 (purple) E4 (blue) and E5 (grey). Corresponding fault strands on side A and B of the models are plotted in the same colour and indicator style.

5.2.8 Maximum displacement with fault length

Displacement accumulates along the fault planes during the experiments, however the largest offset is not always equal to the surface displacement. The maximum displacement along a fault plane is plotted against the total length of the master fault planes in the models. The plots of maximum displacement and length relationship for group 1 (Fig. 40) and group 2 (Fig. 41) show two dominant trends. The first trend is a relative large increase in length compared to displacement up to a length varying between 20-29 cm with an average value of 24 cm, with faults E1 F2B and E2 F2 as outliers. These latter faults are master ramp-flat-ramp faults, which accumulate displacement at a relatively steady rate (blue-crossed line and blue-boxed line, for E1 F2B and E2 F2, respectively in Fig. 40. A relatively low average of 3.8 cm displacement accumulated within the interval dominated by fault length accumulation, which is a D_{max}/L of 0.15. The second trend is the relative large accumulation of maximum displacement relative to the fault length. From this it is concluded that the length and displacement accumulation is not a constant relationship, but a two-step process. A two-step model is consistent for the general fault population where the length accumulation dominates over displacement accumulation until the maximum length is achieved. When the maximum length is achieved, usually when the plaster column is cut through, the fault plane accommodates strain by displacement along the slip-surface and the length accumulation is weak.

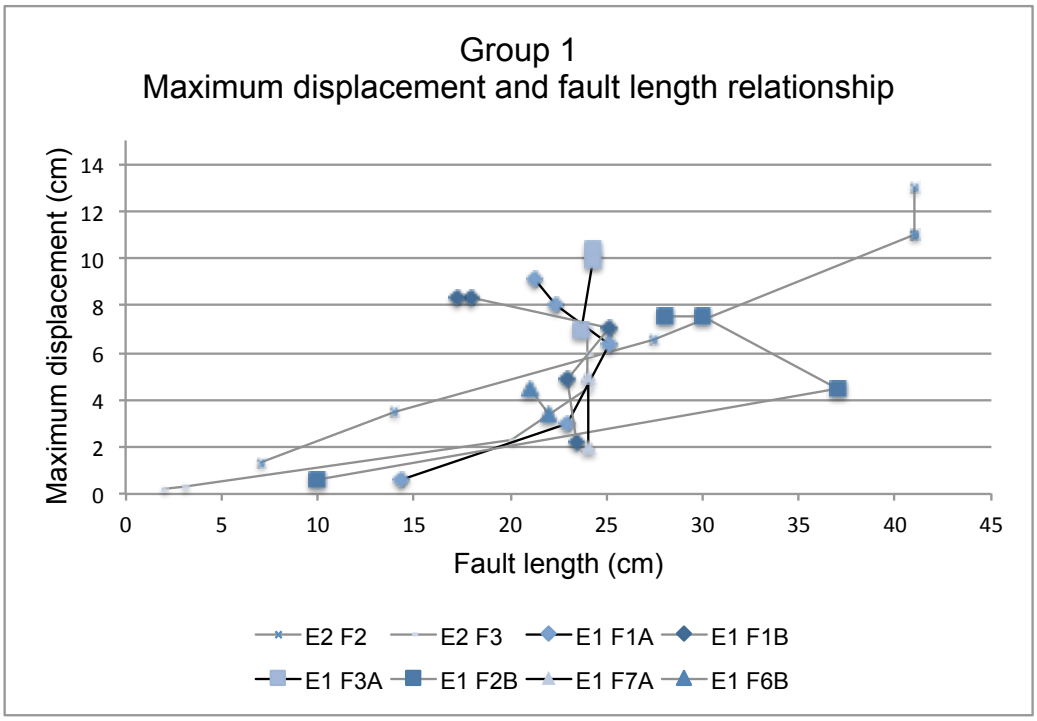

Fig. 40: Maximum displacement plotted against the total length of a master fault plane. Some of the major fault planes are cut by younger faults, leading to a shortening of the fault plane length.

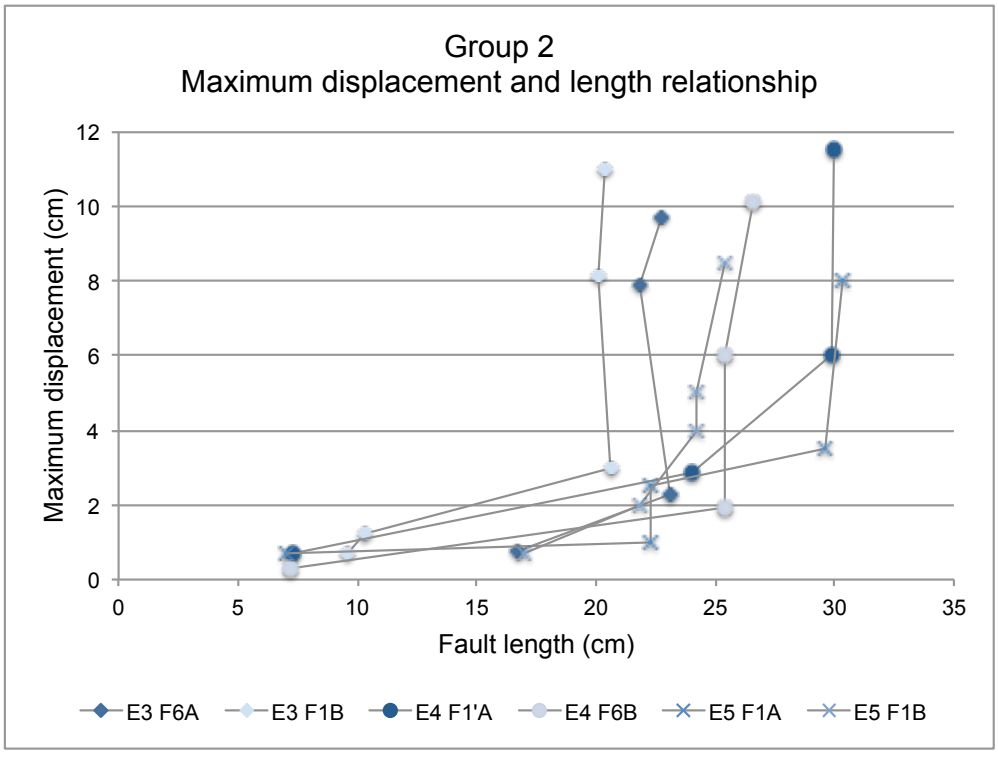

Fig. 41: Maximum displacement plotted against the total length of a master fault plane. Indicators of fault strands on side A and B is coloured dark and light blue, respectively. Fault strands corresponding to the same fault and model has the same indicator, which is a diamond for E3 a circle for E4 and an x for E5.

5.2.9 Maximum displacement-length ratio with increasing strain

The maximum displacement-length ratio (D_{max}/L) is plotted against the increasing strain, or β-factor for experiments E1-E5 (Fig. 42). Their line plots generally increase with increasing strain, but the slope also decreases gently with increasing strain to form a gently curved plot. This indicates that maximum displacement increases compared to the fault length with strain, and also that the D_{max}/L-β slope is relatively lower towards the end of the experiment.

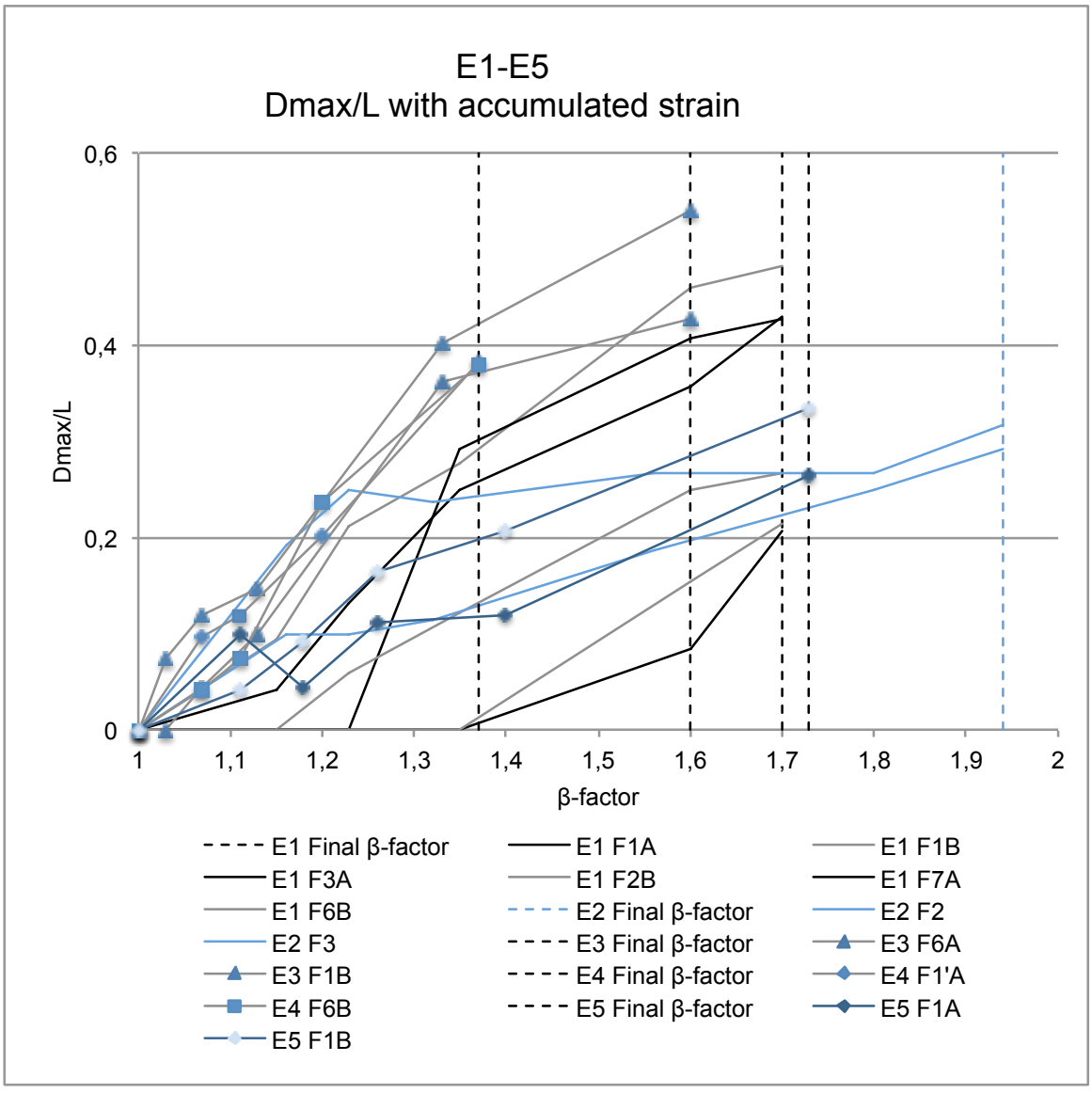

Fig. 42: Maximum displacement and length ratio (D_{max}/L) measured for each of the master fault planes in E1, E2, E3, E4 and E5 is plotted against the accumulated amount of strain (β).

CHAPTER 6 Discussion

6.1.1 Introduction

In this chapter the results are summarised in short, discussed and set in connection to general fault growth patterns and mechanisms. The structural evolution and the associated numerical results are compared to previous work in experimental modelling, field examples and interpreted seismic sections. The final stages of all experiments are collected in Fig. 43 and Fig. 44 for group 1 and group 2, respectively.

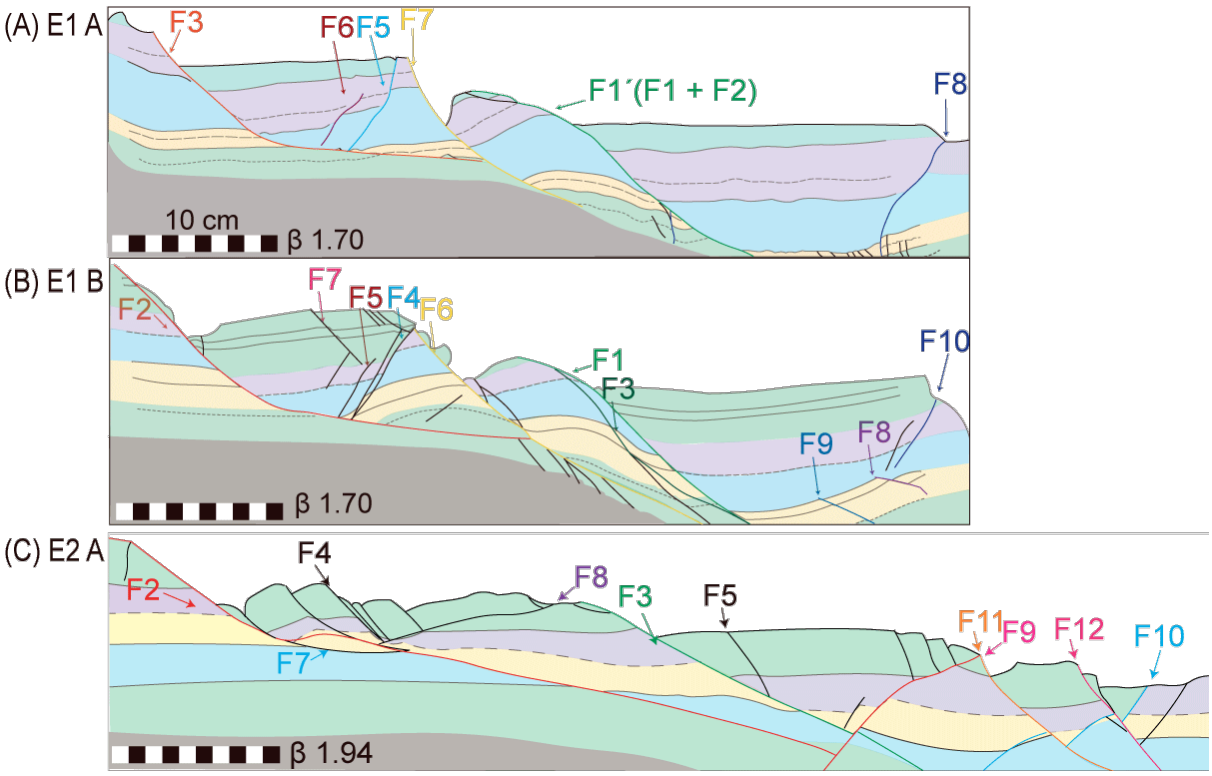

Fig. 43: The final stages of experiments E1 and E2 of group 1: (A) Side A of E1 (B) Side B of E1 (C) Side A of E2. The models formed several fault planes and a series of horst and graben structures. A few faults have moved out of view due to the model set-up, and are not referenced in the end model: E1 F4A and E2 F1.

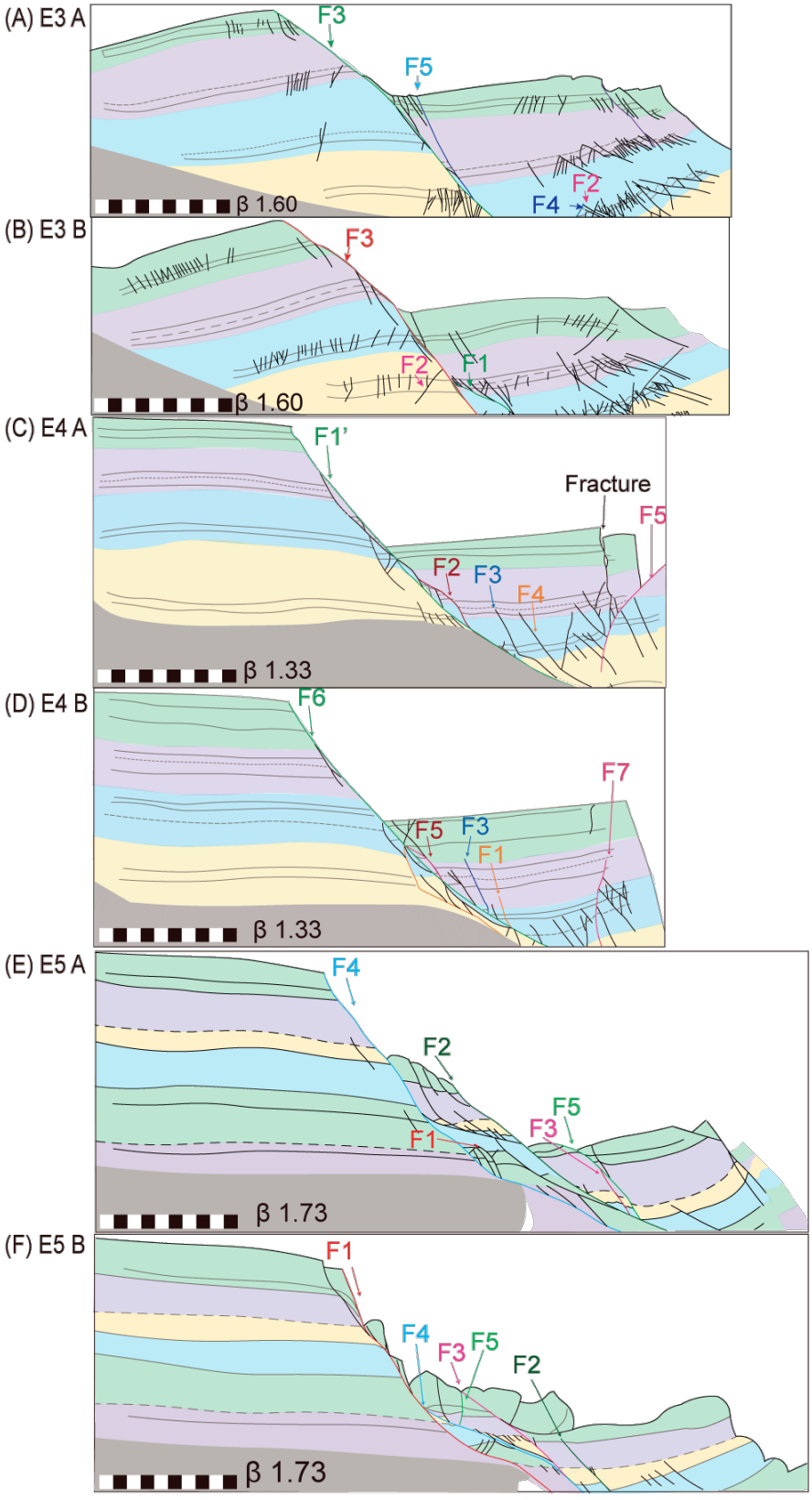

Fig. 44: The final stages of experiments E3-E5 in group 2: (A) Side A of E3 (B) Side B of E3 (C) Side A of E4 (D) Side B of E4 (E) Side A of E5 (F) Side B of E5. The models formed one major fault plane through varying processes.

6.1.2 Fault initiation

As extension starts the whole plaster medium is flowing in a ductile manner to fill the given space during the first β 1.10. The first brittle structures form in the β-interval 1.02 – 1.10, while a through-cutting master fault plane forms within β 1.23 for the five experiments presented in this thesis. According to Fossen et al. (1996), the faults with the largest displacement are formed at β 1.25. A column-cutting fault plane is formed within interval of 7-17% after the first brittle structures initiate. The location of fault nucleation is in the rightmost 5-10 cm of the vertical moveable wall at the interface between the basal layer and the plaster cover, where the faults propagate upwards, which is consistent with Odinsen (1992). Odinsen (1992) finds that the first fault is established by ca. 5% extension, which is within the 2-10% interval observed in this thesis. The average β-factor for fault initiation found in this work is ca. 6%.

Amount of strain accumulated before brittle fault initiation is dependent on the properties of the plaster cover. A less viscous plaster cover will flow relatively easily without fracturing as in E1 and E2, and therefore accumulate a larger amount of strain before brittle deformation. Hence the strain at fault initiation is a measure of rheology in the experiments (Fossen et al., 1996). Brittle deformation was visible in E3 after only 5 mm, or β 1.016, while it took almost 5 cm to form a visible fault in model E2 at β 1.13. The visibility of brittle structures may be affected by the nature of marker stripes. The plaster to water ratio was 1.33 and 1.66 for E1 and E2-E5, respectively. A large number of near vertical fractures without visible displacement parallel to the fracture planes formed in run E3. According to experimental data, such fractures form under a contractional stress orientation under low pressure. This is consistent with subsidence of the plaster medium induced by the accommodation space given as the extension increases.

A general trend of increasing or decreasing dip angle with increasing strain is not found for the experiments in this thesis. Average initiation angle of faults throughout the experiments of group 1 differs from ca. 50° in E1 to 39° for E2. The average initiation angle of experiments of group 2 more consistent and is 57.5±1°. The large discrepancy within group 1 may be a result of the relatively larger number of faults in E2 compared to E1. Only one large fault plane forms in the experiments of group 2, excluding some antithetic faulting towards the very end, which may form due to edge effects.

6.1.3 Basal layer geometry and their effect on the plaster cover

The first brittle structures form at the interface between the plaster cover and the basal baryte layer and close to the moveable vertical wall. The plaster and basal layer is set in motion due to the given space, the weight of the plaster cover and the adhesion on the interface between the wooden vertical wall and the baryte mixture leading to stretching towards the right. The amount of movement of the plaster is largest near the vertical moveable wall, as seen in the particle trace models for E1 (Fig. 32) and E3 (Fig. 33). The nucleation area might be where the strain patterns change, meaning that the strain imposed on the model is not distributed into the relatively viscous basal baryte layer at the same rate as in the plaster cover, leading to a local increase in strain in the less viscous overlying plaster cover.

Most of the experiments had a relatively thick and flat basal baryte layer (Fig. 26), which may inhibit the initial strain accumulation in the overlying plaster cover towards the fixed wall to reach the sufficient amount for a large rotational movement. If the basal viscosity allows it, a ramp dipping in the extension direction forms at the end of the basal layer. The large majority of faults were formed above the break-off zones of the ramps, where the basal slope increases. The basal ramp can be treated as a very low-angle ramp-flat-ramp fault. A high relief of the basal layer promotes movement within the hanging wall. Some adhesion forces act between the baryte and the plaster cover as well.

The geometry and relatively low viscosity of the pre-made basal ramp in E3 promoted footwall rotation. The largest amount of footwall rotation was found in this experiment, as seen in the displacement path and particle trace in Fig. 29 and Fig. 33, respectively. It should also be considered that the fixed wall was gently tapped using a hammer during the experiment.

When comparing the two end-members of basal layer relief it is apparent that the structural complexity and deformation zone in the plaster cover increases in width with increasing relief and dip angle of the basal layer. This is consistent with all the models presented in this thesis. In E3, where the fault plane formed in front of the pre-made basal ramp, the fault zone was quite narrow of ca. 3 cm. The widest observed fault zone of the experiments is found in E5 with ca. 6 cm, it formed as a result of sequential faulting in the plaster cover above a relatively viscous basal layer with a steep relief. This steep zone leads to a series of sub-planar faults to form in a wide zone.

6.1.4 Master fault formation

This section focuses on the growth patterns in the 7-17% extension interval from the initial formation of brittle structures to an established through-cutting fault plane. Larger faults form by cutting through or connecting minor faults. The master fault geometry is usually dependent on the formation process. Faults nucleating at the interface between the plaster cover and the basal layer usually form a steepening upwards geometry. The further propagation and establishment of a through-cutting master fault is highly dependent on the initial structures. The orientation and distribution of these first generation faults varies and they are the brittle expression of a changing strain pattern as the model is extended. Evolution of master fault formation in the models presented in this thesis follows four trends: (i) segment linkage (ii) footwall stepping segment growth, (iii) ramp-flat-ramp, and (iv) shifting fault plane trajectories.

(i) Segment linkage

Irregular master fault planes may form as a result of segment linkage, as seen in models E2 and E3B. Similar structures observed in an outcrop in Taranaki, New Zealand (Fig. 45A) is interpreted to be an array of minor rotated antithetic faults bound by two normal faults in a relay zone (Childs et al., 2009). Segment linkage structures can be observed as they form in plaster experiment E3B (Fig. 45B). Two segments propagate towards each other; segment one from the base and up and segment two from the surface and downward. Their fault tips overlap, curves towards each other and link up to form a horse (Fig. 45C). A horse forms between the two segments with varying internal deformation. The horse formed in E2 show some internal deformation in the form of compression, while the example from model E3B was faulted by a set of minor antithetic faults before the horse-formation and was subsequently faulted by several synthetic faults. Cross-sections of vertical relay-zones are rare and associated data is limited, therefore their observed temporal development in the plaster models can contribute to the interpretation of structures seen in nature. This example indicate that the minor or secondary structures are formed prior to the horse formation and not after, which is in contrast to other models (Childs et al., 2009). This may also indicate that faults form as an array within a strained three dimensional lens, which is consistent with the coherent fault model (Walsh et al., 2003).

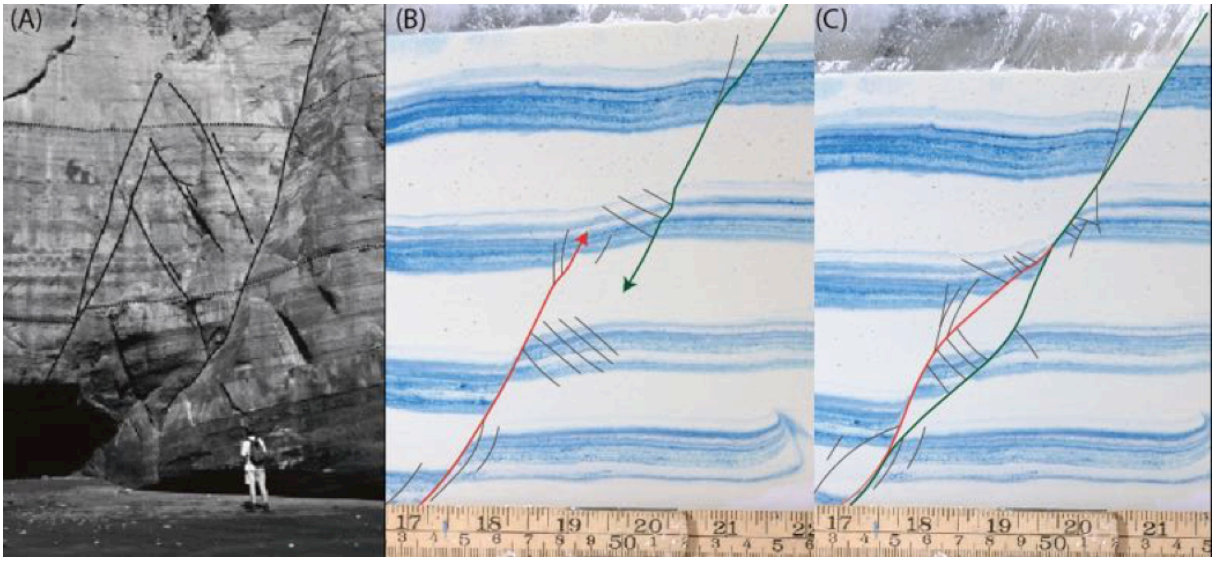

Fig. 45: Formation of antithetic faults between two fault strands before segment linkage from a field example and plaster experiment E3B. The main faults in the plaster experiments are coloured red and green. (A) Field example of a zone of antithetic faulting and rotation bound by two normal faults, the fault segments are lined in black, from Taranaki, New Zealand (Childs et al., 2009). (B) The two main faults propagate towards each other and overlap at β 1.36. (C) The faults have linked together to form a horse at β 1.43. The upper and lower scale bar rows represent inches and cm, respectively. Note that the experiment photos are not flipped vertically, and they are therefore the mirrored image of the experiment illustration in Fig. 16. Only the largest structures close to the segment linkage is illustrated. The extension direction is towards the left.

(ii) Footwall stepping segment growth

An array of first generation of sub-parallel minor faults cut sequentially upwards and into the footwall. The minor faults are initially formed as separate segments and each set may range from a high angle, as in E4A and B (Fig. 19C and Fig. 20C) to an intermediate angle as in E1B (Fig. 11B) and E3A (Fig. 15C). The displacement is distributed between the minor faults at this stage. A large master fault plane cuts through the first generation of faults, which is left relatively inactive in the footwall and hanging wall. A number of cut-off fault strands and small lenses are visible in the damage zone. The initial fault plane is irregular and is evened out by asperity bifurcation, which again may form several smaller lenses and heavily deformed zones along the fault plane.

(iii) Shifting fault plane trajectories

A group of faults propagate upwards and spread out in a zone of relatively larger faults and associated splay faulting, as seen in model E5 side A (Fig. 23). The larger faults are initially

sub-parallel, with the leftmost fault accumulating the most strain. The fault plane trajectory shifts and cuts the sub-parallel fault planes obliquely to form a ramp-flat-ramp fault. The abandoned fault planes in the footwall forms smaller horses in an extensional duplex and the splay faults in the hanging wall forms an array of riders, also called a listric fan (Gabrielsen et al., 2001). The fault plane trajectory again shifts towards the leftmost existing fault planes to form an irregular, or wavy, fault plane. A shifting fault plane trajectory generates a relatively wide fault zone, where displacement is distributed in a heavily faulted zone. A vertical section through the fault zone shows a column of stacked horses and riders.

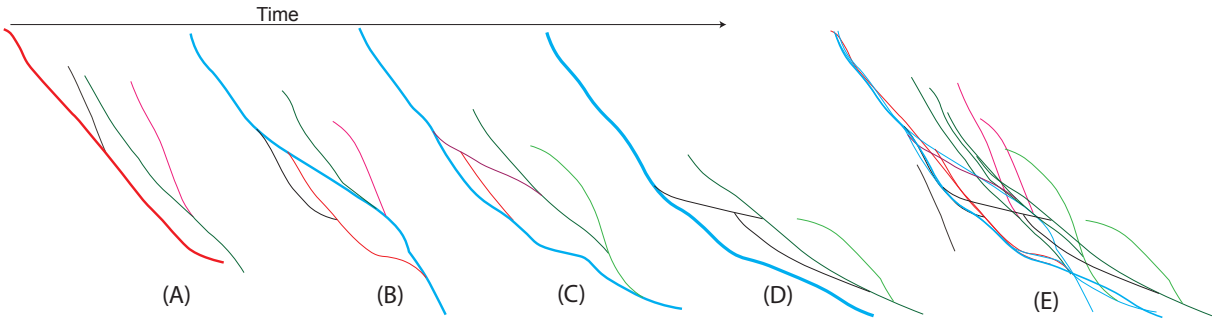

Fig. 46: The shifting master fault plane trajectories and associated large fault planes in E5A are illustrated at different stages. The thickest line represents the most active fault plane. Fault plane colours are the same as in the experiment illustration in Fig. 23, where the full structural complexity is illustrated. (A) β 1.18 (B) β 1.26 (C) β 1.40 (D) β 1.73 (E) Stacked fault planes from stages A-D show an anastomosing pattern.

(iv) Ramp-flat-ramp

Ramp-flat-ramp fault geometries are found in many experiments with varying orientations and reliefs, from which three types are identified (Fig. 45): (1) A ramp-flat geometry may be inherent in the basal layer as the horizontal interface between the baryte and the plaster cover, the ramp end geometry and the base of the box. (2) Low-angle ramp-flat-ramp faults bound an extensional basin in models E1 (Fig. 43A and B) and E2 (Fig. 43C). (3) High angle ramp-flat-ramp geometries along irregular fault planes.

An example of type 2 formed by a listric fault plane propagating downwards from the surface and over the ramp in E1, while type 2 in E2 formed by segment linkage. Type 3 was formed in E3 by segment linkage (Fig. 45). The similarities of these three types are the associated hanging wall strain pattern. The hanging wall rotates anti-clockwise as it moves down in the restraining bend where the gradient decreases over the flat and rotates clockwise over the releasing bend where the gradient increases over the ramp. The hanging wall deformation

associated with ramp-flat-ramp faults is discussed in section 6.1.6. These faults have similar geometries to low-angle detachment faults, which are important for accommodating extension in the lithosphere (Lister et al., 1986).

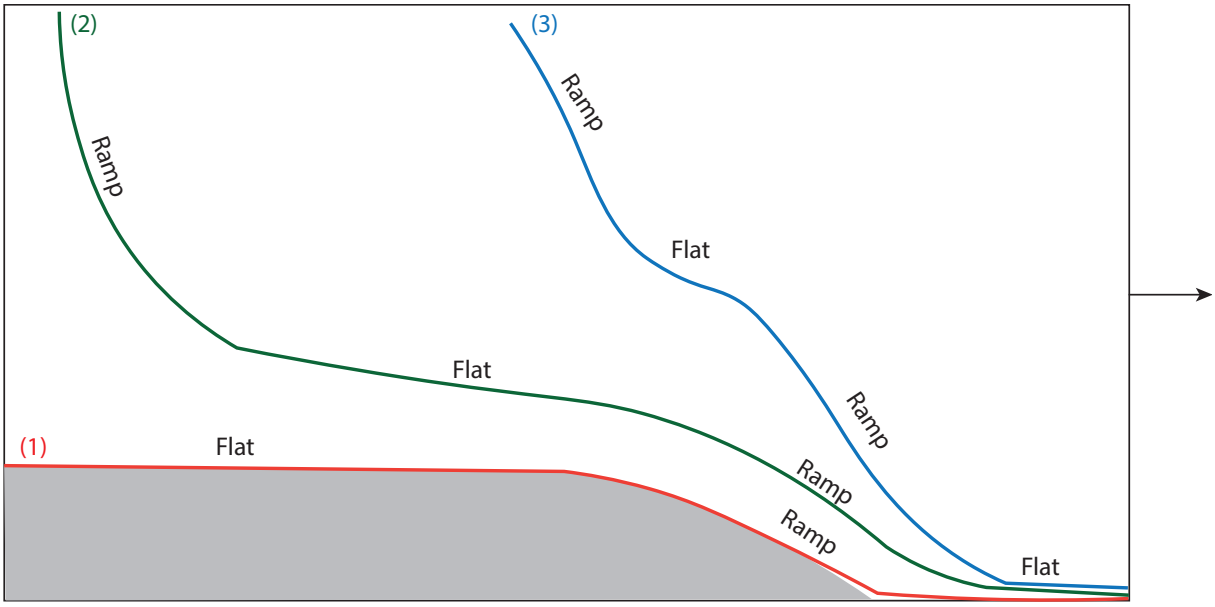

Fig. 47: Three types of fault planes with ramps and flats at varying orientations are identified: (1) inherent basal layer flat-ramp-flat, (2) basin-bounding ramp-flat-ramp and (3) high angle ramp-flat-ramp. The extension direction is towards the right and indicated by a black arrow.

6.1.5 Fault geometry evolution during extension

As the model is extended, the master faults change their geometry and accumulate displacement. Minor faults surrounding larger fault planes generally form as planar slip-surfaces and propagate with a curved trajectory to intersect with the master fault plane, as splay faults or they are rotated anti-clockwise within the hanging wall.

Plaster models presented in this thesis have produced master faults with a range of geometries such as (i) planar, (ii) listric, (iii) curved and (iv) irregular such as ramp flat ramp. The geometries are a result of the processes that lead to the formation of a master fault and the amount of secondary deformation. The first through-cutting fault plane observed forms with a planar geometry with a low angle tail towards the base or as irregular with a general planar geometry.

Models of group 1 formed several fault planes. The first plane to form in model E1 was a planar fault which developed into a gently listric fault plane. A secondary listric fault forms in the footwall propagating down from the surface to form a ramp-flat-ramp geometry, on which

the hanging wall displaces and rotates. The displacing hanging wall of the secondary fault pushes the primary fault plane to a more curved, steepening downwards geometry at the same time as it is faulted antithetically to form a graben and a horst. The horst is subsequently faulted by a curved fault plane following the ramp geometry. Another antithetic fault forms near the moving vertical wall to accommodate the subsidence and extension of the hanging wall along the base. A similar faulting pattern forms in E2. Two planar faults of different dip angles propagate from the lower right corner and upwards. One cuts the surface as a planar fault, while the other links up with a down-propagating listric fault by segment linkage to form a ramp-flat-ramp. The horse is formed at a low angle, forming a mound along the fault plane. Both faults keep their geometry, but are cut off by two younger antithetic faults near the end of the experiment to form a series of horsts and grabens. The listric geometry is preserved throughout the experiment, however the shallow and lowermost part of the fault plane is cut by a younger curved fault directly above the basal ramp in E1 and outside the ramp for E2.

Models of group 2 formed only one master fault plane, and the final fault plane geometry seems dependent on the amount of rotation in the footwall together with a reworking of the fault plane by asperity bifurcation. A large footwall rotation leads to a curved fault plane, steepening downwards as seen in E3. A smaller footwall rotation limits the fault plane secondary deformation and the initial planar fault plane geometry is preserved, as seen in E4. In model E5, the primary fault plane geometry is curved irregular, or wavy, however the fault plane is pushed gently to a more planar geometry as the footwall rotates gently.

Final master fault geometries generated in the different models are as follows, E1: ramp-flat-ramp, curved, listric and irregular, E2: ramp-flat-ramp, curved, planar and irregular, E3: curved, steepening downwards, E4: curved, flattening downwards, E5: Irregular. The initial master fault plane geometry is dependent on the fault formation processes, while a secondary geometry is dependent on footwall rotation and asperity bifurcation.

6.1.6 Master fault geometry and their effect on hanging wall deformation

Listric fault plane seen in E1 generates as a secondary master fault in the initial footwall. It forms as a relatively steep fault from the surface and flattens out to form a relatively long fault plane, on which the hanging wall is transported and rotated. These are consistent with the characteristics of an extensional basin as described in Gibbs (1984) with tilted horsts and terrace systems generated on both listric and planar normal faults. One of the reoccurring

features is the formation of horsts and antithetic faults above a relatively low-angle master fault. This is expressed on various scales and occurs as a result of changing movement patterns in a down-going block. The front of the block meets resistance as the gradient decreases while the back of the block is still moving down, this leads to rotation and compression within the block and the formation of an antithetic fault, seen in models E1 and E2.

Secondary structures such as antithetic faults and splay faults are promoted if the slope is increasing or decreasing along a main fault plane, meaning that the dip angle is gradually flattening or steepening. For the experiments in this thesis the most fault promoting areas were the section directly above a basal ramp (slope increase), above listric faults (slope decrease) and where the hanging wall extended along the base (slope decrease). Irregularities along the fault plane itself are also a significant cause of deformation. Restraining bends promote an anticlockwise rotation of the hanging wall, and a releasing bend promotes a clockwise rotation. Such irregularities promote internal shearing due to edge effects of the rotating block and a varying strain-accommodation pattern within the hanging wall. Antithetic rotation is dominating the hanging wall deformation in all models, which significantly affect the dip-angles of in the final model. Such irregularities are evened out by asperity bifurcation to form new fault trajectories, which abandon long and narrow lenses of heavily deformed plaster.

The plaster models presented in Gabrielsen et al. (2001) showed the formation of a master fault and tip-line bifurcation in the interval 5-12% and asperity bifurcation at 10-25% extension. In this thesis the asperity bifurcation process start to rework the fault plane just after its initial formation, meaning that the processes are active at similar stages in E1-E5.

The last faults to form are usually found in the near the vertical moveable wall towards the right, either as synthetic faults nucleating along the base of the plaster or as antithetic faults to accommodate the subsidence of the plaster cover along a flat base. The rightmost portion of the model is strained the most during the last stages of extension, and as the plaster stiffens the amount of strain to propagate through the cover towards the left is not enough for deformation.

The majority of both ductile and brittle deformation occurs in the hanging walls. The footwalls are generally deformed by means of ductile subsidence, however one of the most brittle experiments (E3) shows fracturing in throughout the model with varying densities

before any larger fault planes form. These fractures occur not only in an incipient fault zone, but also throughout the plaster cover (Fig. 15 and Fig. 16). They can represent the strain pattern as it propagates through the model from the moveable vertical wall and from the plaster cover subsidence.

A general sequence of deformation events for experiment E1-E5:
Models E3, E4 and E5 all formed one major fault plane, while models E1 and E2 formed several major fault planes. The processes forming a through-cutting master fault plane vary between the experiments. The deformation is dynamic and the displacement patterns change due to the changing strain-relationship imposed by increasing extension. Some differences in propagation patterns are also seen between the two profile planes in the same model, see discussion in section above on master fault evolution.

1. **Ductile deformation**: As extension starts, the induced strain spreads out into the medium to be accommodated by primarily ductile deformation.
2. **Fault initiation**: The first brittle structures form close to the vertical moveable wall in the lower corner of the model, nucleating on the interface between the basal baryte layer and the plaster cover.
3. **Growth and linkage of minor faults:** The first generation faults grow and link to form larger faults. The processes leading to a through-cutting major fault plane vary and determine the initial geometry of the fault plane. These processes are discussed in section 6.1.4.
4. **Formation and reworking of a major fault**: Generally, the newly formed through-cutting fault plane is at an early stage irregular. As extension continues the strain pattern changes and the original dip angle often is reduced as new fault plane trajectories are established by secondary processes such as asperity bifurcation and the formation of splay faults and horses. Footwall collapse is most active in the very short period as the first primitive master fault cut the surface and after some displacement has accumulated, which exposes the footwall. The master fault plane starts to accumulate a large amount of displacement only after a full length has been established, meaning that the plaster column is cut from base to surface. The smaller load along the exposed footwall may lead to larger strain propagation into the footwall, and subsequent faulting. Rotation and subsidence in the hanging wall increases with increasing displacement along the master fault plane and amount of strain imposed. Extensional duplexes are a reoccurring feature in the hanging wall near the master fault plane. These are often not preserved in it full size

at the end of the experiment as they are often cut through by new faults and/or smeared out along a fault plane. From this a repeating pattern of smoothing out irregularities, and the formation of new irregularities is seen.

5. Formation of multiple large fault planes generally a repeat of the processes listed in step 4. The formation of multiple master faults in the same model may be a concurrent process as in E2 or a sequential pattern as in E1.

6.1.7 Plaster to water ratio and the effect on the plaster rheology

The models of group 2 (E3, E4 and E5) are more viscous relative to group 1 (E1 and E2). A more viscous flow results in a relatively smaller strain propagation and/or a shorter ductile interval before the first formation of brittle structures. The plaster to water ratio for E1 is 1.33, while for E2, E3, E4 and E5 the ratio is 1.66. The plaster rheology is also very dependent on measurement accuracy, blending time and the water temperature. The plaster starts to set during the experiment, meaning that the plaster cover stiffens and will promote brittle deformation with increasing strain until a certain point where the plaster is too stiff to produce new structures. The cumulative number of visible faults was highest for E3 with 163 faults and the lowest for E1 with 16 faults, measured on one side in the model. The large cumulative number of faults produced in model E3 can be a measure of the brittle properties of the plaster cover, and the relatively small cumulative number in model E1 can be a measure of the ductile properties.

Ultimate tensile strength

The plaster to water ratio used in this thesis was 1.66 for all models, except for model E1 with a ratio of 1.33. According to the ultimate tensile strength plot in Fig. 4 (Coffin et al., 1964), the ultimate tensile strength of the solidified model E1 is ca. 375 psi, or 2.6 MPa. This indicates that the tensile strength during deformation is lower than 2.6MPa. For the rest of the experiments, the exact plaster to water ratio of 1.66 was tested by Coffin et al. (1964) but the sample was too stiff to produce proper results. The closest tested ratio was 1.54. A plaster to water ratio of 1.54 has an ultimate tensile strength of 500 psi, or 3.4 MPa. This indicates that the solidified models E2-E5 have ultimate tensile strengths of minimum 3.4 MPa.

6.1.8 Surface deformation

The extent of surface deformation is highly dependent on the plaster rheology, the nature of fault growth and strain rate. Most large faults produced in these models propagated upwards

to cut the surface after a fault plane was established, which reduces the influence of secondary structures on the hanging-wall surface.

Tension cracks are expected to form perpendicular to the direction of movement in materials that are brittle. As seen in the surface deformation of the models in this thesis, the orientation of the surface discontinuities varies. Along the surface of the middle parts of the plaster cover the discontinuities are perpendicular to the walls. In the areas close to the glass walls, the discontinuities typically form an acute angle to the sidewalls, pointing towards the direction of movement.

6.1.9 Displacement in the horizontal plane

According to Fossen et al. (1996) the largest and through-cutting faults accommodate 60-70% of the total extension, and the smaller faults accommodate 10-20%. Heave for the largest and through-cutting faults are measured for E1-E5. The models each accommodate a range within 43-90% of the total horizontal extension. The percentage horizontal displacement of the large faults is relatively smaller for models with a large cumulative number of smaller faults, indicating that the displacement is more distributed. For model E1, E2 and E4, which contains relatively fewer smaller faults, the largest and through-cutting fault accommodate 70-90% of the total horizontal extension. The models containing a larger cumulative number of faults accommodate 43-63% of the total extension in the throw of larger and through-cutting faults. This supports that the extension of a seismic section with a large number of sub-seismic faults may be underestimated, due to a wider distribution of displacement. A ductile component is present throughout the experiment, however the amount is difficult to quantify. The first brittle structures form after a ductile interval from 0-10% extension, which together with the ductile deformation throughout the experiment indicate an estimated ductile component of 10%. The remaining percentages of horizontal displacement is assumed to be accommodated by small-scale faulting, which is 27-37% and 10% for the models with a high and a low cumulative number of faults, respectively.

6.1.10 Displacement-length relationship along the fault plane

From the plots of maximum displacement along the fault plane with total fault length (D_{max}/L) it is concluded that the length and displacement accumulation is not a constant relationship, but a two-step process. A two-step model is consistent for the general fault population where the length accumulation dominates over displacement accumulation until the maximum length is achieved. When the maximum length is achieved, usually when the plaster column is cut

through, the fault plane accommodates strain by displacement along the slip-surface and the length accumulation is weak. The D/L plots for group 1 represent interacting fault planes, while group 2 represent models with only one master fault plane. All master faults formed by the linkage of minor fault planes. Most of the large fault planes nucleate at the base and propagates upwards. A delay in displacement accumulation may be a result of the coherent plaster cover near the surface. A through-cutting fault plane is already established when the surface is breached, which may promote a fast accumulation of displacement. According to Walsh et al. (2003) this pattern is more consistent with the isolated fault model than the coherent fault model. The displacement delay can be an elastic response up to a certain point. The previously isolated segments link up to form a segmented array, which in turn accumulate displacement and length to fit the displacement-length ratio of a single fault. A displacement accumulation delay is consistent with the isolated fault model where the displacement is not continuous. This is in contrast to the coherent fault model, where the displacement is continuous and displacement deficits are not found (Walsh et al., 2003).

Logarithmic diagrams are widely used for displacement-length relationships and include faults of several orders magnitude (Cowie et al., 1992). The plots generally represent displacement and length relationships for fault in map-view, as well-exposed vertical sections are limited in nature. Linear trends in a log-log plot represent a constant relationship of the two factors. A regular plot of the D-L values of the fault in this thesis are assumed to be a better representative for the data as the results fall into three orders of magnitude and their values can be read off the axes.

Maximum displacement-length ratio with increasing strain

Their line plots generally increase with increasing strain, but the slope also decreases gently with increasing strain to form a gently curved plot. This indicates that maximum displacement increases compared to the fault length with strain, and also that the D_{max}/L-slope is relatively lower towards the end of the experiment. These trends are consistent with the D_{max}/L-strain plots for both group 1 and 2.

6.1.11 Fault zone width

The width of the fault zone is dependent on the formation style of a through-cutting fault plane. The measured fault zone includes linking-damage structures and accommodation structure damage oriented sub-parallel to the main fault. This structural relationship is similar to those observed bounding fault zones in outcrops (Childs et al., 1997).

The fault damage zone for master faults in the models generally increased in thickness with increasing depth along the fault plane. The fault zone is often not wider than a few mm close to the surface. The maximum fault zone widths vary between 3 cm and 6 cm, measured perpendicular to the fault. This may be a result of larger volumes of plaster has passed each point with depth of the fault plane, and therefore experienced more structural complications and as a result, more asperity bifurcation and other accommodation structures and processes.

The formation processes vary from side A to B in a model, but the general trend is that the fault zone width was larger on the side on which the formation of brittle structures formed and developed first. The fault zone is also wider in the hanging wall compared to the footwall. Segment splaying and segment amalgamation may increase the width of the fault zone. The fault zone width is generally narrower on the side on which the through-cutting fault plane formed later. From this the conclusion is that the fault plane geometry in through the model is dependent on the structural style and timing of the structures. It also indicates that the fault plane interacts in three dimensions, and that the fault growth style is dependent on the primary structures.

Fault core is measured as the collective zone of collapsed structures, which has been heavily deformed along the fault plane. These zones increase towards the base, however their width is below 1 cm for all experiments. The fault core grows generally as a result of a changing fault trajectory, where the fault plane smears some plaster along the fault plane and then steps towards the right to leave sequential narrow zones of heavily deformed plaster in its footwall. The maximum fault core width for the experiments is; 4-5 mm for E3, 6-7 mm for E4 and 3-4 mm for E5.

Experimental set-up

The wide box set-up allows for the formation of more major fault planes compared to the narrow box set-up. Advantage of modelling in the wide box set-up is that a larger portion of the plaster cover is less affected by edge effects and a group of large master faults is generated. The advantage of modelling in the narrow box set-up is the closer view at the fault growth of one master plane and their associated minor structures without the intersection of other master faults.

6.1.12 Geometrically similar models

The plaster models presented in this thesis are made to simplify the natural deformation processes by testing the conditions needed to induce fault growth and generate structures similar to those found in nature. The accuracy of the models can only be measured by comparing models made under similar conditions, self-similarity, and comparing these similar models to structures formed and observed in nature. The plaster models are more simplified than accurate as the exact deformation patterns are difficult to match in seismic imaging and outcrops. However, numerical and experimental models of all kinds can rarely depict nature exactly but they are still valuable in the prediction of how structures will look in the nature (Stüwe et al., 2012).

Experiment E1 (Fig. 48A) is structurally similar to Run 1 presented in Fossen et al. (1996) shown in Fig. 48B. Run 1 and E1 both started with a relatively stiff and flat basal baryte layer, which forms a ramp as extension starts and generates geometrically similar end products. The first fault forms over the ramp geometry and cuts through the plaster column to form a main fault plane. Both Run 1 and E1 has a ramp-flat-ramp fault plane overlain by a graben and a horst structure. To the right of the horst structures are two right-dipping through-cutting fault planes and one left-dipping fault to the far right. Run 1 is extended to a $\beta \approx 1.48$, while E1 is extended to $\beta \approx 1.70$. The amount of small-scale structures formed is larger for run 1 than for E1, indicating that E1 presented in this thesis was relatively more ductile during the experiment than run 1. The experimental results are compared to a seismic section interpreted to be a basin-bounding normal fault with a ramp-flat-ramp geometry by Gibbs (2008). A horst and graben structure is interpreted to overlay the ramp-flat-ramp fault in the seismic section. This supports that is it possible to reproduce structurally similar models given similar initial conditions, which can be used to understand how structures will look in nature and is consistent with the conditions for a good model presented in Stüwe et al. (2012).

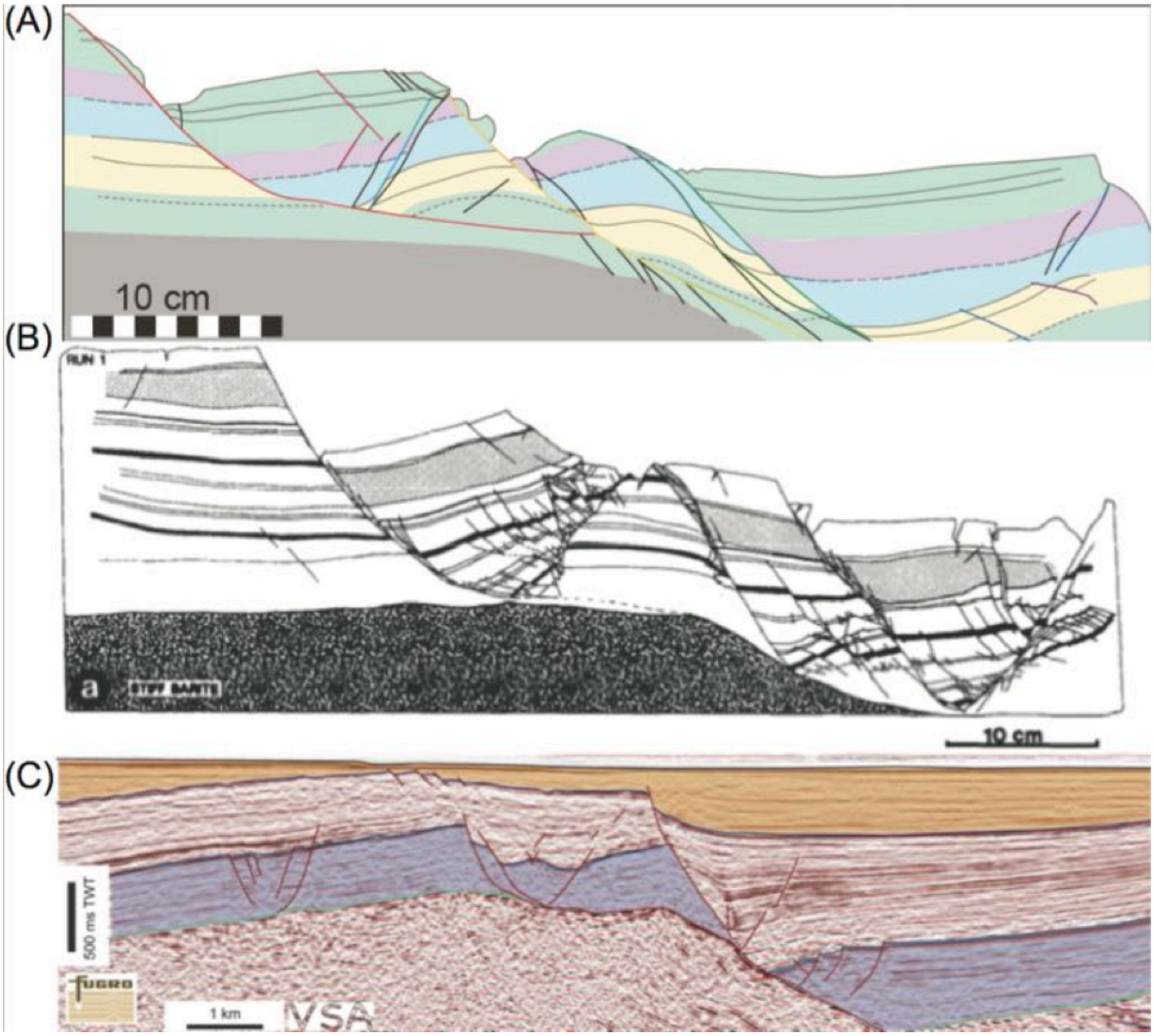

Fig. 48 (A) Final stage of model E1 presented in this thesis extended to β ≈1.70. (B) Run 1 extended to β ≈1.48. Modified from Fossen et al. (1996). (C) An interpretation of a seismic section in Inner Moray Firth, UK by Gibbs (2008) from the Virtual Seismic Atlas. The seismic section is interpreted to model a basin-bounding normal fault with a ramp-flat-ramp geometry.

The plaster models can be used as a reference for seismic interpretation of sub-seismic deformation when encountering complex sections. Two sub-parallel fault planes enclose a block of rock and plaster in Fig. 49A and B, respectively. The seismic section (Fig. 49A) is annotated and interpreted with normal faults and basin fill in the Inner Moray Firth, UK by Butler (2008) from the Virtual Seismic Atlas. The section is interpreted using the seismic data alone, without using external data or models. The section between the two leftmost large faults is described as a structurally complex zone, which probably contains sub-seismic deformation. The plaster model in (Fig. 49B) is a close-up of the fault zone in model E5 side A at β 1.18, where the accumulated displacement is ca. 5.5 cm. Between the larger faults in

(Fig. 49B), coloured red, dark green and pink, there are an array of synthetic splay faults, which intersect with the larger fault plane with a range of 60-80°.

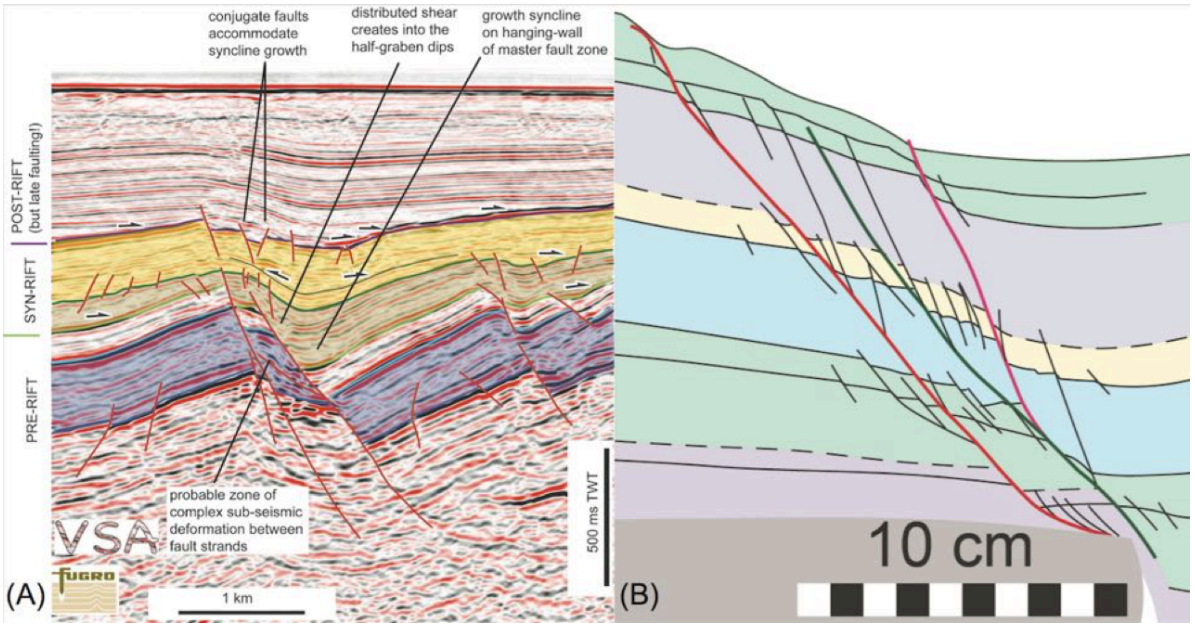

Fig. 49: (A) An interpretation of normal fault geometries and basin fill from the Inner Moray Firth, UK by Butler (2008) from the Virtual Seismic Atlas. (B) A section of an early stage of deformation (β 1.18) from model E5 side A (Fig. 23C).

Plaster modelling method

In reference to the criteria for a good model as described in section 3.2.1, the plaster modelling method provide models containing structures similar to those found in nature by means of a relatively simple experimental set-up. The range of structural orders visible in the models include the small scale structures that lead to the formation of a large through-cutting fault plane and associated deformation structures such as cross-cutting minor faults, lenses and fractures. The structures are compared to field examples, seismic sections and other plaster models that portray similar geometries, which indicate that the plaster models can be reproduced and aid the interpretation of structures in nature. The models are not unique, as both analogue and numerical modelling together with fieldwork is widely used, however the plaster models produce structures that are consistent with nature and can provide an additional source of reference for structural interpretation.

6.1.13 Errors

i. As a result of the experimental set-up, the lowermost 1.5 cm of the extended model is hidden behind the ruler and is not visible on photographs during the experiments. The base of the extended model is therefore not depicted in the model figures and explains why the lowermost marker stripes sometimes seems to move out of the figures. The hidden section also reduces the accuracy of section balancing using the photos shot during extension, as one of the initial criteria for balancing is a constant volume, or in this case area which is not fulfilled. Replacing either the basal plate within the box to a thicker plate, or replacing the two external plates with thinner plates can solve this.

ii. The experiments are set-up on a table, which is levelled manually using wedges of wood under the table feet and controlled using a spirit level.

iii. Water drainage from the model as it solidifies during the experiment may not be fast enough to avoid a ductile component.

iv. The extension rate is not constant. The friction between the moveable wall and the model box varies during the experiment, which leads to a more erratic extension rate.

v. The mixing rate, style and time of mixing affect the properties of the plaster cover. The plaster starts to set and becomes more viscous if mixed for a long time, however the viscosity is relatively lower and unpredictable if not all the plaster powder has been mixed and lumps are present.

vi. The basal layer geometry may not have the exact geometry as stated in the experiments. A horizontal layering may have a small dip angle, which is difficult to prevent when applying the basal layer manually within a narrow box. The level of the basal layer may appear to be different from side A to B, which may be a result of poor cleaning of the glass walls or uneven application.

vii. Dip angles and lengths are measured using the measure tool in adobe illustrator CC 2014 and compared to the model scale. The angular orientation of photos and figures are subject to errors from the level accuracy of the camera and the model set up. The photos from experiments are rotated to level the scale bar if needed, and is stated in the tables of model description in the results chapter.

6.2 Advantages and limitations for choosing plaster as the modelling material

Advantages:

- The plaster solidifies within an hour after an experiment and the model is preserved and studied in detail after the experiment, which is in contrast to sandbox models.
- The experimental set-up is relatively inexpensive, requires few materials and is easy to build and to modify if needed.
- Possibility to study the initial and deformed models, and the structural evolution.
- Plaster and baryte are promoted as modelling materials by Sales (1987) as they produce structures similar to the large scale structures formed in nature due to their viscoelastic properties, which allows the materials to shear as well as flow under deformation.
- The small and varying plaster grain size promotes narrow fault zones and fault planes.
- Coffin et al. (1964) presented plaster of Paris to be an effective material for dynamic testing for several reasons. Plaster of Paris has a high ratio of compressive to tensile strength. Low modulus of elasticity and low tensile strength require relatively small loads for brittle deformation to occur, which is suitable when deforming a medium under its own weight. Plaster of Paris has a linear stress-strain relationship for both compression and tension.

Limitations:

- The plaster is homogeneous without any internal layering. The models can therefore not be opened or cut to see internal deformation.
- The exact strain rate is difficult to determine as well as the stress field.
- The quality of the marker stripes and photos shot during the experiments largely control the level of detail and accuracy of fault plane trajectory and interactions. Fault planes are difficult to determine when they terminate between two marker stripes, unless some smear of blue acrylic paint marks the fault plane trajectory.
- The plaster is homogeneous and does not model the interactions of layers with varying competence, as one would expect to find in nature. The plaster is assumed to be homogeneous. Any water pressure gradient and density differences within the plaster cover may be present and is not accounted for in this thesis.
- The properties of the plaster cover changes during the experiment as it solidifies and the water from the mixture may not be drained out fast enough.

CHAPTER 7 Conclusions

The structural evolution of five analogue plaster models with varying basal layer, plaster cover properties, amount of strain and strain rate has been studied. The plaster modeling method generates deformation structures similar to those found in nature and can provide an additional source of reference for interpretation of seismic sections. Several master fault planes form and interact in models E1 and E2, while a single master fault with associated minor deformation form in models E3, E4 and E5. The models are compared to geometrically similar interpreted seismic sections. Structures formed in these plaster models are scale-independent as similar patterns are seen in both large- and small scale within the same model. This supports that is it possible to reproduce structurally similar models given similar initial conditions, which can be used to understand how structures will look in nature and is consistent with the conditions for a good model provided by Stüwe et al. (2012).

Plaster experiments model the geometric expression of a changing strain-pattern induced by extension and its effect on a homogeneous ductile-brittle medium. Important controls on the style of deformation are (1) Viscosity and homogeneity of the plaster mixture, (2) Extension rate and style (3) Geometry of the basement and basement properties.

The initial brittle structures form at the interface between the plaster cover and the basal baryte layer close to the moveable vertical wall. This is where the strain imposed is not distributed gradually, as the basal-cover layer interface forms a discontinuity in flow pattern. The initial brittle deformation occurs within 2-10% extension and a through-cutting fault plane forms within 23% extension, followed by secondary deformation. The footwalls show significantly less deformation than the hanging wall. The footwalls generally undergo subsidence and some movement towards the extension direction, whereas the hanging wall rotates and shears internally to generate faults with a variety of dip angles.

The structural complexity and deformation zone increases in width with increasing relief and dip angle of the basal layer as well as the level of fault plane irregularities.

Evolution of fault formation in the models presented in this thesis follows four trends: (i) Segment linkage of two fault planes propagating towards each other to form a horse with varying angular relationships as seen in E2A and E3B, (ii) footwall stepping growth of sequentially formation and linkage of sub-planar minor faults in a zone. These minor fault

may be oriented sub-parallel to the formed master fault as in E1 and E3A, or they may form at a relatively high angle in a wide zone to be cut at a higher angle as in E4, (iii) ramp-flat-ramp fault plane geometry on which the hanging wall may form grabens and horsts, and (iv) shifting fault plane trajectory where minor faults propagate upwards in a relatively wide zone to be cut through by an irregular fault plane with a shifting fault plane to form an anastomosing pattern and a number of horses and riders.

By plotting the maximum displacement with fault length a two-step process is apparent. The first stage is fault length accumulation up to a given maximum dependent on the accommodation space and fault geometry with a low displacement accumulation rate. The second stage is fault growth dominated by displacement accumulation, during which the fault length accumulation is relatively low. Plotting the maximum displacement-length ratio with increasing strain support the two-step model. Maximum displacement increases compared to the fault length with strain, and the plot also show that the D_{max}/L-slope is relatively lower towards the end of the experiment. A displacement accumulation delay is consistent with the isolated fault model where the displacement is not continuous. This is in contrast to the coherent fault model, where the displacement is continuous and displacement deficits are not found (Walsh et al., 2003).

By studying the fault growth patterns from three angles it is apparent that the larger faults are dependent on the style of the primary brittle structures and that the fault planes interacts in three dimensions. The collective horizontal displacement for large and through-cutting faults is dependent on the cumulative number of faults, which is again dependent of the ductile-brittle relationship. Relatively ductile sections with a small cumulative number of faults accommodate 70-90% of the total horizontal extension in the large and through-cutting fault planes. Relatively brittle sections tend to generate a large amount of smaller faults, leading to a more distributed horizontal displacement, where the larger faults accommodate 43-63% of the total horizontal extension. This distribution supports that the extension of a seismic section with a large number of sub-seismic faults may be underestimated, due to a wider distribution of displacement.

7.1 Further work

- Visualisation of deformation patterns and stepwise figures are also a useful tool for the basic and intuitive understanding of how the crust deforms an audience outside the geological community.
- By photographing the model at an oblique angle, including one profile plane and the surface in the same frame may easy the mapping and interpretation of faults in three dimensions. A wider box set-up, where the surface deformation is even less affected by edge effects in focus at the same time as the vertical sections could be of use for investigating structures related to fault-linkage and growth in three dimensions.
- The experimental set up is easy to modify and the hanging-wall deformation as a result of a given foot-wall geometry can easily be modelled by forming a rigid footwall covered with some friction-reducing material (rubber, oil, soft baryte) as in Lindanger et al. (2004). Pre-determined footwall geometry also enhances the controls on structural evolution by changes in strain-rate, plaster properties and extension factor.
- Model the extensional structures generated by having the basal layer follow the extensional movement, providing accommodation space at the back end of the basal layer. Such an experimental set-up is easily made from the original set-up used in this thesis by connecting a thin sheet or wooden plate to the moveable wall. The baryte basal layer used in the experiments presented in this thesis may inhibit the view through the glass walls as it moves. A very thin layer could be applied or an alternative basal layer could be used.
- Adding more marker stripes of acrylic paint mixed with water, perhaps alternating colours. Or stripes added with a wider brush. This may solve a problem regarding correlation between widely spaced marker stripes. The general propagation of faults is easier to follow in models with carbon powder marker stripes, which were applied with a wider brush but the details of fault propagation can be lost as the carbon powder often appears as aligned dots that is not easily identified as piercing points.
- Investigate the physical and mechanical properties of plaster of Paris in mixture with water
- Particle image velocimetry: In order to increase the numerical accuracy of the particle paths, the displacement field could be measured using particle image velocimetry

(PIV), which provide velocity vector measurements in a cross-section of a flow (Graveleau et al., 2012). Such studies for analogue plaster models have not been published.

- Constant extension rate
- The accuracy of plaster modelling can be tested by reducing the variability of the initial and boundary conditions to a minimum and look for similarities and differences in the plaster.
- Bilateral extension was modelled but not presented in this thesis. The experimental set-up is as presented in this thesis with the exception that both of the vertical short walls are pulled manually along the horizontal base for bilateral extension. The advantage of bilateral extension is the possibility to compare the structural outcome of two sub-experiments with the same initial conditions. Bilateral experiments provide an opportunity to see how deformation style varies by extension rate and style when using the same plaster mixture with the same properties. The movement of two wooden walls can be treated as two sub-experiments with same initial conditions equal starting point. The plaster mixture will have the same properties, but the extension rate and style of the two moveable walls are different.

References

Ackermann, et al. (2001). The geometric and statistical evolution of normal fault systems: an experimental study of the effects of mechanical layer thickness on scaling laws. *Journal of Structural Geology, 23*(11), 1803-1819. doi: http://dx.doi.org/10.1016/S0191-8141(01)00028-1

Atmaoui, et al. (2006). Initiation and development of pull-apart basins with Riedel shear mechanism: insights from scaled clay experiments. *International Journal of Earth Sciences, 95*(2), 225-238. doi: 10.1007/s00531-005-0030-1

Bastesen, & Braathen. (2010). Extensional faults in fine grained carbonates – analysis of fault core lithology and thickness–displacement relationships. *Journal of Structural Geology, 32*(11), 1609-1628. doi: http://dx.doi.org/10.1016/j.jsg.2010.09.008

Braathen, et al. (2004). Rock-slope failures in Norway; type, geometry, deformation mechanisms and stability. *Norw. J. Geol., 84*(1), 67-88.

Braathen, et al. (2009). Fault facies and its application to sandstone reservoirs. *AAPG bulletin, 93*(7), 891-917. doi: 10.1306/03230908116

Butler. (2008, 2008-02-19). Normal faults in the Inner Moray Firth - 2 annotated. from http://seismicatlas.org/entity?id=d60756c5-1a4f-41bf-a2e9-529b51e67792

Cadell. (1888). Experimental researches in mountain building. *Royal Society of Edinburgh Transactions, 35*, 337-360.

Caine, et al. (1996). Fault zone architecture and permeability structure. *Geology, 24*(11), 1025-1028. doi: 10.1130/0091-7613(1996)024<1025:fzaaps>2.3.co;2

Cartwright, et al. (1995). Fault growth by segment linkage: an explanation for scatter in maximum displacement and trace length data from the Canyonlands Grabens of SE Utah. *Journal of Structural Geology, 17*(9), 1319-1326. doi: http://dx.doi.org/10.1016/0191-8141(95)00033-A

Childs, et al. (2009). A geometric model of fault zone and fault rock thickness variations. *Journal of Structural Geology, 31*(2), 117-127. doi: http://dx.doi.org/10.1016/j.jsg.2008.08.009

Childs, et al. (1997). Complexity in fault zone structure and implications for fault seal prediction. In P. Møller-Pedersen & A. G. Koestler (Eds.), *Norwegian Petroleum Society Special Publications* (Vol. Volume 7, pp. 61-72): Elsevier.

Clifton, et al. (2000). Influence of rift obliquity on fault-population systematics: results of experimental clay models. *Journal of Structural Geology, 22*(10), 1491-1509. doi: http://dx.doi.org/10.1016/S0191-8141(00)00043-2

Cloos. (1955). Experimental analysis of fracture patterns. *Geol. SOC.Am. Bull, 66*, 241-256.

Coffin, & Kumar. (1964). *PLASTER OF PARIS AS A STATIC AND DYNAMIC MODEL TESTING MATERIAL*. U. S. AHMT RESEARCH OFFICE -DURHAM Box CM, Duke Station Durham, N. C.: Army Research Lab Research Triangle Park Nc Army Research, Office.

Cowie, & Scholz. (1992). Displacement-length scaling relationship for faults: data synthesis and discussion. *Journal of Structural Geology, 14*(10), 1149-1156. doi: http://dx.doi.org/10.1016/0191-8141(92)90066-6

Daubrée. (1879). Etudes synthétiques de géologie expérimentale pt. 1 (pp. 828). Paris.

Ehrlich, & Gabrielsen. (2004). The complexity of a ramp–flat–ramp fault and its effect on hanging-wall structuring: an example from the Njord oil field, offshore mid-Norway. *Petroleum Geoscience, 10*(4), 305-317. doi: 10.1144/1354-079303-585

Favre. (1878). Archives des Sciences Physiques et Naturelles. (No. 246).

Fisher, & Knipe. (2001). The permeability of faults within siliciclastic petroleum reservoirs of the North Sea and Norwegian Continental Shelf. *Marine and Petroleum Geology, 18*(10), 1063-1081. doi: http://dx.doi.org/10.1016/S0264-8172(01)00042-3

Fossen. (2010). *Structural Geology*. Cambridge: Cambridge eText.

Fossen, & Gabrielsen. (1996). Experimental modeling of extensional fault systems by use of plaster. *Journal of Structural Geology, 18*(5), 673-687. doi: http://dx.doi.org/10.1016/S0191-8141(96)80032-0

Fossen, & Hesthammer. (1998). Structural geology of the Gullfaks Field, northern North Sea. *Geological Society, London, Special Publications, 127*(1), 231-261. doi: 10.1144/gsl.sp.1998.127.01.16

Fossen, et al. (2000). Detachments and low-angle faults in the northern North Sea rift system. *Geological Society, London, Special Publications, 167*(1), 105-131. doi: 10.1144/gsl.sp.2000.167.01.06

Gabrielsen, & Clausen. (2001). Horses and duplexes in extensional regimes: A scale-modeling contribution. *Geological Society of America Memoirs, 193*, 207-220.

Gibbs. (1983). Balanced cross-section construction from seismic sections in areas of extensional tectonics. *Journal of Structural Geology, 5*(2), 153-160. doi: http://dx.doi.org/10.1016/0191-8141(83)90040-8

Gibbs. (1984). Structural evolution of extensional basin margins. *Journal of the Geological Society, 141*(4), 609-620. doi: 10.1144/gsjgs.141.4.0609

Gibbs. (2008, 2008-08-26). Fault interpretation by Alan Gibbs - v2. from http://goo.gl/QeOxhd

Graveleau, et al. (2012). Experimental modelling of orogenic wedges: A review. *Tectonophysics, 538–540*(0), 1-66. doi: http://dx.doi.org/10.1016/j.tecto.2012.01.027

Gupta, & Scholz. (2000). A model of normal fault interaction based on observations and theory. *Journal of Structural Geology, 22*(7), 865-879. doi: http://dx.doi.org/10.1016/S0191-8141(00)00011-0

Hall. (1815). On the Vertical Position and Convolutions of certain Strata, and their relation with Granite. *Transactions of the Royal Society of Edinburgh, 7*, 79-108.

Hubbert. (1937). Theory of scale models as applied to the study of geologic structures. *Geological Society of America Bulletin, 48*(10), 1459-1520. doi: 10.1130/gsab-48-1459

Koyi. (1997). ANALOGUE MODELLING: FROM A QUALITATIVE TO A QUANTITATIVE TECHNIQUE — A HISTORICAL OUTLINE. *Journal of Petroleum Geology, 20*(2), 223-238. doi: 10.1111/j.1747-5457.1997.tb00774.x

Lewry, & Williamson. (1994). The setting of gypsum plaster. *Journal of Materials Science, 29*(20), 5279-5284. doi: 10.1007/BF01171536

Lindanger, et al. (2004). Analogue (plaster) modelling and synthetic seismic representation hangingwall falt blocks above of ramp-flat ramp faults. *First Break, 22*(January 2004), 22-30.

Lister, et al. (1986). Detachment faulting and the evolution of passive continental margins. *Geology, 14*(3), 246-250. doi: 10.1130/0091-7613(1986)14<246:dfateo>2.0.co;2

Mansfield, & Cartwright. (2001). Fault growth by linkage: observations and implications from analogue models. *Journal of Structural Geology, 23*(5), 745-763. doi: http://dx.doi.org/10.1016/S0191-8141(00)00134-6

McClay. (1996). Recent advances in analogue modelling: uses in section interpretation and validation. *Geological Society, London, Special Publications, 99*(1), 201-225. doi: 10.1144/gsl.sp.1996.099.01.16

McClay, & Ellis. (1987). Analogue models of extensional fault geometries. *Geological Society, London, Special Publications, 28*(1), 109-125. doi: 10.1144/gsl.sp.1987.028.01.09

Mead. (1920). Notes on the Mechanics of Geologic Structures. *The Journal of Geology, 28*(6), 505-523. doi: 10.2307/30063760

Odinsen. (1992). *Modellering av normalforkastninger; analoge ekstensjons-gipsmodeller og balansering.* (Cand. scient.), Universitetet i Bergen, Unbublished, Universitetsbiblioteket i Bergen.

Osmundsen. (2002). Deep structure of the Mid Norway rifted margin. *Norsk Geologisk Tidsskrift, 82*, 205-224.

Pfaff. (1880). Der Mechanismus der Gebirgsbildung. Winter, C., Heidelberg., 143 pp.

Rotevatn, & Fossen. (2011). Simulating the effect of subseismic fault tails and process zones in a siliciclastic reservoir analogue: Implications for aquifer support and trap definition. *Marine and Petroleum Geology, 28*(9), 1648-1662. doi: http://dx.doi.org/10.1016/j.marpetgeo.2011.07.005

Rotevatn, & Fossen. (2012). Soft faults with hard tips: magnitude-order displacement gradient variations controlled by strain softening versus hardening; implications for fault scaling. *Journal of the Geological Society, 169*(2), 123-126. doi: 10.1144/0016-76492011-108

Saint-Gobain. (2015). Molda 3 Normal. *Material Safety Data Sheets of Saint-Gobain.* Retrieved 2015/03/19

Sales. (1987). TECTONIC MODELS,Tectonic models *Structural Geology and Tectonics* (pp. 785-794): Springer Berlin Heidelberg.

Schlische, et al. (1996). Geometry and scaling relations of a population of very small rift-related normal faults. *Geology, 24*(8), 683-686. doi: 10.1130/0091-7613(1996)024<0683:gasroa>2.3.co;2

Stüwe. (2007). *Geodynamics of the lithosphere: An introduction*: Springer.

Stüwe, & Drescher. (2012). How to write a manuscript for a journal. *Mitteilungen des naturwissenschaftlichen Vereines für Steiermark, 142*, 117-144.

Walsh, et al. (2003). Formation of segmented normal faults: a 3-D perspective. *Journal of Structural Geology, 25*(8), 1251-1262. doi: http://dx.doi.org/10.1016/S0191-8141(02)00161-X

Willis. (1891). ... *The Mechanics of Appalachian Structure*: U.S. Government Printing Office.

Withjack, et al. (1995). Normal faults and their hanging-wall deformation: an experimental study. *AAPG bulletin, 79*(1), 1-17.

Yielding, et al. (1991). Seismic reflections from normal faults in the northern North Sea. *Geological Society, London, Special Publications, 56*(1), 79-89. doi: 10.1144/gsl.sp.1991.056.01.06

Appendix A: Definitions

Geological terms specifically used in this thesis are defined in this section. For further reference, a more detailed description of structural geological terms and processes are provided in Fossen (2010).

Faults

Faults are planar fractures in rocks on which displacement has occurred. The fault plane geometry may vary and is usually planar or curved. The rocks on each side of a fault plane are displaced relative to each other in an up-dip manner for reverse faults, down-dip for normal faults and along strike for strike-slip faults. Faults occur in the upper and brittle crust.

Normal faults

When extensional faults form, the hanging wall moves down relative to the footwall. According to the Andersonian stress state, the fracture forms at a 60˚ angle, while faults in nature have a more variable dip. **Listric** faults, or **detachment** faults, have a steep dip near the surface and flatten out downwards. The hanging wall may rotate or slide along the fault plane, or be transported more rigidly along the flatter base.

A **master** fault is the largest fault in an area, while other dominant faults are called master faults and smaller faults are called minor faults. The minor faults are divided in synthetic and antithetic faults. **Synthetic** faults have he same dip-direction as the main fault. The dip-direction of **antithetic** faults is opposite to the main fault.

The rigid domino model

Rotated fault blocks are often a dominant configuration in a rifted upper crust. The blocks in a rigid domino model rotates at the same rate and at the same time, ending up with the same dip angle and a constant offset along the fault. The block has not undergone internal shear and the layers within a block are planar (Fossen, 2010). The model of rigid rotation of blocks creates an issue of space, which can be solved by introducing a listric fault, on each side and along the base of rotated blocks. Two arrays of rotated fault blocks dipping towards each other would need a graben where the two orientations intersect to solve a space problem.

The soft domino model

Rotated fault blocks in nature have layers of varying competence, which leads to a variation of deformation patterns and geometries. The soft domino model allows for internal strain in the rotated fault blocks as well as different fault geometries, a varying displacement distribution and folding of layers.

Piercing point

Piercings points are elements on each side of a fault plane, which was originally connected or juxtaposed before deformation. The displacement and apparent offset can be found by identifying piercing points, which in turn can be used for the interpretation and restoration of a deformed area. Linear structures like a fold axis or planar layering of visually different rock types provide good conditions for an accurate measurement, as their geometry is predictable.

Fractures

Fractures are discontinuities in a medium with a very small displacement parallel to the fracture surface. Their geometry is planar or sub-planar. Tensile fractures may form due to tensional stress in a rock and are also called joints.

Horst and grabens

A single normal fault may form a half graben, which is more common in the crust. When two normal faults form with different dip-directions, they may form a horst or a graben. A horst is formed when two normal faults dip away from each other, while a graben is formed when the fault planes dip towards each other.

Fault core

The fault core of a fault is where most displacement is accommodated. In nature, the core may consist of strongly deformed rocks as well as lenses of rock.

Damage zone

The damage zone consists of brittle deformed rocks surrounding the fault core. The width of both the damage zone and fault core increase with increasing displacement, but this complicated relationship is difficult to predict. Statistically the width of a damage zone is 1/100 of the faults length for faults with displacement up to 100 m (Fossen, 2010).

Process zone

When the crust is subjected to extensional stresses, micro fractures start to form in a zone called the process zone. The process zone in non-porous rock grinds the grains, weakens the rock and increases the porosity by fractures. Porous rocks allow the grains to rotate and slide to a certain point, where the grains break and may form deformation bands. This is called strain hardening and may reduce porosity. Deformation bands form adjacent to the fault, usually in the same orientation as the fault plane.

If the tips of these micro fractures connect, a fault plane may form. The maximum displacement of a normal fault is usually found at the centre of the fault plane, decreasing towards the tip-lines. The dip of the fault plane may vary due to the complex linkage of fault segments in map view and in profile. Listric faults flatten out down-dip and vary from high angle near the surface to low angle at depth. These faults may create accommodate space for rotation of fault blocks. Less energy is needed for reactivation of joints or pre-existing fault planes, resulting in a narrower damage zone. The angle of the fault plane will be a result of the pre-existing plane or weakness zone.

Displacement accumulates by stable sliding, aseismic slip or earthquakes. Porous sedimentary rocks promote stable sliding, while non-porous rocks promote stick-slip. Earthquakes are a sudden release of tension as a result of friction along a fault plane. This build-up and release pattern is called stick-slip. Friction as a result of irregularities along the fault plane inhibits plate motion and lead to a build up of stress, where the tension is partially released during rupture.

Drag is the deflection of layers surrounding a fault plane. Drag in large scale may appear as folding as a result of ductile deformation, while on a smaller scale the drag zone may be a zone of many minor faults.

Relay ramps

Relay ramps may form when the tips of two faults propagate sub-parallel to each other. The faults accumulate displacement at their respective fault planes, which decreases towards the tips, leaving a coherent slab of rock between them. When sufficient tip propagation and displacement accumulates, the relay ramp breaks.

Horse and riders

Fault planes with a ramp-flat-ramp geometry promote the formation of riders and horses in the hanging wall. Riders have free tips upwards and may reach the surface, while horses are limited by a floor fault and a roof fault. A succession of riders is collectively called an imbrication fan, while a succession of horses form a lens and is collectively called an extensional duplex (Fossen, 2010).

Formation of extensional duplexes

There are two main groups of fault patterns, the primary processes describe the formation of a fault plane and the secondary processes describe the development of the fault zone in reference to an existing fault plane. The following six processes describe the mechanisms for the development of extensional duplexes.

Tip-line coalescence is a primary structure and is the direct linkage of two parallel or sub-parallel fault planes propagating towards each other. The result is a fault plane with varying dip angle, with ramps and flats.

Segment linkage is a primary structure and involves the overlapping of two near-by sub-parallel faults. Horses are formed by segment linkage of a series of minor fault branches, which tips interact and grow together in a shared stress area (Gabrielsen et al., 2001).

Tip-line bifurcation may develop if two sub-parallel fault strands originating from the same fault propagate irregularly. The irregular propagation may be a result of heterogeneities in the host rock, a variation of stress fields or reorientation of the stress field (Walsh et al., 2003).

Asperity bifurcation is a secondary process, which removes and smoothens irregularities along a fault plane by generating a new slip surface.

Segment splaying is a secondary process, which may contribute to widening the fault zone. Minor fault strands initiate at the fault plane of a master fault, propagate synthetically and may link up to form a series of splay horses.

Segment amalgamation is a secondary process where minor faults propagate downwards and grow together with a master fault. These structures are associated with the damage zone or high-strain zone of a master fault or synthetic adjustment structures (Gabrielsen et al., 2001).

Appendix B: Additional results

Plots and figures not included in the results chapter are presented in this section.

Cumulative plot of faults during extension

The cumulative number of faults for E1, E2, E3, E4 and E5 are plotted in Fig. B 1. All models generated an average maximum of 36 faults, with E3 as an outlier of around 163 faults generated in total.

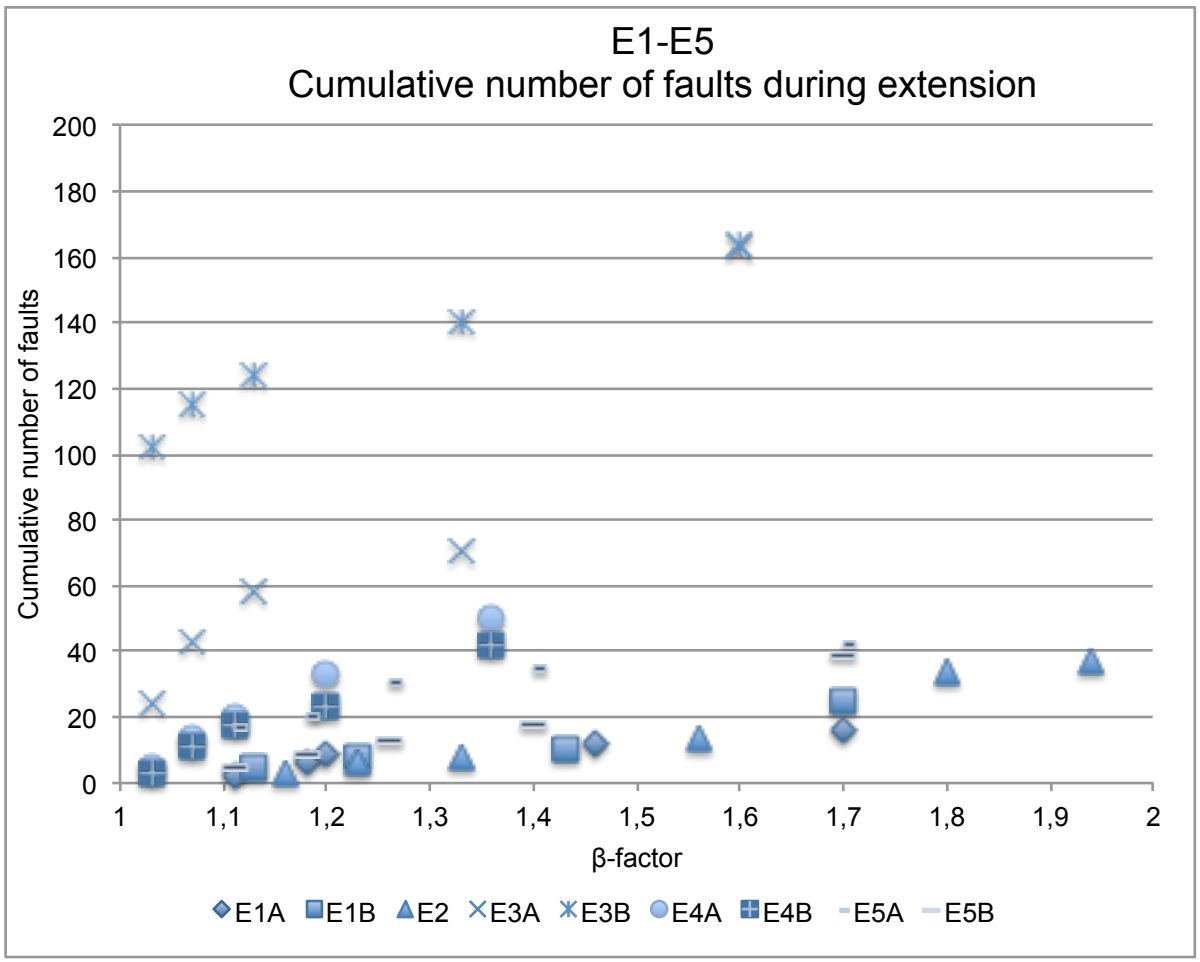

Fig. B 1: Cumulative number of faults plotted against the amount of strain during experiments E1, E2, E3, E4 and E5.

Plots of fault lengths of master faults with increasing strain

The fault length of master faults is plotted against an increasing strain, or β-factor. The axes are scaled equally for easy comparison of the plots. The corresponding fault strands on side A and B are plotted in the same plot. Note that as the fault strands are numbered after

chronological time of formation for each vertical profile plane, hence numbers do not always correlate between corresponding A and B sides and is specified for each plot.

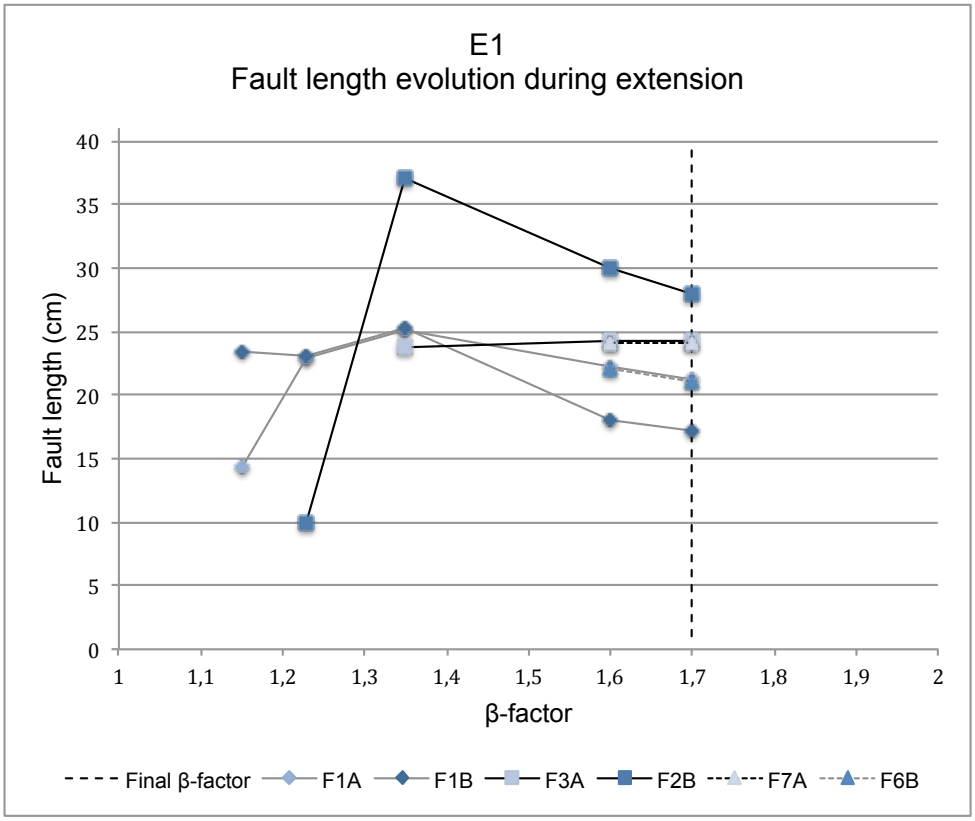

Fig. B 2: The evolution of fault length during extension for E1. F1A and F1B are fault strands that correlate to the same master fault, as do F3A with F2B and F7A with F6B.

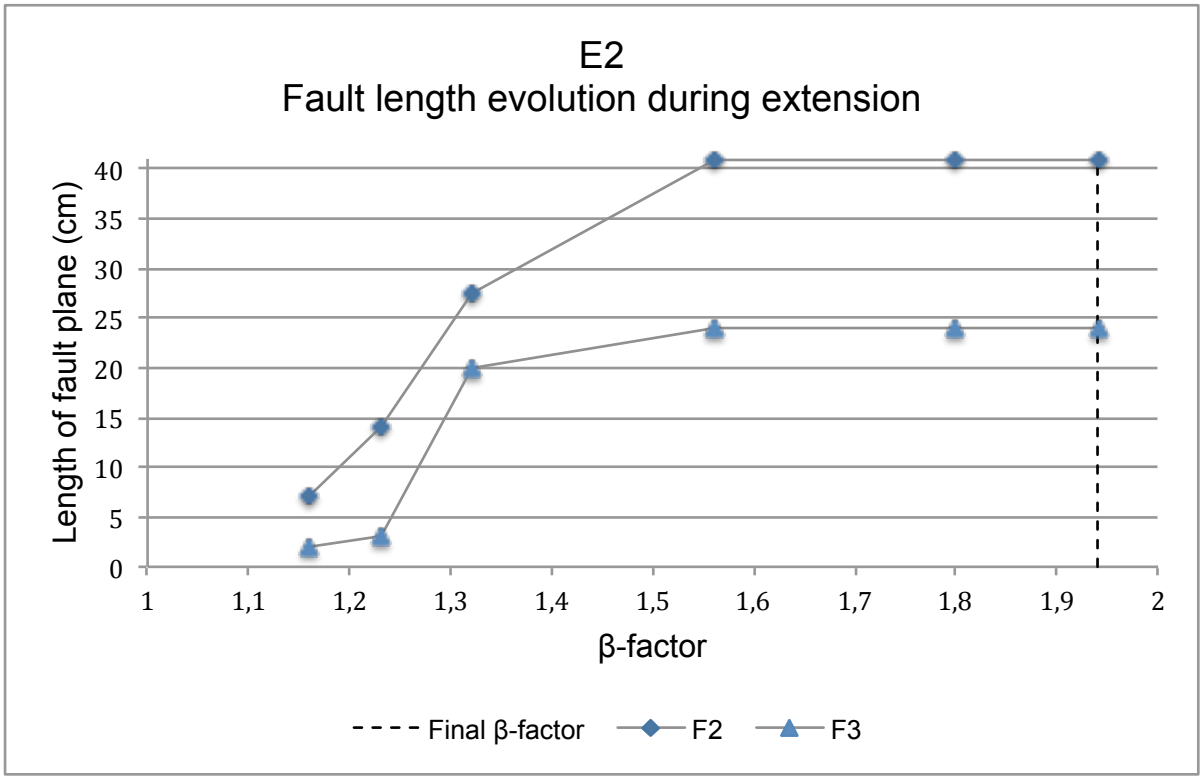

Fig. B 3: The evolution of fault length during extension for E2. Strain (β-factor) plotted against the length (cm) of the two master right-dipping fault planes F2 and F3 in model E2.

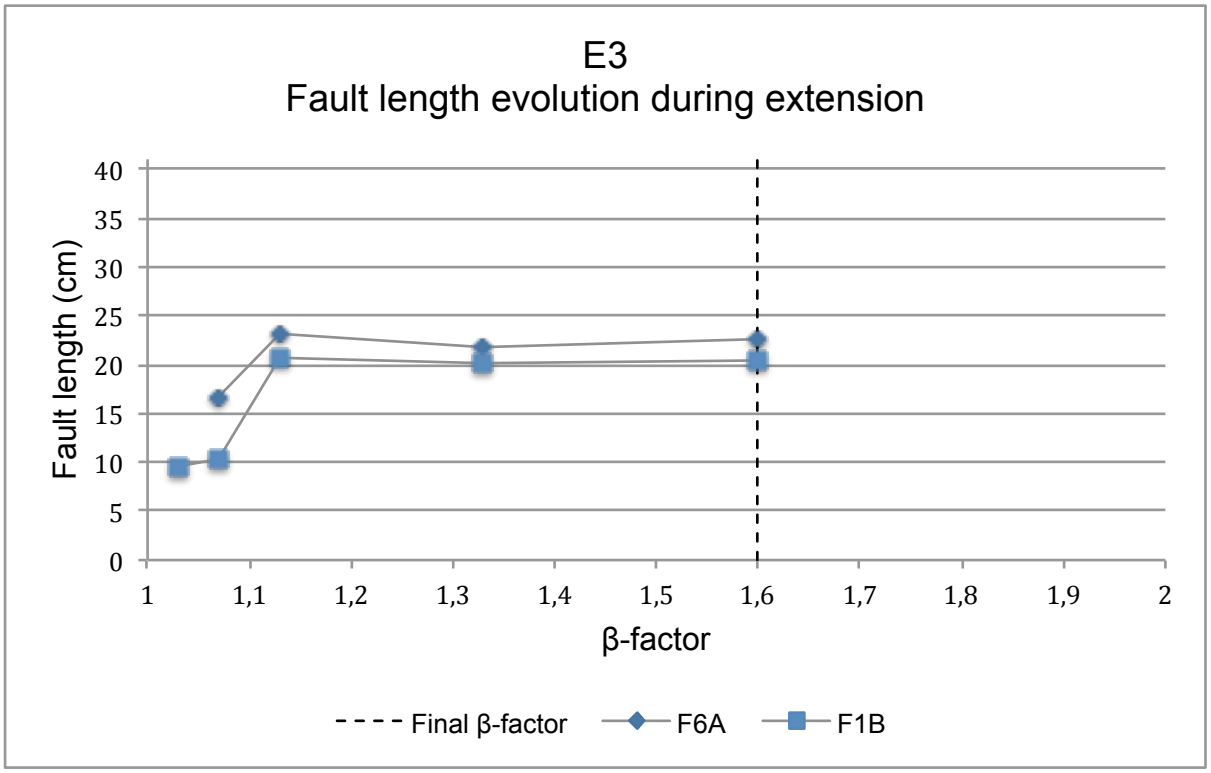

Fig. B 4: The evolution of fault length during extension for E3. F6A and F1B are fault strands that correlate to the same master fault.

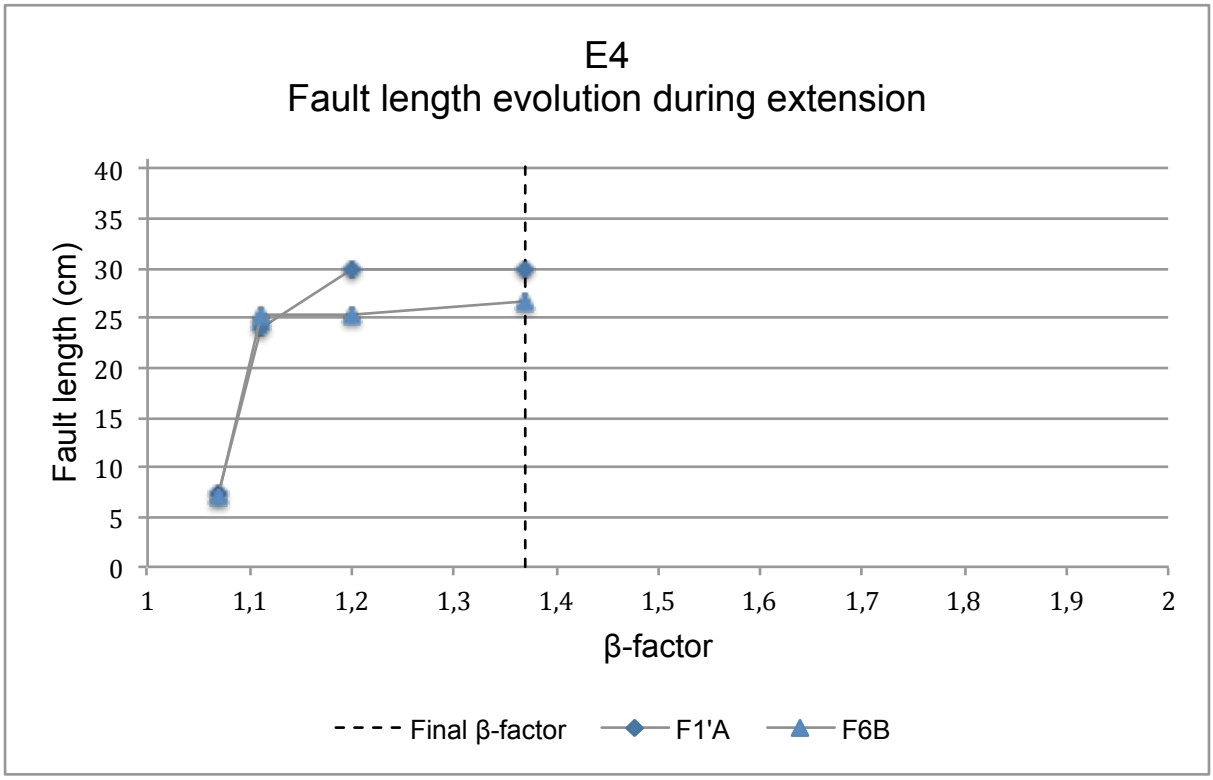

Fig. B 5: The evolution of fault length during extension in model E4. F1'A and F6B are fault strands corresponding to the same through-cutting master fault plane.

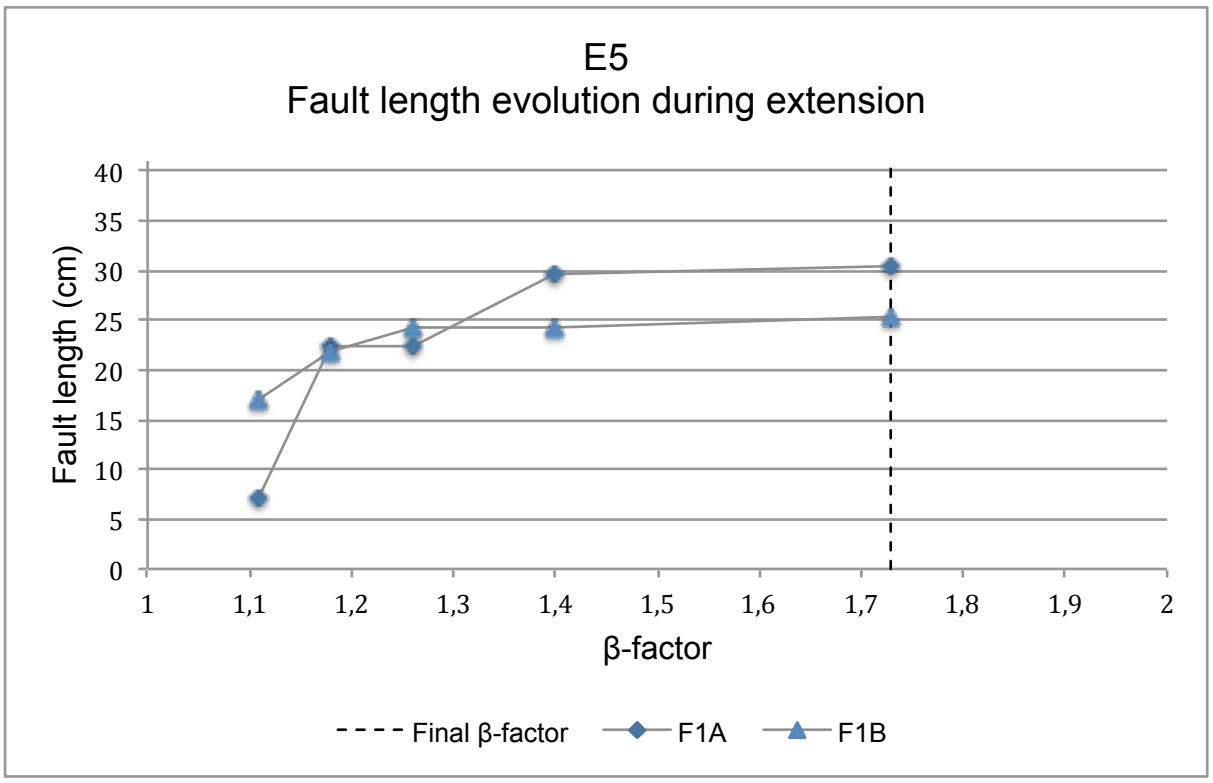

Fig. B 6: The evolution of fault length during extension in model E5. F1A and F1B are fault strands corresponding to the same through-cutting master fault plane.

Plots of accumulated displacement at surface level with increasing strain

The accumulated displacement of the three main normal faults in E1 side A and B is plotted against the β-factor, or accumulated amount of displacement. F1A and F1B are fault strands that correlate to the same master fault, as do F3A with F2B and F7A with F6B.

F1 on side A and B follow a similar displacement accumulation until β 1.35, from here the pattern is similar but slightly less displacement is accumulated on side A compared to side B. The two fault stands end up with a similar total amount of displacement of 8 cm and 8,5 cm for A and B, respectively.

F3A and F2B is two fault strands of the same master fault. They have the same amount of displacement at β 1.35. The fault stands follow the same trend, while the accumulation is relatively lower for side A than side B. The total amount of displacement accumulated is 5 cm and 6 cm for side A and B, respectively.

F7A and F6B correlate to the same master fault, which form at a late stage of the experiment above the ramp geometry. The two strands show different amounts of displacement, at 1.60 the total amount is larger for side B at 3,5 compared to 2 cm for side A. When the experiment ended, the maximum had shifted to side A with 5 cm accumulated compared to 4 cm for side B.

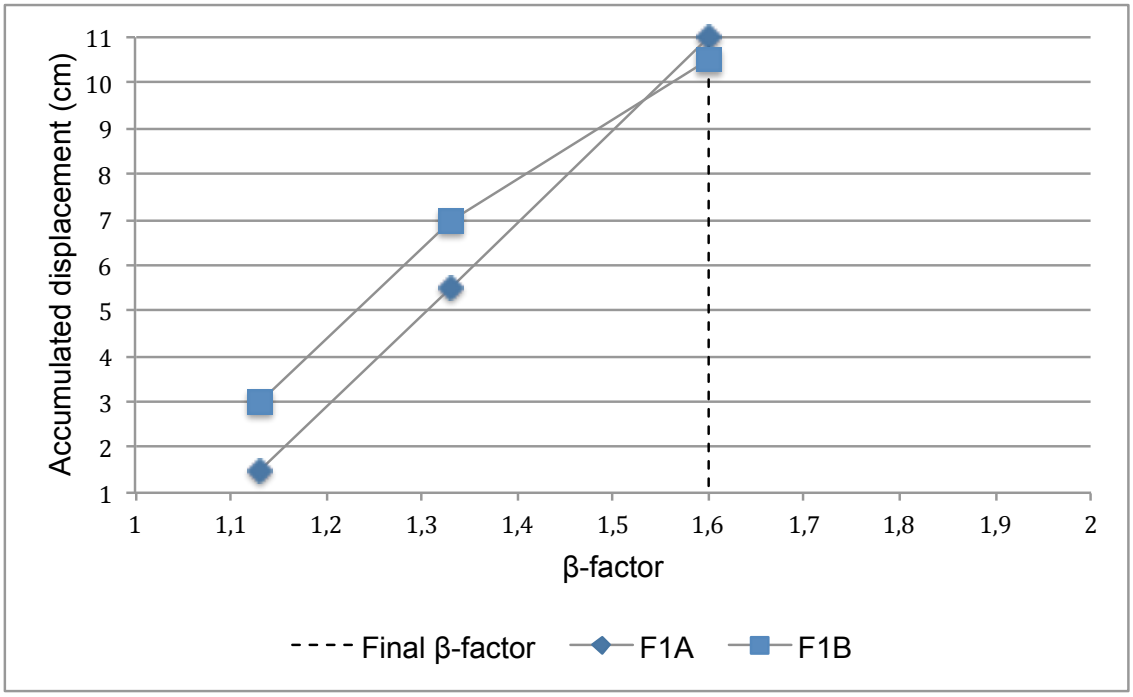

Fig. B 7: The accumulated surface displacement of the main normal fault in E3 side A and B is plotted against the β-factor, or accumulated amount of displacement.

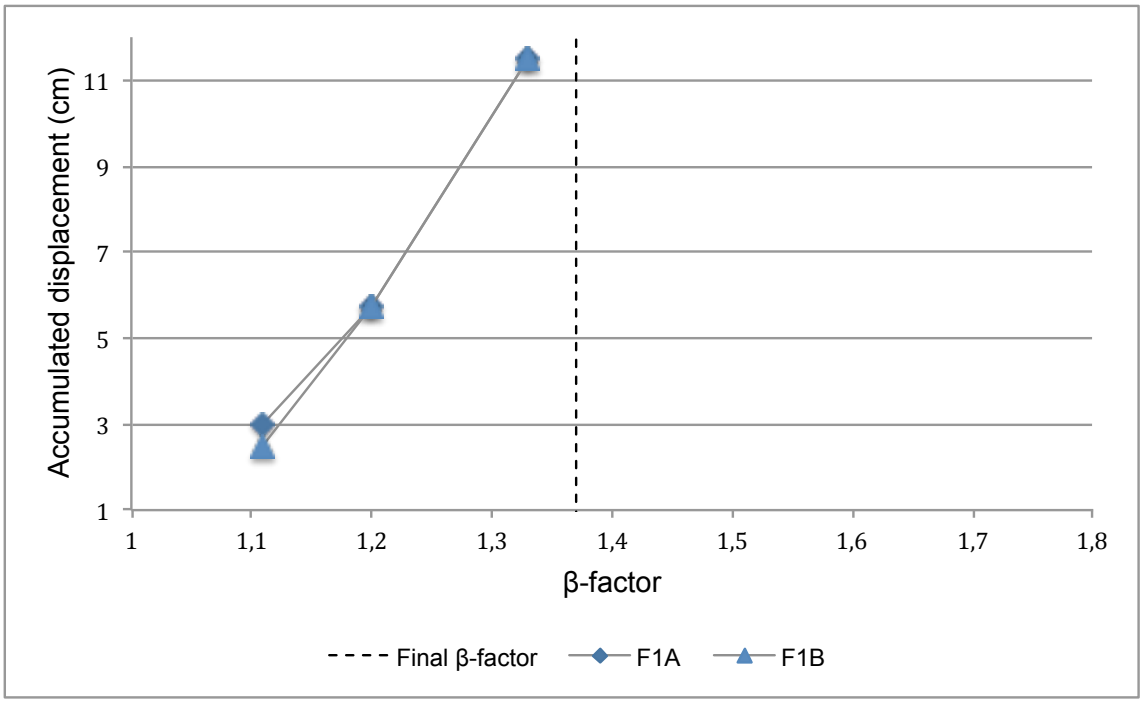

Fig. B 8: The accumulated surface displacement of the main normal fault in E4 side A and B is plotted against the β-factor. The two fault profiles F1A and F1B correspond to the same master fault. The amount of displacement accumulated varies by 0.5 cm at β 1.11, where the displacement is 3 cm for F1A and 2,5 cm for F1B. The displacement is the same for both fault profiles at β 1.20 and 1.33.

Plots of maximum displacement of master faults with total fault plane length

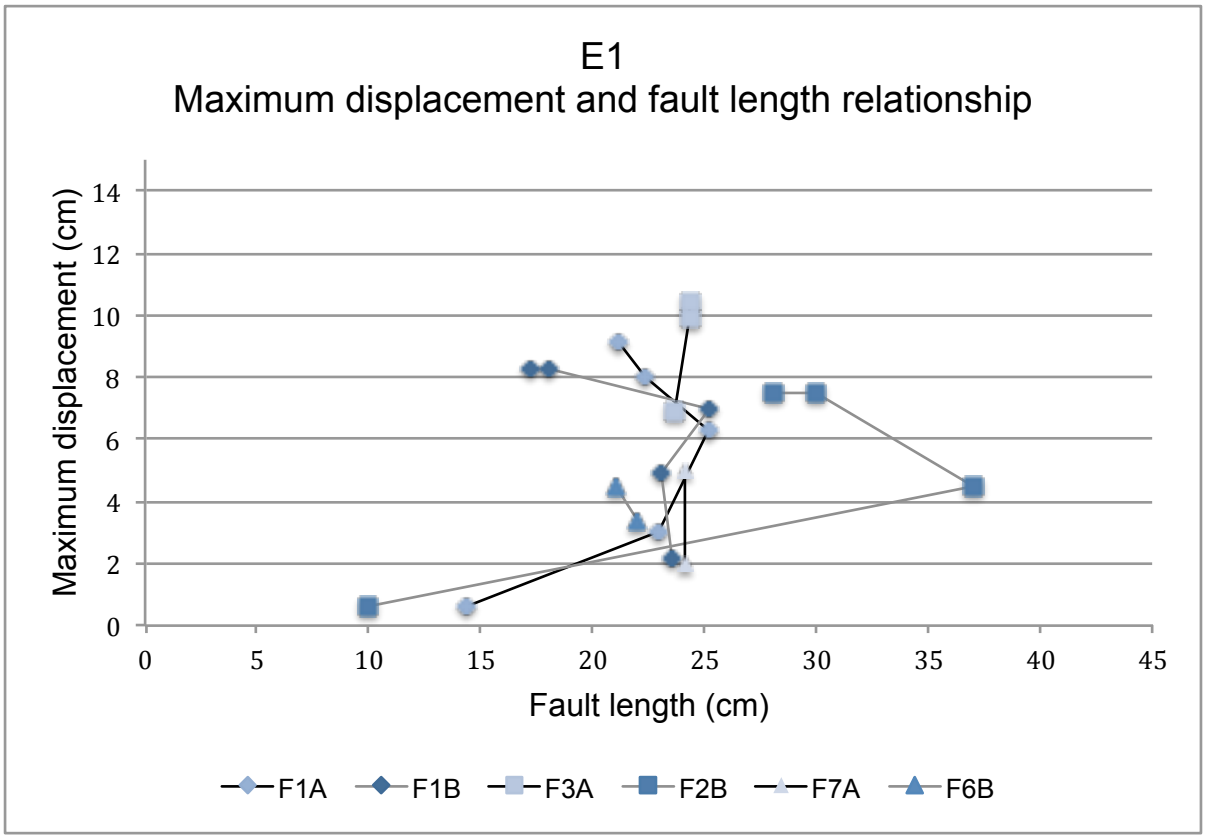

Fig. B 9: The evolution of the maximum displacement to length during extension. F1A and F1B are fault strands that correlate to the same master fault, as do F3A with F2B and F7A with F6B. Some fault planes are cut by younger faults and decrease in length.

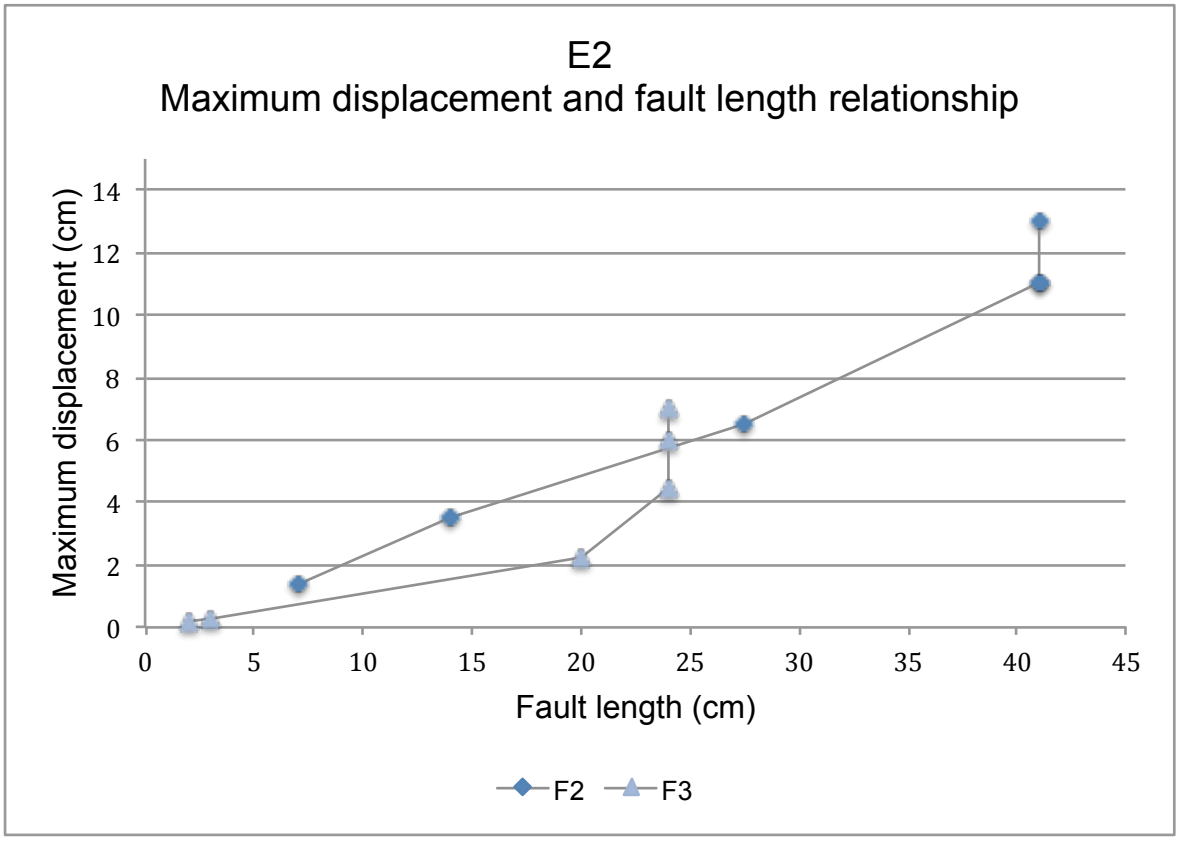

Fig. B 10: The evolution of the maximum displacement to length during extension. F2 and F3 are two different master normal faults. Photos available are limited to side A of model E2 and is described in this thesis.

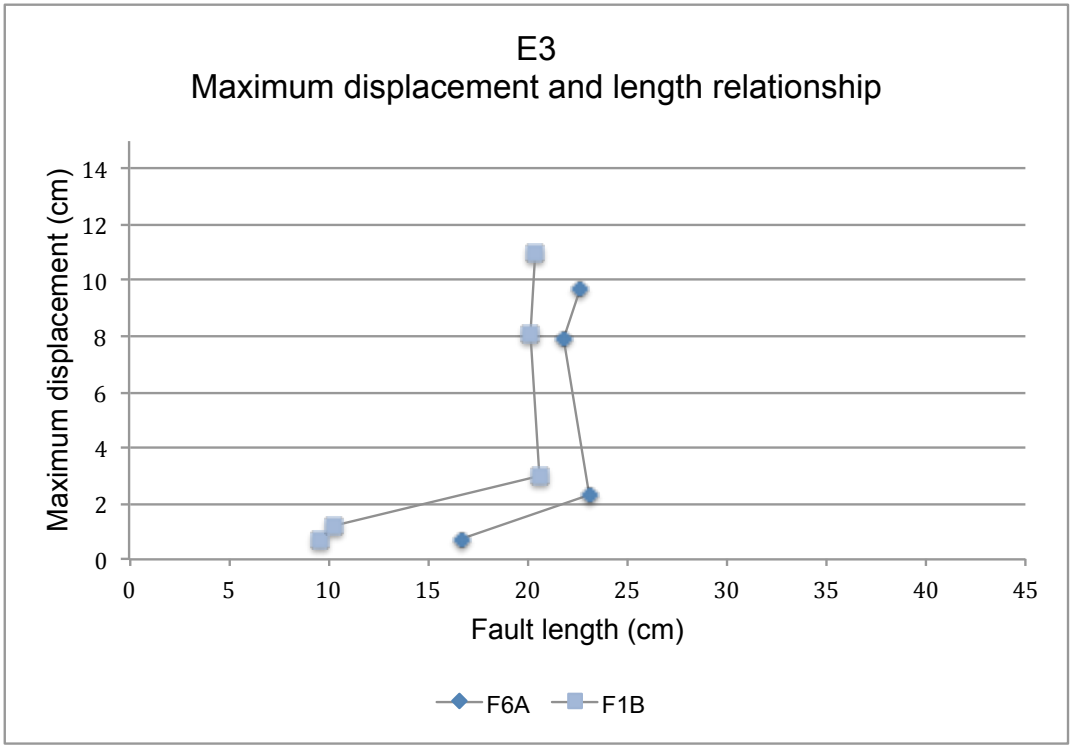

Fig. B 11: The evolution of the maximum displacement to length during extension. F6A and F1A correspond to the largest fault on each profile plane.

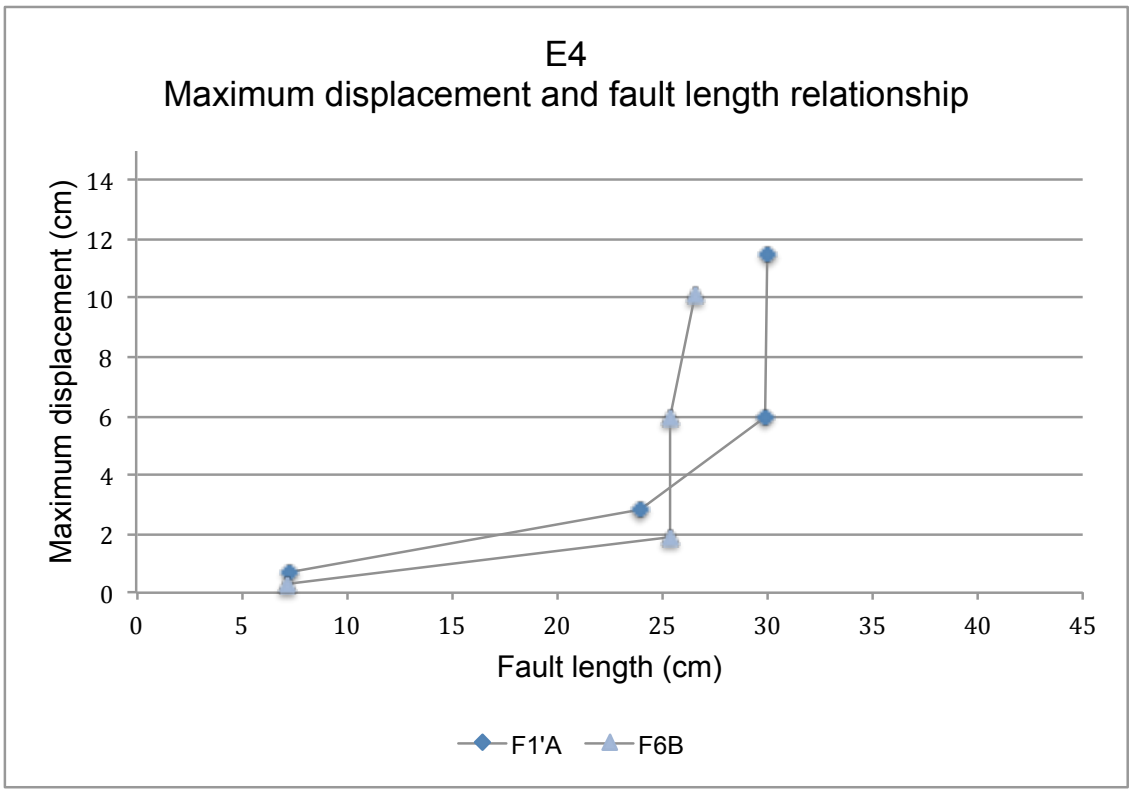

Fig. B 12: The evolution of the maximum displacement to length during extension. Faults F1'A and F6B corresponds to the same through-cutting master fault plane on sides A and B, respectively.

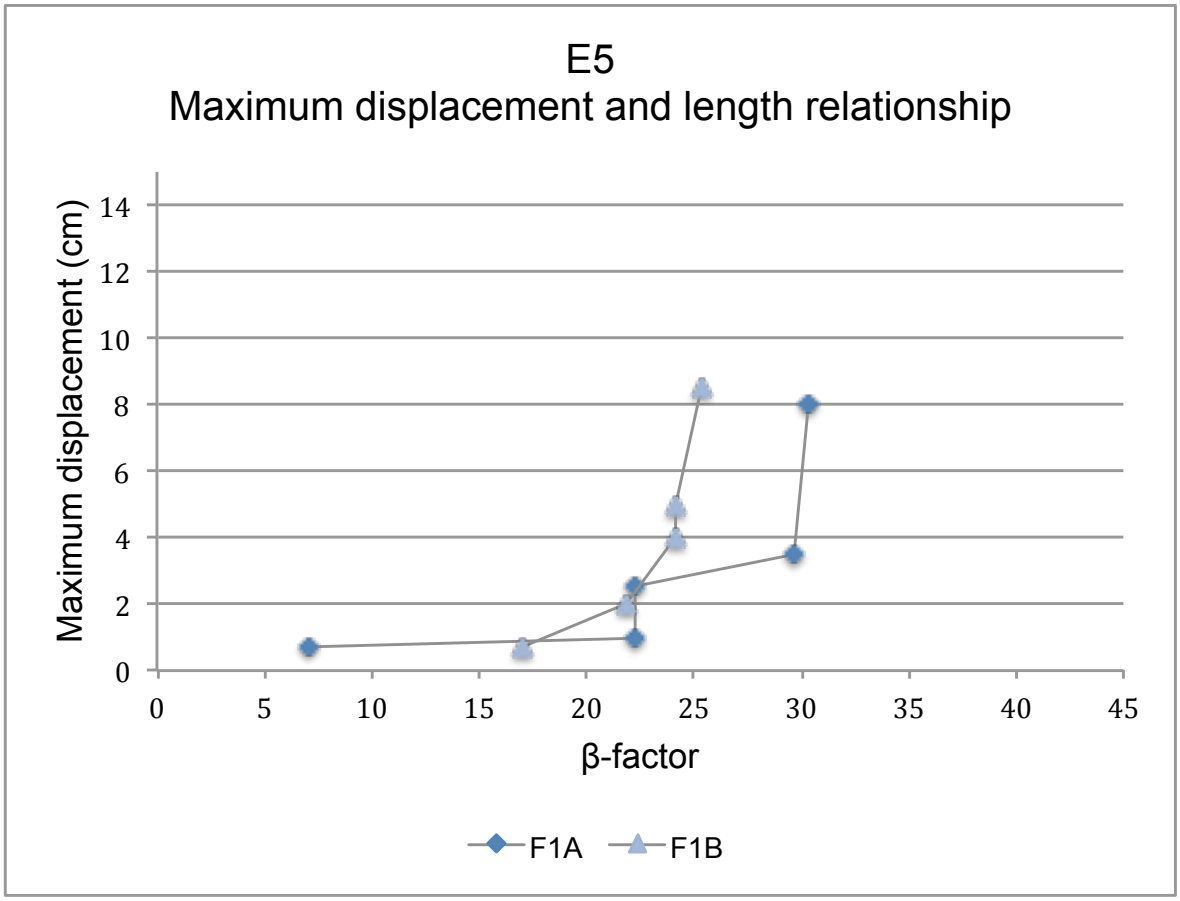

Fig. B 13: The maximum displacement of the main normal fault in E5 side A and B is plotted against the β-factor, or the amount of strain. E5 ended at β 1.73 and is indicated in the graph by a dashed line. The two fault profiles F1A and F1B correspond to the same master fault. The amount of displacement accumulated in cm varies between the two sides, while the accumulation rate is similar. Most displacement is accumulated along F1B at 10 cm, while F1B has accommodated 8 cm of displacement. (*fault F3 on side A accommodate 7 cm of displacement, but is not prominent on side B*)

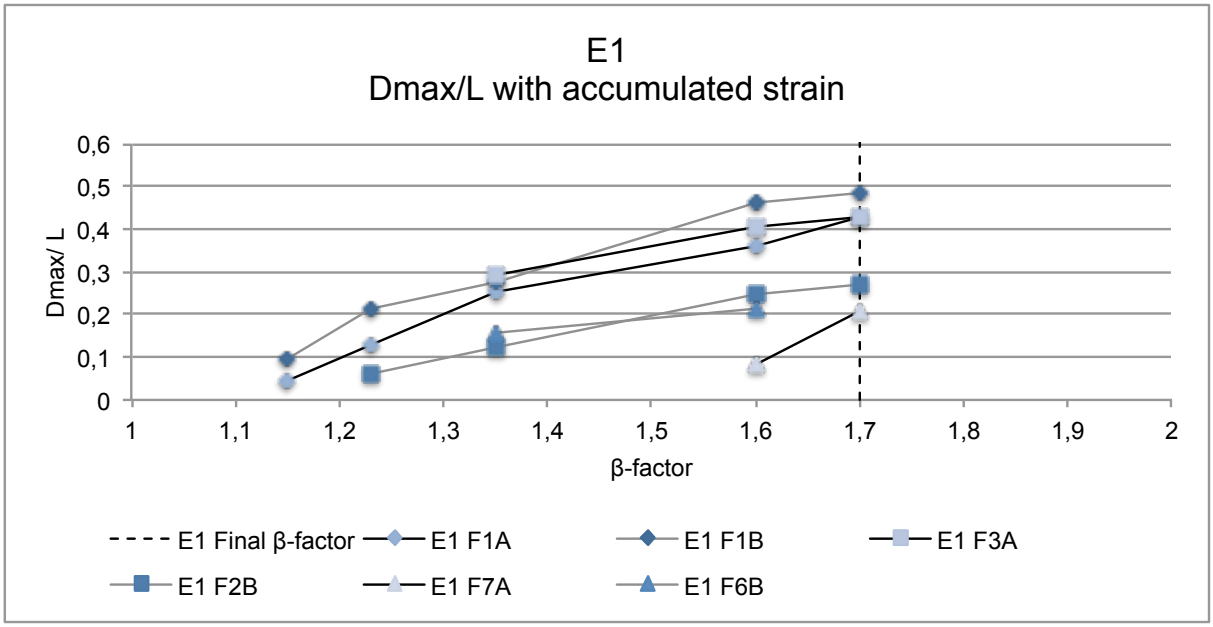

Fig. B 14: Maximum displacement (D_{max}) and length (L) ratio plotted against the accumulated strain (β-factor) for model E1

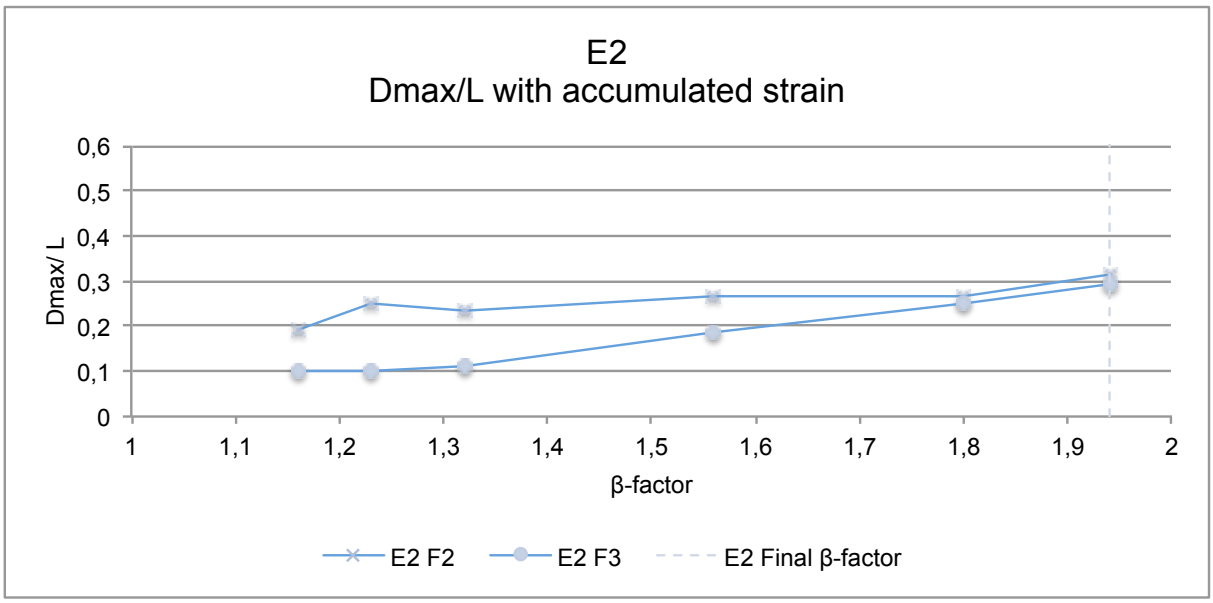

Fig. B 15: Maximum displacement (D_{max}) and length (L) ratio plotted against the accumulated strain (β-factor) for model E

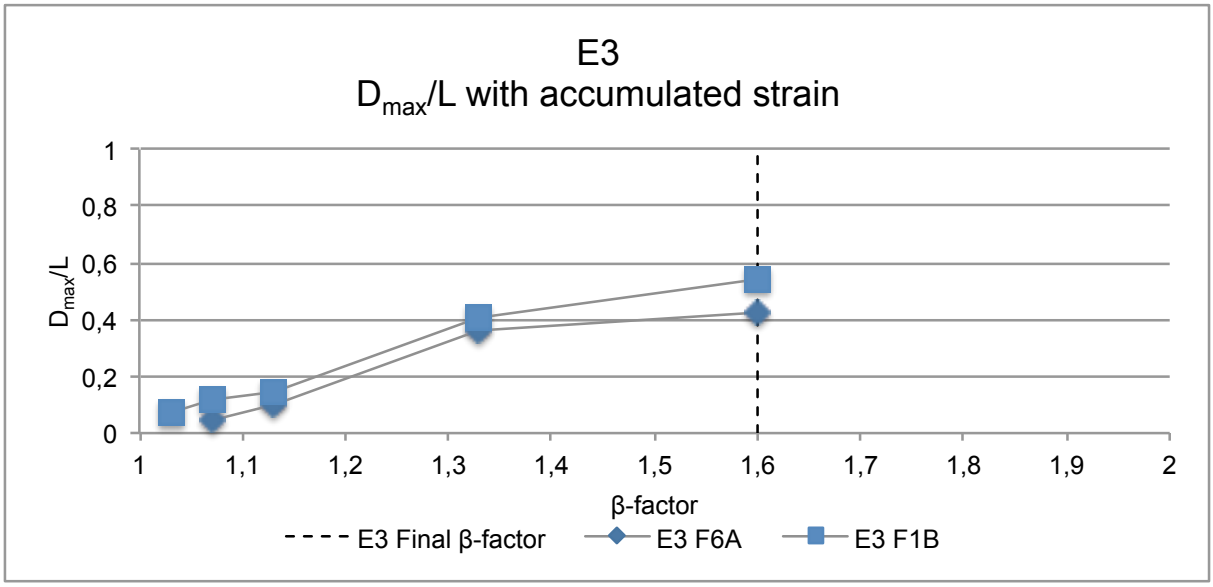

Fig. B 16: Maximum displacement (D_{max}) and length (L) ratio plotted against the accumulated strain (β-factor) for model E3.

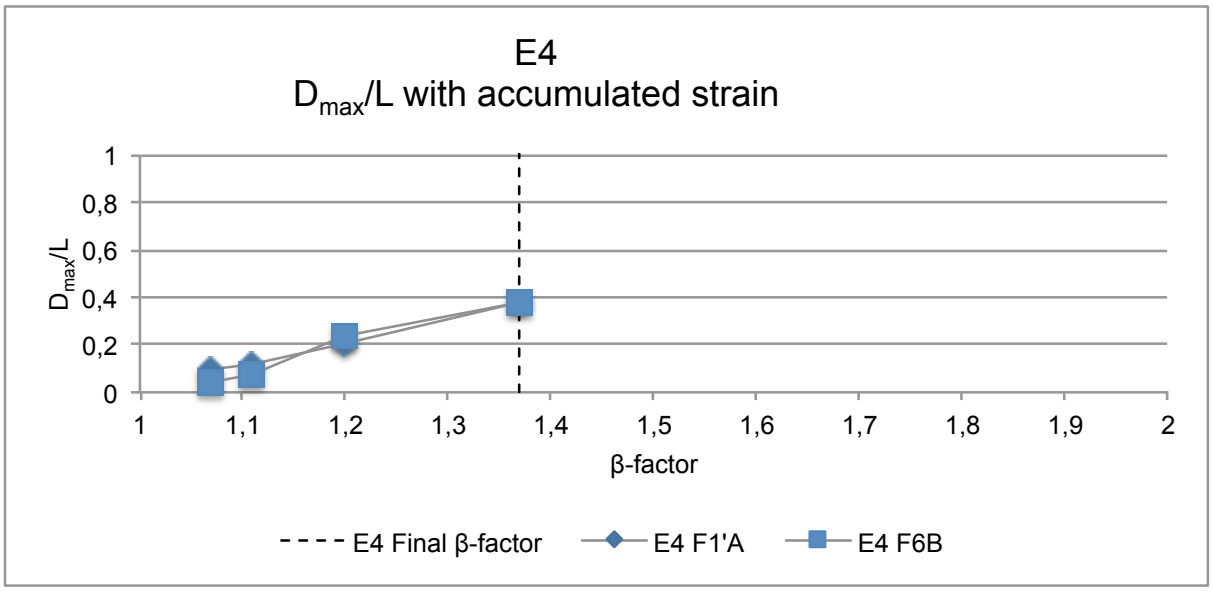

Fig. B 17: Maximum displacement (D_{max}) and length (L) ratio plotted against the accumulated strain (β-factor) for model E4.

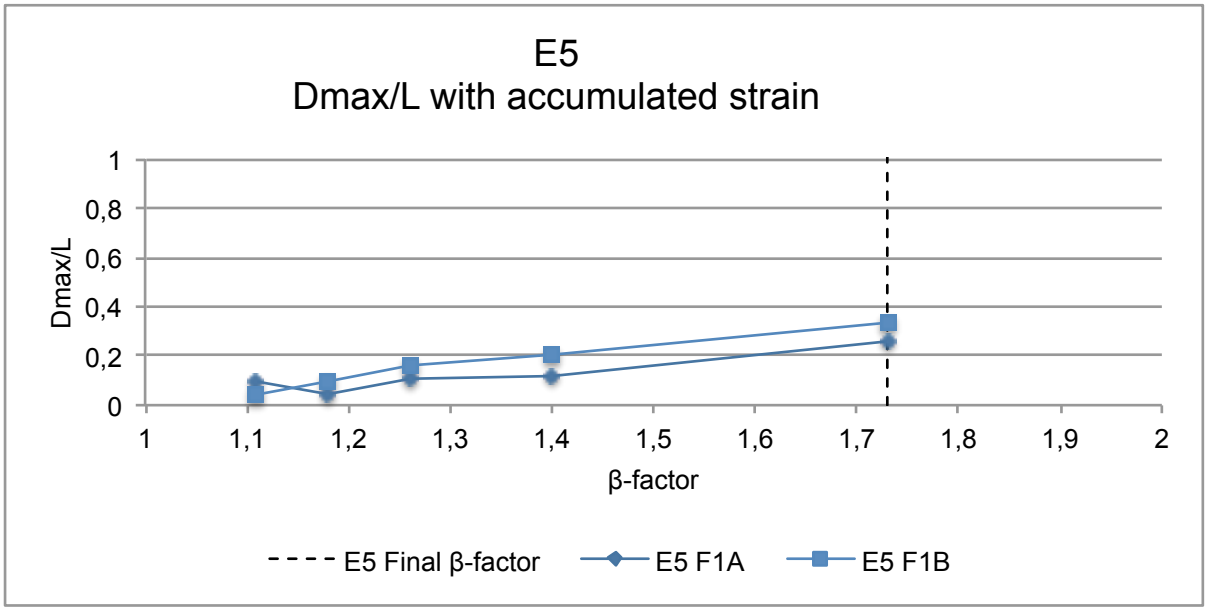

Fig. B 18: Maximum displacement (D_{max}) and length (L) ratio plotted against the accumulated strain (β-factor) for model E5.

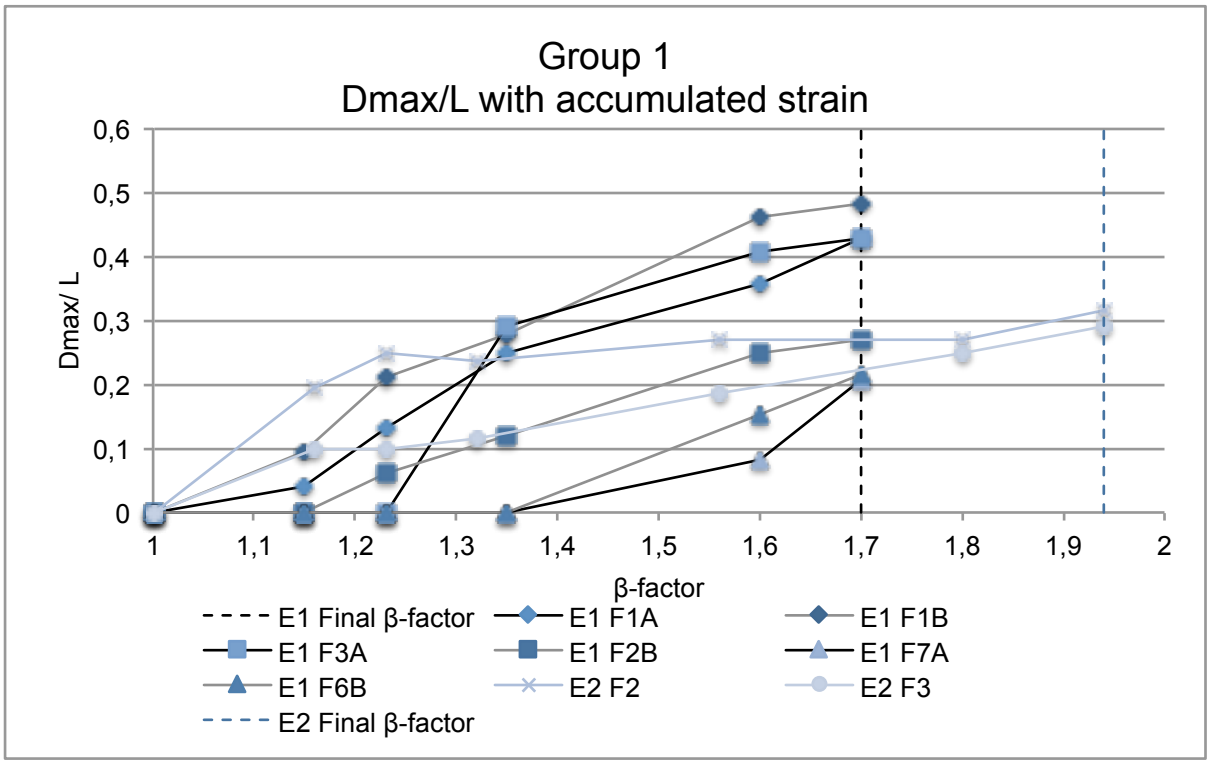

Fig. B 19: Maximum displacement (D_{max}) and length (L) ratio plotted against the accumulated strain (β-factor) for group 1 (models E1 and E2).

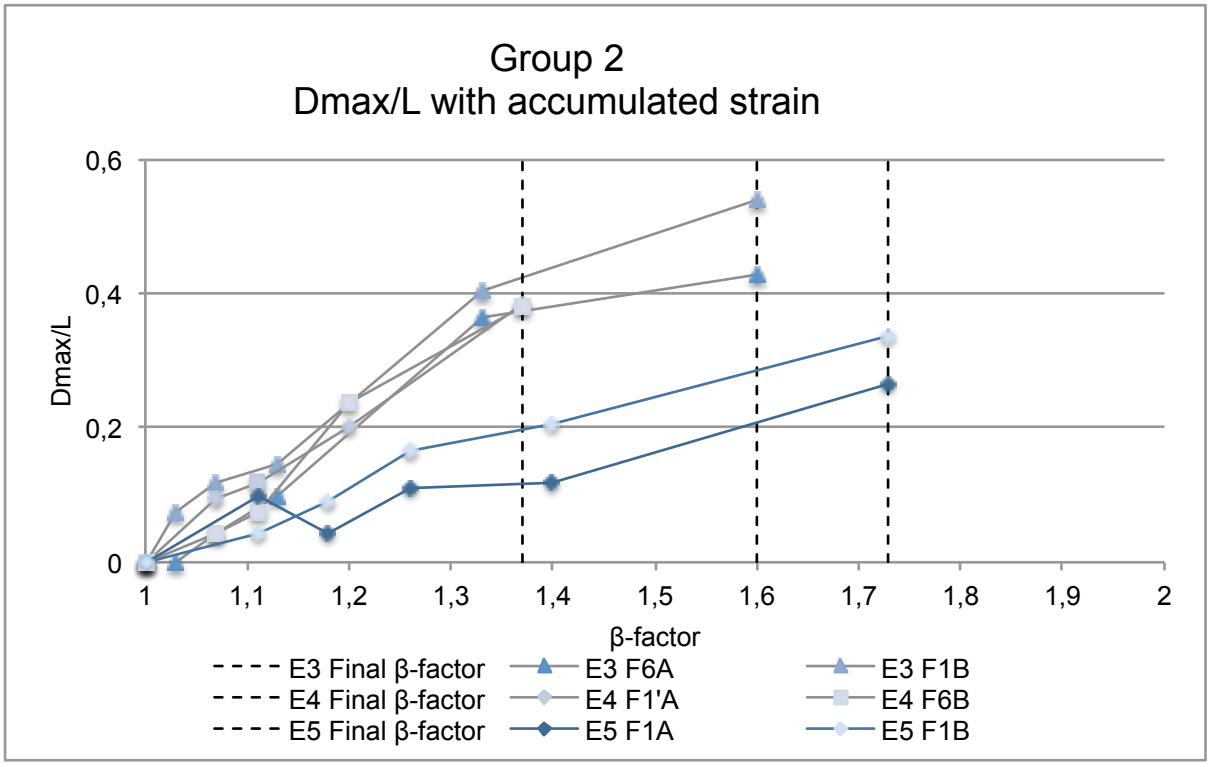

Fig. B 20: Maximum displacement (D_{max}) and length (L) ratio plotted against the accumulated strain (β-factor) for group 2 (models E3, E4 and E5).

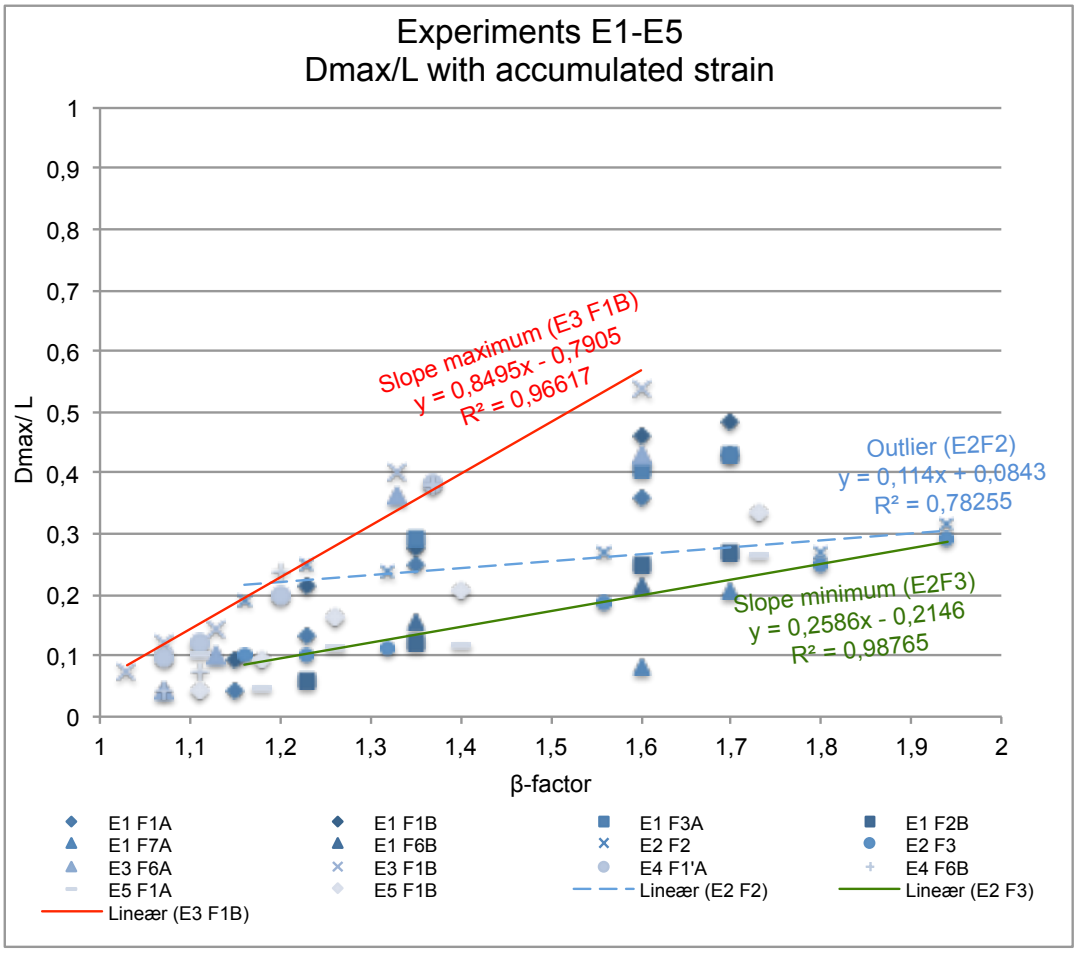

Fig. B 21: The maximum displacement to length ratio is plotted as points against the amount of strain (β-factor).

The plot in Fig. B 21 shows the collective plots D_{max}/L with strain for the main faults of E1-E5 assembled in a wedge shape.

The data assemblage indicates a maximum and minimum slope of D_{max}/L-value with strain. The linear regression trend lines were made for each data set in MS Excel. Most of the plots fall within a slope minimum of ca. 0.26x-02 with 99% accuracy for E2F3 and a maximum of ca. 0.85-0.80 with 97% accuracy for E3F1B. Fault E2F2 is again an outlier with a very low slope of ca. 0.11x+0.08 with 78% accuracy, which is not a very consistent slope. Fault E1 F7A also falls out of this interval as it forms late and is represented with two data points, which yields a high slope. The referenced formulas and accuracy (R^2) is annotated in Fig. B 21. The collective plots of D_{max}/L with strain for the main faults of E1-E5assembled in a wedge shape. The maximum and minimum slopes of D_{max}/L with strain are experimental and should not be used as a reference without further investigations. The estimated end-members of the wedge shape are based on data collected for the master faults presented in this thesis.

Horizontal, vertical along-fault displacements

Tab. B 1: Maximum displacement is measured along the fault plane, throw is measured vertical displacement and heave is measured horizontal displacement. The percentage of total horizontal extension is estimated based on the amount of heave measured in the models and the total amount of extension of each model. The measured values represent faults with apparent displacements.

Model number	D_{max} (cm)	Throw (cm)	Heave (cm)	Percentage total heave accommodated by large faults
E1A	28.31	16.57	14.81	70.51%
E1B	20.64	15.36	14.87	70.80%
E2	32.33	12.77	22.48	70.25%
E3A	16.33	9.32	8.86	49.20%
E3B	10.96	10.84	7.83	43.51%
E4A	23.73	11.98	10.30	89.57%
E4B	16.75	9.58	9.28	80.67%
E5A	23.67	12.71	13.79	62.70%
E5B	22.14	11.08	10.78	49.01%

Appendix C: Video attachments

Photos shot during the experiments are compiled to videos and are attached on a DVD. The videos are best played in QuickTime for Mac-users and VLC Media Player for Windows-users.

Videos attached:

Model number (Laboratory reference)	Title of video side A (File size)	Title of video side B (File size)	Title of video surface (File size)
E1 (03-13)	E1 side A (03-13A).mov (317,3 MB)	E1 side B (03-13B) vendt.mov (21.28 MB)	N/A
E2 (06-13)	E2 (06-13).mov (56,7 MB)	N/A	N/A
E3 (50-14)	E3 side A (50-14).mp4 (111.8 MB)	E3 side B (50-14B) vendt (103,9 MB)	E3 (50-14) Surface deformation vendt (81.9 MB)
E4 (51-14)	E4 side A (51-14A).mp4 (105,3 MB)	E4 side B (51-14B) vendt (42 MB)	E4 (51-14) Surface deformation.mov (774.2 MB)
E5 (52-14)	E5 side A (52-14A).mov (229,4 MB)	E5 side B (52-14B) vendt (63,1 MB)	E5 (52-14) Surface deformation.mov (390.4 MB)